

VU Research Portal

Outer Tracker calibration and open charm production cross section measurement at LHCb

Kozlinskiy, A.

2013

document version

Publisher's PDF, also known as Version of record

[Link to publication in VU Research Portal](#)

citation for published version (APA)

Kozlinskiy, A. (2013). *Outer Tracker calibration and open charm production cross section measurement at LHCb*. [PhD-Thesis - Research and graduation internal, Vrije Universiteit Amsterdam].

General rights

Copyright and moral rights for the publications made accessible in the public portal are retained by the authors and/or other copyright owners and it is a condition of accessing publications that users recognise and abide by the legal requirements associated with these rights.

- Users may download and print one copy of any publication from the public portal for the purpose of private study or research.
- You may not further distribute the material or use it for any profit-making activity or commercial gain
- You may freely distribute the URL identifying the publication in the public portal

Take down policy

If you believe that this document breaches copyright please contact us providing details, and we will remove access to the work immediately and investigate your claim.

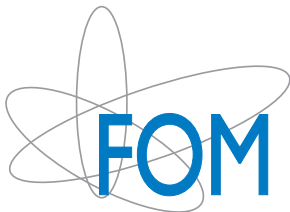
E-mail address:

vuresearchportal.ub@vu.nl

**Outer Tracker calibration
and open charm production cross section
measurement at LHCb**

Alexandr Vladimirovich Kozlinskiy

Cover by Shamil Gumirov (shamil@gumirov.com) and Maria Chaplina
Printed by Off Page (www.offpage.nl)
Copyright © 2013 A.V.Kozlinskiy, all rights reserved



This work is part of the research program of the Foundation for Fundamental Research on Matter (FOM), which is part of the Netherlands Organization for Scientific Research (NWO).

VRIJE UNIVERSITEIT

**Outer Tracker calibration
and open charm production cross section
measurement at LHCb**

ACADEMISCH PROEFSCHRIFT

ter verkrijging van de graad Doctor aan
de Vrije Universiteit Amsterdam,
op gezag van de rector magnificus
prof.dr. L.M. Bouter,
in het openbaar te verdedigen
ten overstaan van de promotiecommissie
van de Faculteit der Exacte Wetenschappen
op woensdag 22 mei 2013 om 11.45 uur
in de aula van de universiteit,
De Boelelaan 1105

door

Alexandr Vladimirovich Kozlinskiy

geboren te Krasnoyarsk, Rusland

promotor:	prof.dr. M.H.M. Merk
copromotor:	dr. Th.S. Bauer

Table of contents

Introduction	1
1 Theory	3
1.1 Introduction	3
1.2 Heavy quark production	4
1.2.1 Parton model	4
1.2.2 Parton density function	5
1.2.3 pQCD	6
1.2.4 Renormalization	6
1.2.5 Resummation	8
1.3 Charm physics beyond production	9
2 The LHCb experiment	11
2.1 The LHC collider	11
2.2 The LHCb detector	12
2.3 Sub-detectors	14
2.3.1 VELO	14
2.3.2 Tracker Turicensis	16
2.3.3 Inner Tracker	17
2.3.4 Outer Tracker	17
2.3.5 RICH	19
2.3.6 Calorimeters	20
2.3.7 Muon System	20
2.4 Trigger	21
2.5 LHCb 2010 and 2011 operation	22
3 Outer Tracker simulation	25
3.1 Detector description	25
3.2 Digitization	28
3.3 Summary	35
4 OT calibration	37
4.1 The OT time measurement	37
4.2 t_0 calibration	41
4.3 TR-relation calibration	45

4.4	Walk correction	50
4.5	The average OT time and spatial resolution	52
4.6	Mono-layer shift	55
4.7	Results	61
5	D^0 and D^{*+} production cross section	67
5.1	Data set	68
5.2	Event selection	69
5.3	Yield extraction	75
5.4	Efficiency	79
5.5	Systematic uncertainties	90
5.6	Cross section	100
5.7	D^{*+} polarization	105
5.8	Summary	106
A	TR-relation PDF	107
B	D^0 and D^{*+} fits	113
	Bibliography	129
	Summary	133
	Samenvatting	135
	Acknowledgments	137

Introduction

Quantum chromodynamics (QCD) is the theory of the strong interactions that describes the interaction of quarks and gluons. In QCD, the six quark flavors are divided in light and heavy quarks, depending on the relation of the quark mass to the QCD scale. The heavy quarks are charm and beauty, and at the scale of charm quark mass the cross section can be calculated perturbatively. The knowledge of heavy quark production in proton-proton collisions allows to test predictions of QCD. In addition, the charm and beauty from QCD processes contribute to the background for other processes, such as Higgs production.

The LHC is a proton-proton collider located in a circular tunnel 27 km in circumference. The LHC is designed to collide two beams of protons or heavy ions at a nominal energy of 7 TeV per proton. Four experiments are located at interaction points, where the beams are crossed and collide at small angles. ATLAS and CMS are general purpose experiments that can operate at high luminosity, whereas LHCb and ALICE are dedicated experiments operating at a lower luminosity.

The LHCb experiment is one of the four major experiments at the LHC. The LHCb detector is a single-arm forward spectrometer dedicated to flavor physics studies at the LHC. Its main goals are measurements of CP-violation and the studies of rare decays of heavy flavor particles, in particular to search for 'new physics' beyond the Standard Model using the decays of b - and c - hadrons. The knowledge of the heavy flavor production cross section is particularly important for estimates of the sensitivity of LHCb for these measurements.

In Chapter 1 a brief introduction to the theory of heavy flavor production is given. Several theoretical methods to calculate the cross sections are shortly described.

Chapter 2 gives an overview of LHC and the LHCb detector. An overview of each sub-detector and the performance of the detector during the 2010 and 2011 data taking periods are presented.

The Outer Tracker, one of the LHCb sub-detectors, is a drift-time detector used for tracking of charged particles to measure their momentum. Chapter 3 describes the Outer Tracker, focusing on the Monte Carlo (MC) simulation and detector digitization descriptions, and on how they compare to the real detector.

About 70% of the reconstructed tracks pass through the active area of the OT, and for these tracks about half of the hits are provided by the OT. The calibration of the Outer Tracker is important to achieve the optimal momentum resolution for reconstructed tracks. In Chapter 4 a description of the developed calibration

procedures is given. These procedures include t_0 calibration and time-to-distance calibration, signal walk corrections and a resolution calibration. The performance of the calibration is illustrated over the full 2011 data period.

Finally, in Chapter 5 the measurements of the production cross section of $D^0 + \bar{D}^0$ and $D^{*+} + D^{*-}$ mesons at the LHCb detector are presented. This measurement was performed using 15 nb^{-1} of proton-proton collision data collected with the LHCb detector at 7 TeV center-of-mass energy in May 2010. The cross sections are measured in bins of transverse momentum and rapidity in the acceptance of the LHCb detector, and are compared with two theoretical calculations. In addition, the ratio of cross sections and total $c\bar{c}$ productions cross sections are estimated.

Chapter 1

Theory

Heavy flavor production is an important area for understanding quantum chromodynamics, one of the three fundamental forces in the Standard Model. In the past years the theoretical understanding of the b and c production has greatly improved [1–3].

In this chapter a brief theoretical overview of heavy quark production is given. Section 1.1 gives an introduction into the history of the charm quark and its role in the Standard Model (SM). A theoretical model and techniques for cross section calculation are described in Section 1.2. Finally in Section 1.3 charm physics beyond charm production is discussed.

1.1 Introduction

In quantum chromodynamics (QCD), the six quark flavors are divided in light and heavy quarks, depending on the relation of the quark mass to the QCD scale $\Lambda_{\text{QCD}} \sim 0.2 \text{ GeV}$, where QCD becomes non-perturbative. The light quarks u , d and s have masses $m_q \lesssim \Lambda_{\text{QCD}}$, and the heavy quarks c , b and t have masses $m_q \gg \Lambda_{\text{QCD}}$.

The existence of the charm quark was predicted in 1970 [4], to explain the suppression of Flavor-Changing-Neutral-Current (FCNC) known as the GIM mechanism. In 1973 [5] the CKM matrix was introduced extending the GIM mechanism by inclusion of a third generation of quarks.

The charm quark¹ was discovered in 1974 when the J/ψ resonance was observed at the SLAC electron positron storage ring [6]. This particle was at the same time observed at the Brookhaven 30 GeV alternating-gradient synchrotron [7]. The J/ψ resonance was interpreted as a previously unobserved bound state of a $c\bar{c}$ pair. This interpretation was confirmed by the measurement of the ratio $R(s) = \sigma(e^+e^- \rightarrow \text{hadrons})/\sigma(e^+e^- \rightarrow \mu^+\mu^-)$ at higher center-of-mass energies [8], which was in a good agreement with the prediction, assuming the existence and mass of the charm

¹The name “charm” appeared even before the discovery, and reflects the property that astonishing agreement between theory and data can be achieved by adding this quark to the model (i.e. GIM mechanism).

quark. The charm quark discovery was a fundamental step for the development of the SM with two generations of quark pairs.

The charmed meson family is broad. Many open (charm + light quark) and closed ($c\bar{c}$) charm mesons have been discovered and their properties have been measured. The open and closed charm production cross section in hadron collisions tests the QCD predictions for the heavy quark production mechanism. In addition, the precise knowledge of the heavy quark production cross section is important as charm and beauty from QCD processes contribute to the background for other, often rare, SM processes, e.g. in Higgs production.

1.2 Heavy quark production

1.2.1 Parton model

At the high energies of hadron colliders, such as the LHC, the interaction occurs between partons (quarks and gluons) of the colliding hadrons. A schematic illustration of the process is shown in Fig. 1.1. To describe such processes the following variables are used:

- $S = (P_1 + P_2)^2$, where P_1 and P_2 are the four momenta of colliding hadrons;
- $p_1 = x_1 P_1$ and $p_2 = x_2 P_2$ are the four momenta of interacting partons, where x_1 and x_2 are four momenta fractions of the partons with respect to the hadrons;
- $s = (p_1 + p_2)^2$ is the center-of-mass energy of the interacting partons.

The interaction between individual partons is described with the parton density functions (PDF). The PDF $f_i(x)$ defines the probability to find a parton i with a momentum fraction x . Consequently, the combination of all PDFs should satisfy the sum rule:

$$1 = \sum_i \int_0^1 x f_i(x) dx, \quad (1.1)$$

where the sum goes over all quarks and gluons.

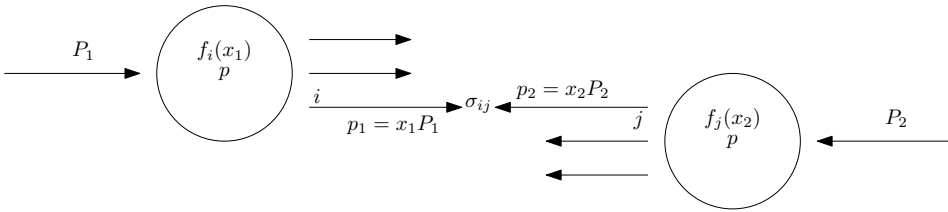


Figure 1.1: Schematic illustration of interaction between two colliding protons.

Based on the initial distributions described with these PDFs the heavy quark production cross section in a hadron collision can be written as

$$\sigma_{hh \rightarrow q\bar{q}} = \sum_{i,j} \int_0^1 dx_1 dx_2 f_i(x_1, \mu_F^2) f_j(x_2, \mu_F^2) \sigma_{ij \rightarrow q\bar{q}}(s, m_q, \mu_F^2), \quad (1.2)$$

where $s = (p_1 + p_2)^2 = x_1 x_2 S$ is the center-of-mass energy of the interacting partons, m_q is the mass of the heavy quark, μ_F is the so-called factorization scale, and f_i and f_j are the PDFs. $\sigma_{ij \rightarrow q\bar{q}}$ is the hard cross section of the process.

Equation (1.2) is based on the QCD factorization theorem [9] stating that the hard scattering process can be factorized from the initial state. The initial state is described with the PDFs and the hard scattering can be calculated within perturbative QCD (pQCD).

1.2.2 Parton density function

The parton density function $f_i(x, \mu_F^2)$ describes the distribution of parton i as a function of momentum fraction x at the probing scale μ_F . The PDFs in general are not calculable perturbatively, however, their evolution as a function of scale μ_F can be obtained through the Altarelli-Parisi (DGLAP) equations [10,11]. This implies that the shape of the PDF have to be fixed at a given scale, for example from the experimental cross sections, such as Deep Inelastic Scattering (DIS) or Drell-Yan processes. In addition, functions f_i depend on the factorization scheme and the order of perturbation theory at which the evolution is calculated.

There are different collaborations, like CTEQ [12] and MSTW [13], that perform fits to a wide range of data to extract the PDFs. However, in general their results are not directly comparable, as both the definition of the f_i functions and the data used in the fits are different. Figure 1.2 shows an example of the CTEQ 6.6 PDF sets for u , \bar{u} , d and c quarks at two different scales, $\mu_F = 2 \text{ GeV}$ and $\mu_F = 10 \text{ GeV}$.

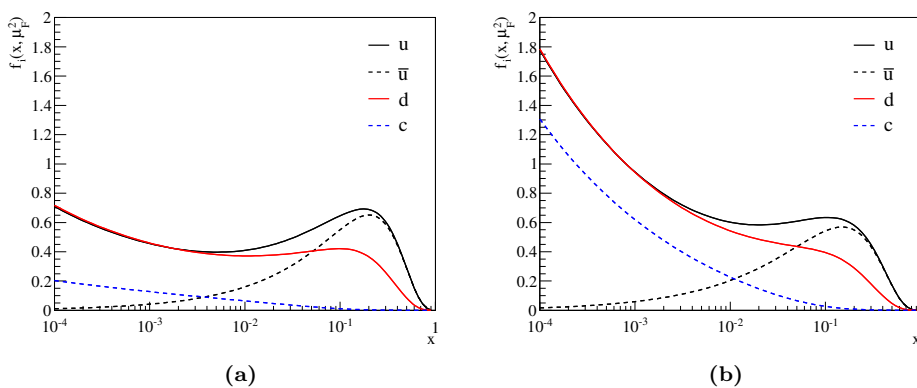


Figure 1.2: CTEQ 6.6 PDF sets for u , \bar{u} , d and c quarks at scales $\mu_F = 2 \text{ GeV}$ (a) and $\mu_F = 10 \text{ GeV}$ (b).

Note that the scale μ_F at which the cross section is calculated is arbitrary and the dependence of the final result on its value comes from the fact that the calculation is performed at a certain order. This dependence in general becomes smaller at higher order and one way to estimate the uncertainty of the calculation is by varying the scale by a factor of 2 around nominal. However, the order of PDF sets have to match the order at which the hard scattering cross section is calculated.

1.2.3 pQCD

Assuming that the coupling constant α_s is small, which is the case in the perturbative regime, it is possible to calculate the cross section expanded in orders of α_s^n :

$$\sigma = \sigma_0 + \alpha_s \sigma_1 + \alpha_s^2 \sigma_2 + \dots, \quad (1.3)$$

where σ_0 is the Leading Order (LO) or Born level cross section. Calculations up to $\alpha_s \sigma_1$ and $\alpha_s^2 \sigma_2$ are known as the Next-to-Leading Order (NLO) and Next-to-Next-to-Leading Order (NNLO), respectively. The cross sections are calculated using Feynman diagrams. Figure 1.3 shows LO diagrams for the process $gg \rightarrow q\bar{q}$ which is dominant source of $q\bar{q}$ production at LHC and is commonly referred to as gluon fusion.

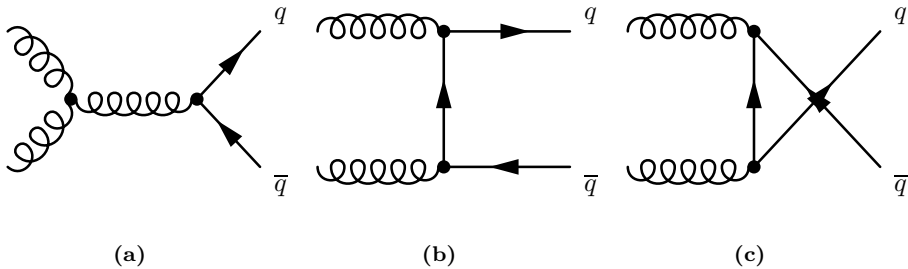


Figure 1.3: LO diagrams for the process $gg \rightarrow q\bar{q}$.

The higher orders (up to $\alpha_s^n \sigma_n$, where $n \geq 1$) contain the divergences that spoil the predictive power of QCD. The sources of these divergences are:

- Ultraviolet (UV) divergences that arise from virtual loops in propagators;
- Infrared (IR) divergences due to the soft gluon emission or collinear emission;

The UV and IR divergences are controlled by renormalization and resummation techniques that are discussed later in this section.

1.2.4 Renormalization

The renormalization technique allows to handle UV divergences. The divergent terms are first isolated by means of regularization and subsequently the couplings,

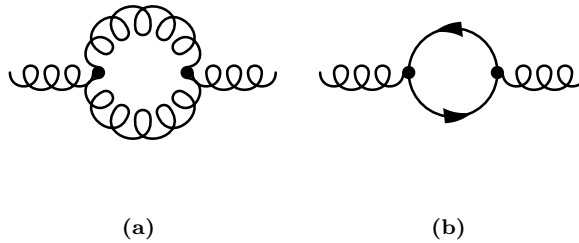


Figure 1.4: Virtual gluon (a) and quark (b) loops.

masses and fields are redefined such that infinities cancel.

The regularization technique allows to calculate the divergent integrals that appear due to virtual loops in the propagators (see Fig. 1.4). There are different regularization techniques available, such as the so-called cut-off and dimensional regularizations.

The cut-off regularization introduces a large but finite scale μ to which the integration is performed such that the integrals are finite:

$$I = \int \frac{dp}{p} \rightarrow \int \frac{dp}{p} \sim \log(\mu^2/Q^2), \quad (1.4)$$

where Q is the interaction scale. Only at the end of the full calculation the limit of $\mu \rightarrow \infty$ is taken.

The most widely used technique is dimensional regularization [14] as it preserves symmetries and gauge invariance. In this method the 4-dimension integrals are replaced with D -dimension integrals:

$$\int d^4p \rightarrow \mu^{4-D} \int d^Dp, \quad (1.5)$$

where $D = 4 - \varepsilon$ and at the end the limit $\varepsilon \rightarrow 0$ is taken. Arbitrary scale μ is introduced to keep physical dimensions.

The redefinition of couplings, masses and fields introduces counter-terms that serve to cancel infinities at each order of perturbation theory. In that case a theory is called renormalizable.

Various types of renormalization techniques have been introduced. The most popular are the Minimal Subtraction (MS) and the modified Minimal Subtraction ($\overline{\text{MS}}$) schemes.

The $\overline{\text{MS}}$ renormalization scheme uses the following rules:

- Dimensional regularization is used to control UV divergences;
- The arbitrary scale μ that appears in the dimensional regularization is set to the energy scale Q , such that logarithms of the form $\log(\mu^2/Q^2)$ vanish;

- The finite term of the renormalization counter-term is set to zero such that the counter-term only subtracts divergences.

1.2.5 Resummation

Next-to-leading order calculations of heavy quark production are available since many years. The main assumptions in these calculations are based on the fact that masses of heavy quarks are relatively large compared to Λ_{QCD} and therefore the cross section can be written as an expansion in powers of the strong coupling constant α_s . The coupling constant can be evaluated at the renormalization scale, which can be chosen to be the mass of the heavy quark.

The most widely used approach is known as collinear approximation, where the production cross section is calculated in an expansion in orders of α_s , neglecting the logarithmic terms. In addition there is an approach of Fixed Order NLO calculation, which resums the large terms proportional to $\alpha_s^n \log^k(p_T/m)$, where m and p_T are the mass and transverse momentum of the heavy quark, respectively.

The heavy quark production cross section can be written as [1]:

$$\sigma_q(p_T, m) = \sigma_0 \left[1 + \sum_{n=1} \alpha_s^n \sum_{k=0}^n c_{nk} \ln^k \left(\frac{p_T^2}{m^2} \right) \right], \quad (1.6)$$

where σ_0 is the Born cross section, c_{nk} are constants² and $\alpha_s^n \ln^k(p_T^2/m^2)$ are the divergent logarithmic terms.

There are many different resumming approaches, such as GMVFNS [15, 16], FONLL [17, 18], etc. All resum the Leading Logarithmic (LL) terms $\alpha_s^n \ln^n(p_T^2/m^2)$ or in some cases Next-to-Leading Logarithmic (NLL) terms $\alpha_s^n \ln^{n-1}(p_T^2/m^2)$.

The idea is to factor all logarithms into a resummation factor:

$$\sigma_q(p_T, m) = \sigma_0 \otimes C(p_T, \mu) \otimes f(\mu, m), \quad (1.7)$$

where $C(p_T, m)$ are coefficients, and $f(\mu, m)$ are PDFs or fragmentation functions and \otimes denotes convolution over momentum fractions. The parameter μ represents the artificial factorization scale. The logarithms in coefficients can be set to zero by choosing $\mu \sim p_T$. The f functions, known at some scale μ_0 , are obtained at scale μ through DGLAP evolution equations. Note that due to the large mass of heavy quarks it is actually possible to calculate the f functions in perturbation theory, which is not the case for light quarks where they must be obtained from fits to data.

The resummed cross section in the massless limit ($p_T \gg m$) is then matched with the Fixed Order (FO) cross section at $p_T \sim m$, where the logarithmic terms can be neglected and the Born cross section is valid. This allows to provide a prediction for the cross section in a wide p_T range.

Currently, several approaches based on the logarithm resummation are in use. They differ in the following points:

- To what order the initial condition $f(\mu_0, m)$ is evaluated and the accuracy of evolution;

²The coefficients c_{nk} can also contain functions of m and p_T vanishing when $p_T \gg m$.

- How matching to FO calculations is performed.

Two approaches, GMVFNS and FONLL, are discussed below.

Fixed Order Next-to-Leading Log

The Fixed Order Next-to-Leading Log (FONLL) approach was developed to improve the calculation of heavy quark differential cross section at large p_T . FONLL provides a way to calculate the differential cross section of inclusive heavy quark production. It is based on the Next-to-Leading Order (NLO) massive calculation with Next-to-Leading Log (NLL) resummation.

The matching between the FO cross section ($p_T \sim m$) and the resummed cross section ($p_T \gg m$) is performed with [17]:

$$\sigma_{\text{FONLL}} = \sigma_{\text{FO}} + (\sigma_{\text{RS}} - \sigma_{\text{FO},M0}) \cdot G(m, p_T) \quad (1.8)$$

where σ_{FO} is a fixed order calculation, σ_{RS} is a resummed calculation and $\sigma_{\text{FO},M0}$ is the FO calculation in the zero mass limit. The subtraction $\sigma_{\text{RS}} - \sigma_{\text{FO},M0}$ allows to cancel terms that are present in both σ_{FO} and σ_{RS} , and the function $G(m, p_T) \sim \frac{p_T^2}{p_T^2 + m^2}$ allows to perform the matching between large p_T and small p_T , where this subtraction term is suppressed.

General Mass Variable Flavor Number Scheme

The General Mass Variable Flavor Number Scheme (GMVFNS) approach is an extension of the Fixed Flavor Number Scheme (FFNS) and the Zero Mass Variable Flavor Number Scheme (ZMVFN).

The FFNS is based on the assumption that the gluon and the light partons (u , d and s) are the only active partons, and that the heavy quark (c or b) appears only in the final state. In the ZMVFN approach the heavy quark is added to the initial state; however, its mass is neglected in the matrix calculation. The FFNS is applicable when $p_T \sim m$, whereas ZMVFN is used in case of $p_T \gg m$.

The GMVFNS combines the FFNS, by retaining the mass depended term, with ZMVFN, by absorbing large logarithms into parton distribution and fragmentation functions. This approach allows to determine the cross section in a wide kinematic range.

The difference with FONLL is that GMVFNS does not use perturbative NLO fragmentation functions. Instead, non-perturbative fragmentation functions (fitted at LEP) of heavy mesons are used. Consequently, the GMVFNS does not produce the pure NLO cross section.

In this thesis the experimentally measured production cross section of open charm particles is compared to both the FONLL and GMVFNS calculations.

1.3 Charm physics beyond production

There has been an enormous development in the experimental knowledge of the charm sector in the past few years [19]. This includes the measurement of open and

closed charm production, double charm production, the $c - \bar{c}$ production asymmetry, as well as CP violation (CPV) and $D^0 - \bar{D}^0$ mixing.

The LHCb collaboration has performed several measurements for the production cross section of beauty [20] and charm mesons [21]. In this thesis the measurement of the charm production cross section at $\sqrt{s} = 7$ TeV is described. The total charm production cross section is found to be about 20 times larger than the beauty production. This makes an extensive study of charm physics possible at LHCb.

For example, a precision measurement of CPV in the charm sector, which is predicted to be small in the SM, is within experimental reach. In particular LHCb contributed to the measurement of mixing in the $D^0 - \bar{D}^0$ system [22] which is now well established at the 10σ significance level, combining results from five different experiments (including LHCb). Recent results from CDF and LHCb also include evidence of non-zero direct CPV in $D^0 \rightarrow K^+ K^-$ and $D^0 \rightarrow \pi^+ \pi^-$ decays [23, 24]. The combined result for direct CPV is that $\Delta a_{CP}^{dir} \neq 0$ at the 4σ significance level (including LHCb, CDF, Belle and BABAR).

The double charm production recently measured at LHCb [25] shows good agreement for J/ψ production accompanied by open charm meson, however, a discrepancy with the predicted cross section is observed for double open charm production.

The observation of the asymmetry in the decay of D^0/\bar{D}^0 mesons boosted interest in studies of the production asymmetries of other charm mesons and baryons, for example the D^+/D^- , D_s^+/D_s^- and Λ_b^+/Λ_b^- production asymmetries.

Given the small asymmetries observed in the charm sector a very large sample of charm decays is needed. The large production cross section, in combination with the high efficiency of LHCb detector, as will be described in the next chapter, will lead to interesting results in the future.

Chapter 2

The LHCb experiment

The Large Hadron Collider beauty (LHCb) experiment is one of the four major experiments at the Large Hadron Collider (LHC) at CERN. The other detectors are ATLAS, CMS and ALICE. These experiments were designed as central detectors, whereas LHCb is a single-arm forward spectrometer. They are all designed to perform extensive tests of the Standard Model (SM) as well as for searches of New Physics (NP) beyond the SM.

2.1 The LHC collider

The LHC [26] is a proton-proton collider located in a circular tunnel 27 km in circumference. The tunnel lies between 45 m and 170 m below the surface. The LHC is designed to collide two beams of protons or heavy ions. The nominal energy of each beam is 7 TeV. In the years 2010 and 2011 the LHC operated at an energy of 3.5 TeV per beam, and in 2012 at 4 TeV per beam. After a shutdown in 2013 and 2014 the machine is expected to operate at full energy. To reach collision energies the beams are first accelerated in the Super Proton Synchrotron (SPS) to 450 GeV and then injected into the LHC ring, where they are accelerated to the nominal energy.

The protons in each beam are grouped into bunches, each containing about 10^{11} protons. Each beam can contain 3564 bunches, however, due to the filling procedure only up to 2808 bunches per beam can be filled. The nominal bunch spacing is 25 ns, resulting in a 40 MHz collision rate.

The four experiments are located at interaction points (IP), as shown in Fig. 2.1, where the beams are crossed and collide at small angles. ATLAS [27] and CMS [28] are general purpose experiments that can operate at a high luminosity of $L = 10^{34} \text{ cm}^{-2}\text{s}^{-1}$, whereas LHCb [29] and ALICE [30] are dedicated experiments operating at lower luminosity of the order of $L = 10^{32} \text{ cm}^{-2}\text{s}^{-1}$ and $L = 10^{27} \text{ cm}^{-2}\text{s}^{-1}$ (lead-lead ion operation), respectively.

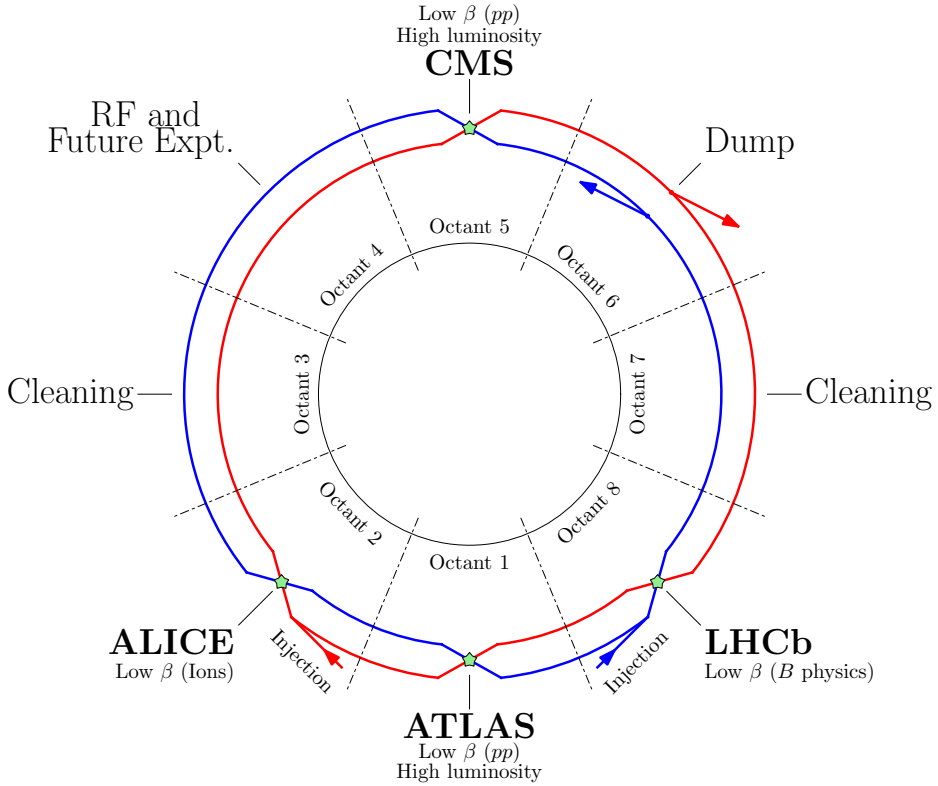


Figure 2.1: Schematic view of LHC. The four main experiments shown are LHCb, ATLAS, CMS and ALICE.

2.2 The LHCb detector

LHCb detector is a single-arm forward spectrometer dedicated to flavor physics studies at the LHC. Its main goals are the measurements of CP-violating observables as well as rare decays of heavy flavor particles, to search for 'new physics' beyond the Standard Model using the decays of b - and c - hadrons.

The $b\bar{b}$ production cross section at $\sqrt{s} = 7$ TeV is $\sigma_{b\bar{b}} \approx 300 \mu\text{b}$ [20]. The proton-proton inelastic cross section at 7 TeV is $\sigma_{in} \approx 70 \text{ mb}$ [31,32] and the expected yield of $b\bar{b}$ is about one in 200 collisions. At the energies of the LHC the main contributions to the $b\bar{b}$ production are gluon fusion, gluon splitting and flavor excitation. Figure 2.2 shows the Feynman diagrams for these processes.

Due to uniform distributions in rapidity ("rapidity plateau"), the $b\bar{b}$ pairs are produced predominantly in forward ($\theta = 0$) or backward ($\theta = \pi$) directions (Fig. 2.3). The design of the LHCb detector is optimized for these kinematics.

The side view of the LHCb detector is shown in Fig. 2.4. The LHCb detector has an acceptance of $2 < \eta < 5.3$ and consists of the following sub-detectors:

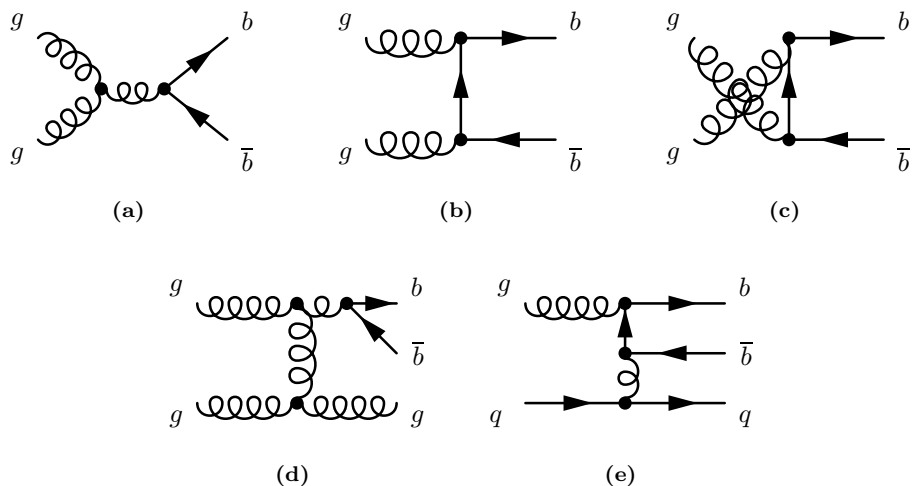


Figure 2.2: Feynman diagrams for production of b -quarks in proton-proton collisions. The top diagrams (a, b and c) show gluon fusion, bottom left (d) is gluon splitting and bottom right (e) is flavor excitation.

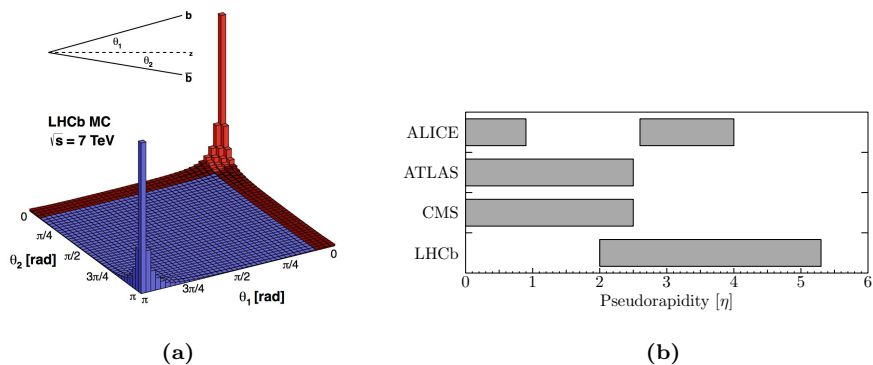


Figure 2.3: (a) Production angles of $b\bar{b}$ pairs at $\sqrt{s} = 7$ TeV. The $b\bar{b}$ pairs are mainly produced in the backward or forward directions relative to the beam direction. (b) Comparison of LHCb acceptance with other LHC experiments.

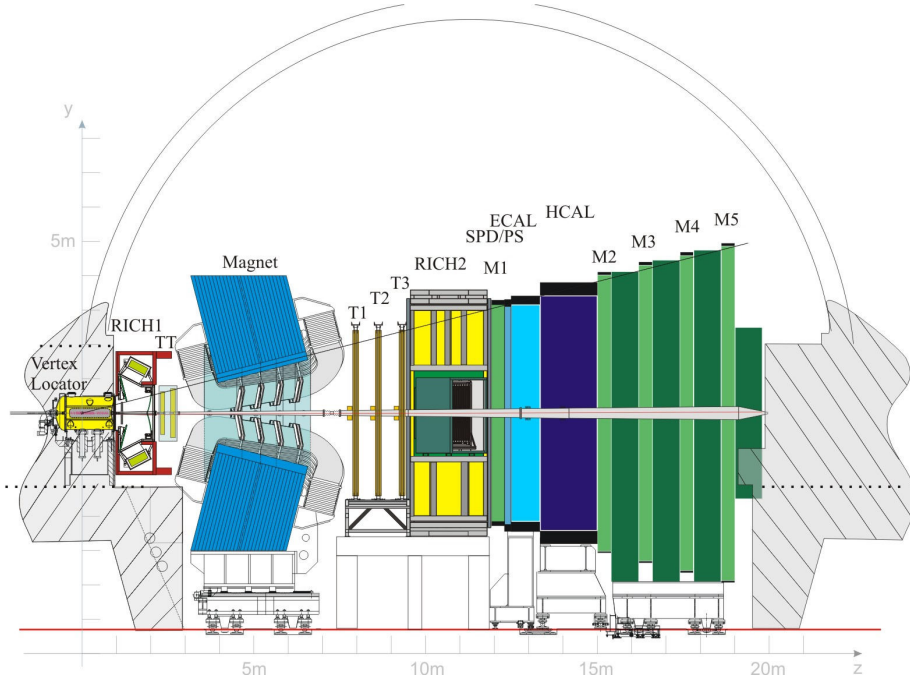


Figure 2.4: Schematic view of the LHCb detector.

- Tracking detectors: Vertex Locator (VELO), Tracker Turicensis (TT), Inner Tracker (IT) and Outer Tracker (OT).
- Particle Identification (PID) detectors: two Ring Imaging Cherenkov Detectors (RICH1 and RICH2), muon detectors, and electromagnetic (ECAL) and hadronic (HCAL) calorimeters.

The warm dipole magnet, located between TT and T-stations, allows the tracking system to reconstruct the momenta of the charged particles. The total integrated magnetic field is 4.2 Tm.

LHCb operates at a luminosity of $(2-5) \cdot 10^{32} \text{ cm}^{-2} \text{ s}^{-1}$, which is smaller than the nominal luminosity of the LHC. This is achieved by focusing the beams to only partly overlap. The same technique allows to keep the luminosity at LHCb constant over the duration of the fill, adjusting the beam focusing periodically. In 2010 and 2011 the average number of interactions per bunch crossing was around 1.5, which corresponds to an average of two interactions per non-empty event.

2.3 Sub-detectors

2.3.1 VELO

Vertex reconstruction is essential for the physics done with the LHCb detector. The Vertex Locator (VELO) [33] provides a precise measurement of track coordi-

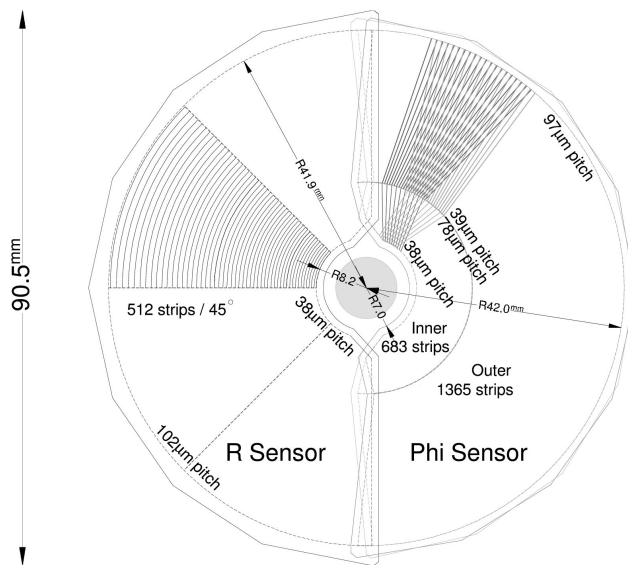


Figure 2.5: The geometry of r (left) and ϕ (right) VELO sensors.

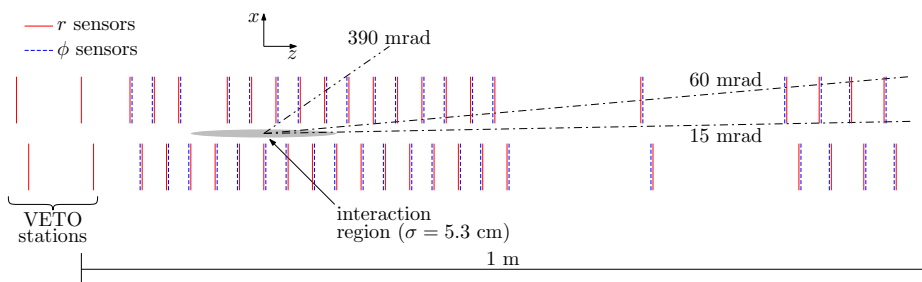


Figure 2.6: The position of left and right module halves along the beam direction.

nates, which are used to reconstruct primary and secondary vertexes. The precise measurement of the primary vertex location and the decay vertexes of beauty and charm hadrons provides information on their lifetimes and on the impact parameters of particles produced in these decays.

The VELO consists of silicon stations located along the beam direction (Fig. 2.6). Each station includes two modules: the left and right half detector modules.

Each module consists of an r -sensor and a ϕ -sensor (Fig. 2.5). The r -sensors are used to measure the radial coordinate of the particle, and the ϕ -sensors are used for the azimuthal coordinate measurement. This layout allows fast track reconstruction that is essential for the trigger.

The r -sensor has four 45° sectors. Each sector consist of 512 readout strips with a pitch increasing with the distance from the center from $38\text{ }\mu\text{m}$ to $102\text{ }\mu\text{m}$. The ϕ -sensor is divided into inner and outer regions. The inner region has radial strips with a stereo angle of 20° with the pitch going from $38\text{ }\mu\text{m}$ to $78\text{ }\mu\text{m}$. The outer region has radial strips with a stereo angle of 10° and a pitch varying from $39\text{ }\mu\text{m}$ to $97\text{ }\mu\text{m}$.

The modules are mounted inside two aluminum boxes, with 21 modules per box and 2 dedicated Level-0 modules on the upstream side. During the LHC injection these boxes are retracted from the beam axis by 3 cm, which is the requirement imposed by the aperture of the LHC beam.

2.3.2 Tracker Turicensis

The Tracker Turicensis (TT) [34] is a silicon microstrip detector located at the upstream side of the dipole magnet. It allows to reduce the amount of ghost tracks¹ and improve the momentum resolution for low momentum tracks. The layout of the

¹Ghosts are formed during pattern recognition due to multiple random combinations of hits.

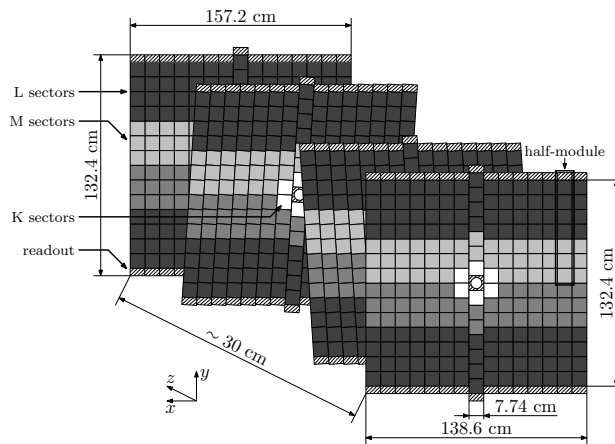


Figure 2.7: The layout of four TT layers ($x-u-v-x$). Different sectors of modules are indicated by differently shaded areas.

TT is shown in Fig. 2.7. TT covers the full acceptance of the detector and consists of four detection layers of silicon sensor ladders. The layers have dimensions of 140 cm in width and 120 cm in height.

The basic building block of a layer is a half-module. Each half-module consists of seven silicon sensors, organized either in two or three readout sectors. Close to the beam pipe, where the particle flux is highest, half-modules are organized into three readout sectors, whereas other half-modules have two readout sectors. The module ladders are positioned in a $x-u-v-x$ configuration with vertical strips in the first and last layers and strips rotated by -5° and $+5^\circ$ in the second and third layers, respectively. Each sensor has a dimension $9.64 \times 9.44 \text{ cm}^2$, is $500 \mu\text{m}$ thick, and has 512 readout strips with a pitch of $183 \mu\text{m}$.

2.3.3 Inner Tracker

The Inner Tracker (IT) [35] is a silicon strip detector that covers the inner regions of the LHCb acceptance and is located directly downstream of the dipole magnet. It consists of three stations, where each station consists of four detector boxes that are arranged around the beam pipe as shown in Fig. 2.8.

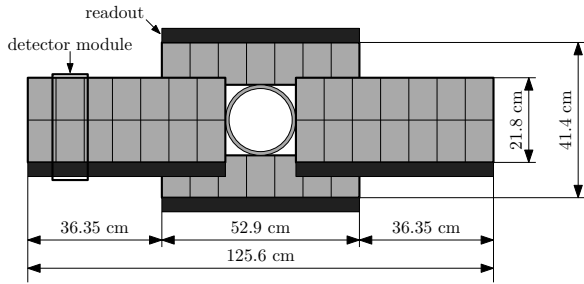


Figure 2.8: The layout of the Inner Tracker station.

Each detector box carries four detection layers of seven modules arranged in a similar $x-u-v-x$ layout as TT. The modules in the top and bottom boxes consist of one silicon sensor, whereas the modules in the left and right boxes contain ladders of two silicon sensors. Each sensor has a dimension of $6.6 \times 11 \text{ cm}^2$ and has 384 readout strips with a pitch of $198 \mu\text{m}$.

2.3.4 Outer Tracker

The Outer Tracker (OT) [36] is a drift-time detector used for tracking of charged particles and their momentum measurement. It uses 5 mm diameter straw tubes and measures the drift time of the ionization clusters induced by charged particles. The distance resolution of the detector is about $200 \mu\text{m}$.

The OT consists of three stations and covers the region outside the IT. Each station consists of four layers of modules in the same $x-u-v-x$ configuration. Each module contains two mono-layers of straw tubes. The modules and read-out

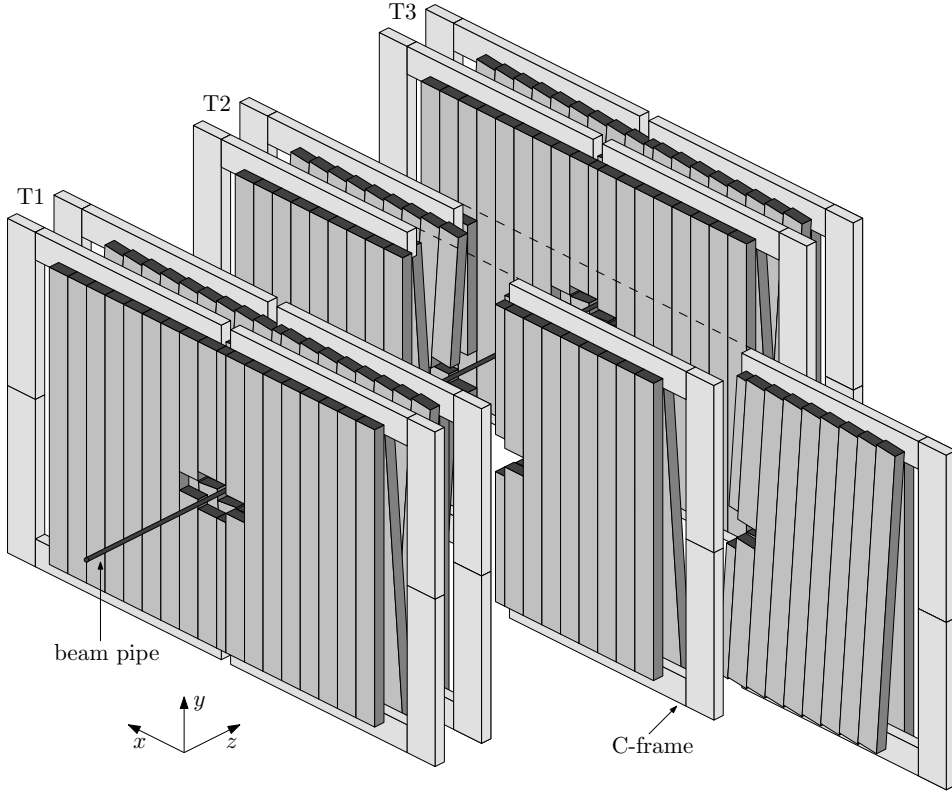


Figure 2.9: Schematic view of the Outer Tracker.

electronics are mounted on support frames (C-frames) outside the active detector area. There are four C-frames per station, two on the C-side ($x < 0$) and two on the A-side ($x > 0$). A schematic view of the OT is shown in Fig. 2.9.

The outer modules (F-modules) span the full vertical acceptance of the detector. There are 128 straws in each F-module (64 per mono-layer), and each straw in the F-modules is divided into a top and a bottom part at $y = 0$, which have separate readout electronics. The inner modules (S-modules) cover the region above and below the IT. There are three types of S-modules (S1, S2 and S3), which differ in width or length. The S1 modules are located on the sides of the beam pipe, next to last F-module. The S2 and S3 modules are located above and below the beam pipe. The S1 and S2 modules contain 128 straws (64 per mono-layer), whereas S3 contains 64 straws (32 per mono-layer). Each C-frame consist of seven F-modules, two S1 modules, and two S2 modules (A side) or two S3 modules (C side). The total number of straws in the OT is 53760.

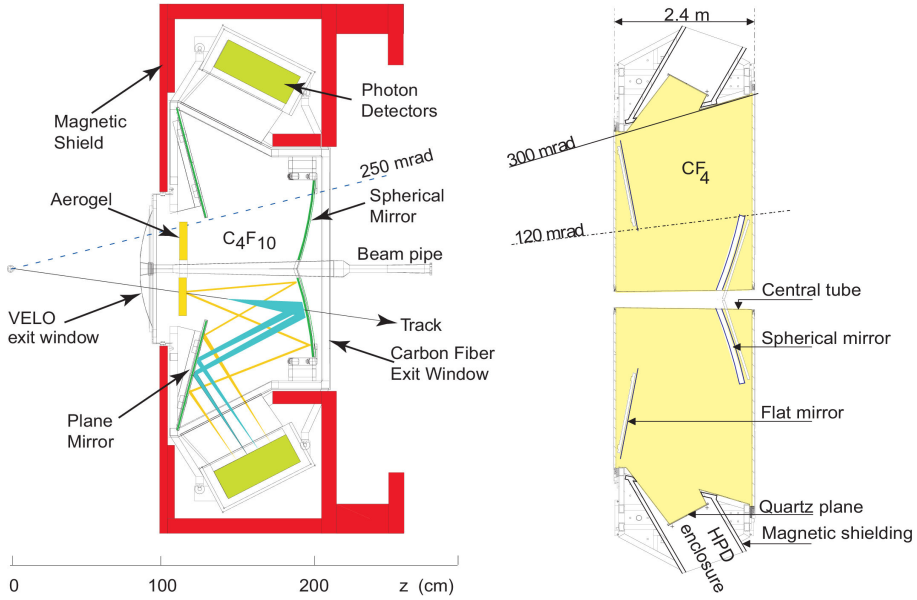


Figure 2.10: Schematic view of the RICH1 (left) and RICH2 (right) detectors.

2.3.5 RICH

There are two RICH detectors [37] in LHCb. RICH1 is located before the magnet (between the VELO and TT) and is used for identification of low momentum particles. RICH2 is located behind the magnet (between OT and M1) and is used for the identification of high momentum particles. The combination of both detectors allows for kaon and pion separation in the momentum range $2 < p < 100 \text{ GeV}/c$.

The RICH detectors measure the opening angle of the Cherenkov emission cone produced by a charged particle that traverses the medium. The photon emission is focused on the detector surface using a combination of spherical and flat mirrors. The mirrors are tilted to allow the photo detectors to be positioned outside the active area of the detector.

The Cherenkov emission angle θ is given by:

$$\cos \theta = \frac{1}{n\beta}, \quad (2.1)$$

where n is the refractive index of the radiator medium and $\beta = v/c$ is the velocity of the particle. Given the momentum p of a particle and the emission angle θ , the particle mass and therefore the type can be determined.

The RICH1 and RICH2 detectors have different effective momentum ranges, which are determined by the corresponding radiator emission threshold velocity $\beta_{thr} = 1/n$. The RICH1 detector uses a combination of aerogel and C_4F_{10} gas radiators and covers the low momentum range $1 < p < 60 \text{ GeV}/c$. The RICH2

detector uses a CF_4 radiator and covers the high momentum range $15 < p < 100 \text{ GeV}/c$.

2.3.6 Calorimeters

The calorimeter system [38] is designed to measure the energy and position of hadrons, electrons and photons. This information is used in the first level trigger (L0) as well as in the offline analysis.

The calorimeter system is located between the RICH2 and muon detectors and consists of a scintillator pad detector (SPD), a pre-shower detector (PS), an electromagnetic calorimeter (ECAL) and a hadronic calorimeter (HCAL). The SPD and PS are located in front of the ECAL and provide information on the evolution of the electromagnetic shower. The ECAL serves to measure the energy of electrons and photons, whereas the HCAL measures the energy of hadrons.

When a particle hits the calorimeter, it produces a cascade of secondary particles. These secondary particles excite the scintillator material, which in turn emits the scintillation light. The light is transmitted through wavelength-shifting fibers to the photo-multiplier tubes. The total amount of light collected by photo-multipliers is proportional to the energy of the incident particle.

The SPD and PS consist of scintillator pads, separated by a 15 mm thick lead converter. The SPD is used for identification of charged particles before the start of the shower. The lead converter initiates the shower that subsequently is detected by the PS. The SPD allows to separate electrons from photons, whereas the PS is used for separation of electrons and photons from hadrons.

The ECAL consists of lead-scintillator modules and covers the acceptance of $25 < \theta_x < 300 \text{ mrad}$ and $25 < \theta_y < 250 \text{ mrad}$ in the horizontal and vertical planes, respectively. Each module is 42 mm thick and consists of alternating layers of 4 mm scintillator material and 2 mm lead absorber. The modules vary in size from $4 \times 4 \text{ cm}^2$ in the inner part of the detector, to $6 \times 6 \text{ cm}^2$ in the middle and $12 \times 12 \text{ cm}^2$ in the outer part of the detector. The energy resolution of ECAL for electrons and photons is:

$$\left(\frac{\sigma_E}{E}\right)_{ECAL} = \frac{10\%}{\sqrt{E[\text{GeV}]}} \oplus 1\%. \quad (2.2)$$

The HCAL is located behind the ECAL. The modules of the HCAL have dimensions of $13 \times 13 \text{ cm}^2$ and $26 \times 26 \text{ cm}^2$ in the inner and outer part of the detector, respectively, and consist of alternating layers of 1 cm thick iron and scintillators. The energy resolution of HCAL for hadrons is:

$$\left(\frac{\sigma_E}{E}\right)_{HCAL} = \frac{80\%}{\sqrt{E[\text{GeV}]}} \oplus 10\%. \quad (2.3)$$

2.3.7 Muon System

The LHCb muon system [39] is designed for muon identification and tracking. It provides information on the transverse energy of the muon to the first level trigger (L0) and muon-ID for the second level trigger (HLT) and offline analysis.

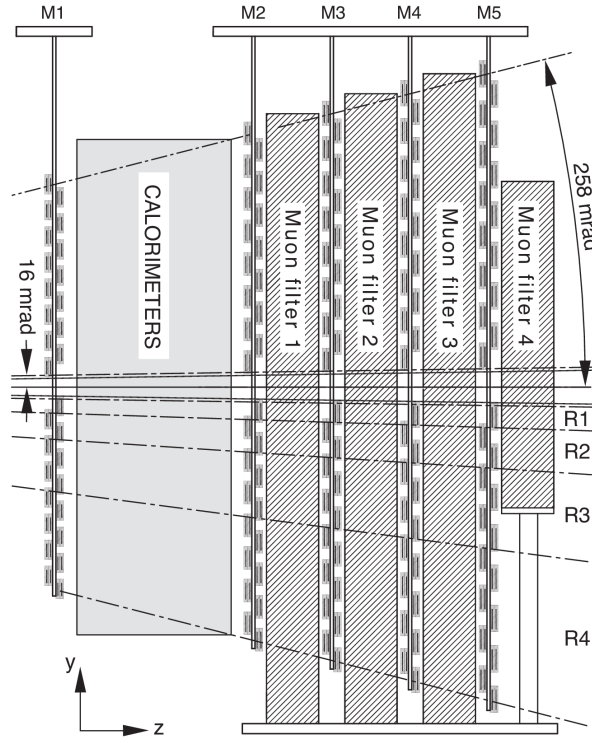


Figure 2.11: Schematic view of the muon system.

The muon system is composed of five stations (M1–M5) placed along the beam axis (Fig. 2.11). Stations M2 to M5 are placed downstream of the calorimeters and are interleaved with iron absorbers. The M1 station is located in front of the SPD/PS and is used to improve the transverse momentum estimate in the trigger.

Each station is divided into four regions, R1 to R4, with increasing distance from the beam axis. The granularity of each region is made according to the particle flux, keeping the channel occupancy roughly constant over the four detector regions. For more precise momentum measurement the granularity is higher in the horizontal plane.

2.4 Trigger

The LHCb trigger system [40] is used for the selection and storage of events for LHCb physics studies. The general layout of the trigger is shown in Fig. 2.12.

The first level trigger Level-0 (L0) is implemented in hardware. The L0 trigger decision is based on the information of the calorimeter and muon systems. Both systems provide information on the multiplicity, and transverse energy E_T or transverse momentum p_T of individual particles.

The High Level Trigger (HLT) is the second level trigger of LHCb. The HLT is

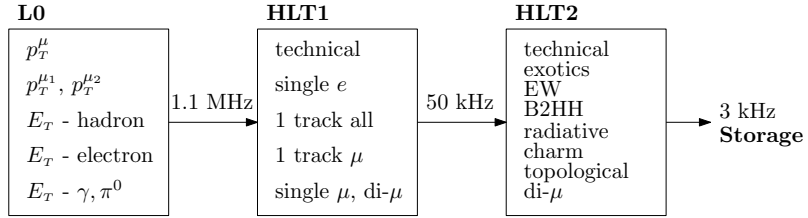


Figure 2.12: Schematic overview of the LHCb trigger.

a software trigger that runs on about 15000 processors of the Event Filter Farm. The HLT, with its two stages HLT1 and HLT2, reduces the 1 MHz L0 rate to about 3 kHz which is put on storage.

HLT1 reduces the rate from 1 MHz to 50 kHz. HLT1 performs the reconstruction of particles in the VELO and determines the location of primary vertexes and impact parameters (IP) of the particles. The events are selected based on the presence of particles which pass the requirements on the minimum track quality, IP, momentum, and transverse momentum. These selections are based on the decay kinematics of charm and beauty hadrons, such as:

- high average momentum and transverse momentum of charm and beauty hadrons, and consequently their decay products;
- the decay vertex is well displaced from the collision (primary) vertex, and consequently the reconstructed final state particles on average do not point to the primary vertex.

HLT2 reduces the rate from 50 kHz to 3 kHz and is mainly based on inclusive trigger lines that cover most of the B decays with displaced vertexes. In addition, HLT2 contains trigger lines based on the presence of muons and lines aiming at selecting exclusive B decays. HLT2 uses similar requirements on the particles as HLT1, in addition to which the requirements on distance between primary and secondary vertexes, vertex quality, mass and lifetime are used.

2.5 LHCb 2010 and 2011 operation

In 2010 and 2011, LHC operated at $\sqrt{s} = 7$ TeV. During these run periods LHCb operated at a significantly higher average number of interactions per bunch crossing, reaching $\mu = 2$, compared with the design value of $\mu = 0.4$. To cope with the higher pile-up conditions the trigger system was re-adjusted several times during data-taking.

Figure 2.13 shows the luminosity delivered and recorded by LHCb in the 2010 (left) and 2011 (right) data-taking periods. In 2010, the luminosity increased approximately exponentially with time, as the number of protons per bunch, and the

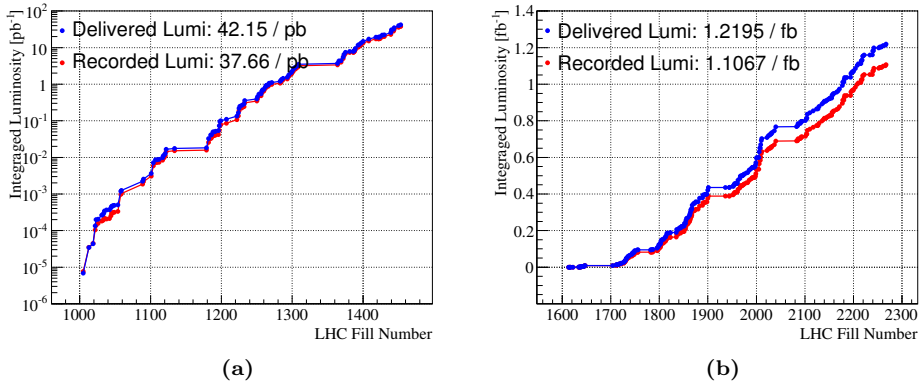


Figure 2.13: Delivered and recorded luminosity to LHCb in 2010 (a) and 2011 (b).

number of bunches per beam increased. In 2011, the operation conditions and luminosity were relatively stable and the total recorded luminosity amounts to 1.1 fb^{-1} , which is close to the originally planned value.

The data used in the analysis presented in this thesis correspond to the first 15 nb^{-1} collected under low pile-up conditions in 2010 with a so-called micro bias trigger. The micro bias is based on the minimum bias trigger with at least one reconstructed track in VELO or T-stations. This trigger essentially selects non-empty unbiased events that are particularly suitable for cross section measurements.

Chapter 3

Outer Tracker simulation

An accurate description of the detector geometry is essential for event simulation and reconstruction. Due to the use of different detector technologies, each sub-detector has its own digitization software that is used to simulate the detector response of the electronics.

In this chapter the simulation and digitization of the Outer Tracker (OT) is described. Section 3.1 describes the detector geometry and numbering scheme used in the OT software. In Section 3.2 the simulation of the OT detector response is discussed, as well as differences with respect to the real detector. The chapter is concluded with a short summary in Section 3.3.

3.1 Detector description

The detector geometry, described in the GAUDI [41] detector description framework, follows closely the actual design of the detector. The location of sensitive elements as well as the inactive material distribution is an important ingredient of the GEANT [42, 43] simulation. The detector description is also extensively used in the OT signal digitization and track reconstruction software. For example, the estimated precision of the measured track parameters crucially depends on the amount of material traversed by the charged particle.

The detector geometry is described by a set of nested volumes that can have any shape, position and material composition. The OT geometry has a tree-like structure that closely follows the physical detector geometry. The details of geometry and alignment procedure can be found elsewhere [44].

The OT is divided into three stations numbered from one to three (T1–T3). Each station is described as a box, with a central hole that accommodates the inner tracker and the beam pipe. It contains four layers positioned in a $x-u-v-x$ stereo configuration that are numbered from zero to three (L0–L3). Table 3.1 shows the coordinates of the centers of 12 OT layers. The x layers have modules positioned vertically along the y -axis, whereas the u and v layers have modules placed at stereo angles -5° and $+5^\circ$ with respect to the vertical y -axis in the xy -plane. The layers are further divided into quarters numbered from zero to three (Q0–Q3). Each

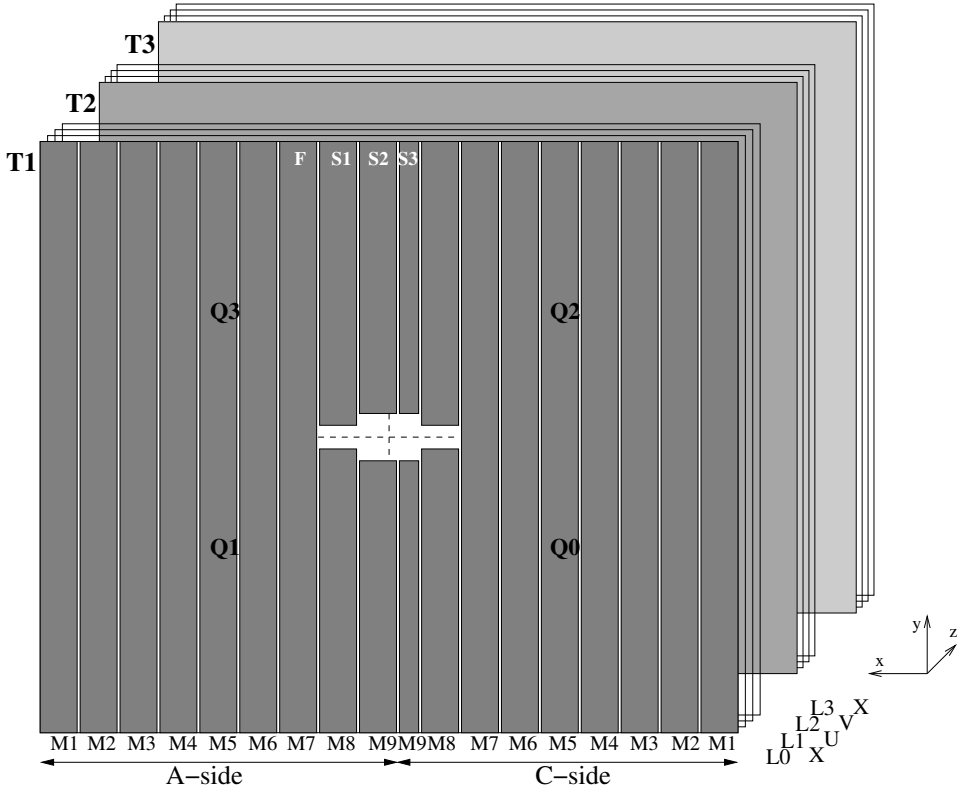


Figure 3.1: Numbering scheme of OT first layer X1. The layer is divided into four quarter, numbered from Q0 to Q4, each containing 9 modules, numbered from M1 to M9. Other layers have same numbering scheme.

	T1		T2		T3	
	y [mm]	z [mm]	y [mm]	z [mm]	y [mm]	z [mm]
x (L0)	28.4	7860.75	30.9	8542.75	33.3	9227.75
u (L1)	28.4	7915.25	30.9	8597.25	33.3	9282.25
v (L2)	28.8	7980.75	31.3	8662.75	33.8	9347.75
x (L3)	28.8	8035.25	31.3	8717.25	33.8	9402.25

Table 3.1: The coordinates of the centers of 12 OT layers. The increase of y positions reflects the tilt of the LHC beam line with respect to the horizontal plane.

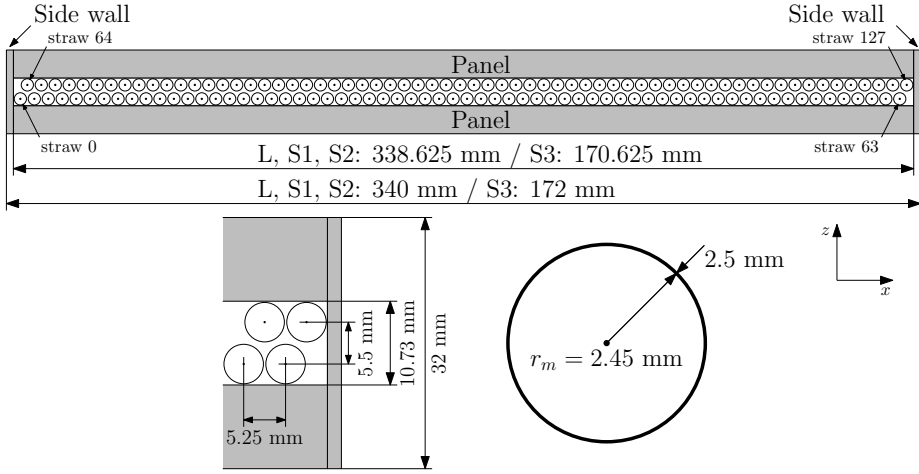


Figure 3.2: Top view of the module. The module consist of two staggered mono-layers of straws.

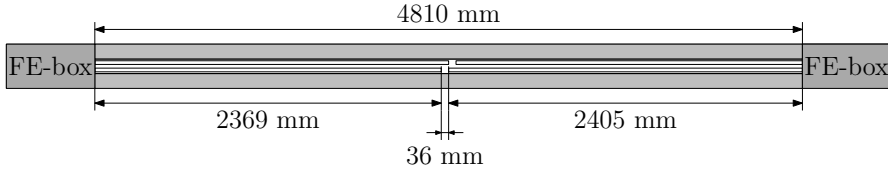


Figure 3.3: Side view of the F-module showing the location of front-end boxes. The mono-layers are staggered in the longitudinal direction to avoid a dead region at the center.

quarter consist of nine modules: seven half F-modules (M1–M7), called L-modules, and two short S-modules (M8 and M9). The S-modules have different length and are named S1 and S2 for the A-side ($x < 0$), and S1 and S3 for the C-side ($x > 0$) quarters. The numbering scheme and locations of the stations are illustrated in Fig. 3.1.

Each module consists of two staggered mono-layers, as shown in Fig. 3.2 and Fig. 3.3. Each mono-layer consist of 64 straws placed in a row. They are numbered from 0 to 63 for the first mono-layer and from 64 to 127 for the second mono-layer. The S3 modules have only 32 straws per mono-layer.

The smallest volume implemented in the geometry corresponds to the individual OT module. This granularity allows to align the OT at the level of modules that have spatial and angular degrees of freedom in the corresponding alignment database. The module geometry description is represented as a set of five sub-volumes: one containing the straws, sandwiched between two panel volumes, and

two side-wall volumes. The straw volume is defined as sensitive detection volume, whereas panels and walls only contain passive material. In the simulation the interaction with the sensitive volumes is recorded and can be further used in the digitization. The passive volumes are essential to simulate multiple scattering and energy loss of the traversing particles, and to correct for these effects in the reconstruction.

3.2 Digitization

The OT read-out electronics measures the drift time of the ionization clusters produced by a particle traversing the straw, relative to the collision time. The time when the signal reaches the detector read-out relative to the collision time is:

$$t_{TDC} = t_{tof} + t_{drift} + t_{prop} + t_{FE}, \quad (3.1)$$

where t_{tof} is the particle's time-of-flight, t_{drift} is the drift time of the ionization cluster inside the straw towards the anode wire, t_{prop} is the propagation time of the signal along the wire to the read-out electronics, and t_{FE} is the signal travel time to the TDC input inside the FE box.

The following sequence of steps constitutes the simulation/digitization procedure of the OT:

- determination of the straws that are hit by a particle and the distances from the particle trajectory to the wire for these straws;
- simulation of the cell efficiency depending on the straw-particle geometry;
- calculation of the drift time corresponding to these distances;
- simulation of the drift time resolution effect;
- simulation of the cross-talk, noise and double pulses;
- addition of spill-over hits from previous or later bunch crossings;
- simulation of the start of the TDC time measurement;
- simulation of the analog dead time effect due to the amplifier chip characteristics and the read-out scheme;
- conversion of the time to a digital representation.

All these steps are discussed further in detail.

Time-of-flight

The time-of-flight t_{tof} is obtained from GEANT and is the time difference between the arrival time of the particle at the straw and the collision time. In the real detector the time-of-flight is calculated assuming that the particle travels with the speed-of-light, which is a good approximation given the energies of produced particles.

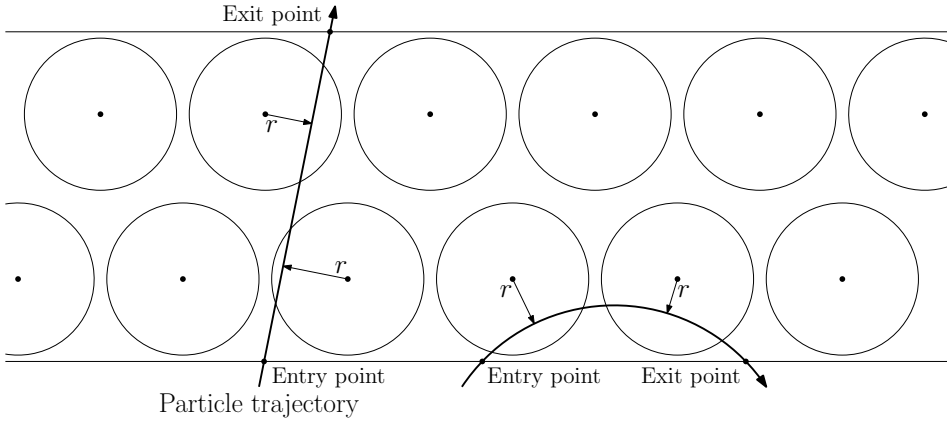


Figure 3.4: The schematic view of the particles crossing the module. The entry and exit points of particles are provided by GEANT and are used for calculation of the distance from the particle to the wire, as explained in the text.

Drift distance

As there is no description of individual straws in the detector geometry, the entry and exit points of the particles in the active volume together with the known locations of the straws in this volume are used to calculate which straws are hit, and at which distances to the wire the particle passes the straws, assuming a straight particle trajectory in the volume. The entry and exit points are provided by GEANT and are schematically shown in Fig. 3.4.

This procedure is only valid for high momentum particles that go through the module, which is not always the case. For example, low momentum particles can bend significantly under the influence of the magnetic field, and the entry and exit points can be located in the same mono-layer ($z_{\text{entry}} = z_{\text{exit}}$). For these particles the trajectory is assumed to be circular and perpendicular to the magnetic field. These particles are mainly produced in secondary interactions with the detector material and are regarded as background.

Cell efficiency

When the particle passes the straw it produces ionization clusters. The number of primary ionizations produced by the particle is distributed following a Poisson distribution and the probability to produce n primary encounters is given by

$$P(n) = \frac{\mu^n}{n!} e^{-\mu}, \quad (3.2)$$

where $\mu = l/\lambda$ is the average number of primary ionizations produced by a particle over a given path length l in a gas with an average ionization length λ . For a particle passing the straw at a distance r from the wire, the path length in the

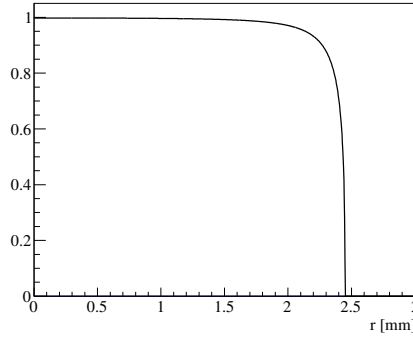


Figure 3.5: Hit efficiency profile corresponding to $\lambda = 0.8$ mm.

straw is given by

$$l(r) = \frac{2\sqrt{r_m^2 - r^2}}{\sin(\theta)}, \quad (3.3)$$

where $r_m = 2.45$ mm is the inner radius of the straw and θ is the angle between the particle trajectory and the wire (typically θ is close to 90°).

The probability to register a particle that passes the straw at a distance r from the wire can be derived assuming that it is given by the probability to register at least one ionization cluster:

$$\varepsilon(r) = P(n \geq 1) = 1 - P(n = 0) = 1 - \exp\left(-\frac{l}{\lambda}\right) = 1 - \exp\left(-\frac{2\sqrt{r_m^2 - r^2}}{\lambda \sin(\theta)}\right), \quad (3.4)$$

where $P(n \geq 1)$ and $P(n = 0)$ are the probabilities to produce at least one and zero ionization clusters, respectively.

The average ionization length in a gas mixture with 70% Ar and 30% CO₂, used in OT, is about $\lambda = 0.3$ mm [45]. However, in a real detector, due to electron recombination and inefficiency of the read-out electronics to register the signal, the effective ionization length is larger. In the OT digitization the following hit efficiency profile is used:

$$\varepsilon(r) = \varepsilon_0 \left(1 - \exp\left(-\frac{2\sqrt{r_m^2 - r^2}}{\lambda_{eff} \sin(\theta)}\right) \right), \quad (3.5)$$

where ε_0 is an efficiency plateau and λ_{eff} is an effective ionization length. Figure 3.5 shows the cell efficiency profile for $\varepsilon_0 = 1$ and $\lambda_{eff} = 0.8$ mm (see next chapter for a determination of λ_{eff}).

Equation (3.5) is used to simulate the probability for a particle to leave a hit in a straw. Note that there is no actual simulation of individual ionization clusters.

Drift time

The drift time is the time for the ionization cluster to reach the anode wire and is calculated as a function of the drift distance. For the simulation, the drift distance is defined as the closest distance between the particle and the wire. Although the closest ionization might occur further from the wire than this closest distance, this is a good approximation as the ionization length is relatively small and the bias is only sizable when the particle passes the straw close to the anode wire. The size of this effect will be discussed in the next chapter.

The conversion from the distance to the drift time in the digitization is performed by a distance-to-time relation (TR-relation). The TR-relation is extracted from the data and the procedure is discussed in detail in the next chapter. In the digitization the TR-relation has a second order polynomial form, which is taken from the beam test of 2005 [46]:

$$t(r) = 20.1 \frac{r}{r_m} + 14.4 \frac{r^2}{r_m^2} \quad (3.6)$$

where r is the distance between the particle and the wire, and $r_m = 2.45$ mm is the inner radius of the straw tube. Note that the maximum drift time is about 35 ns.

Drift time resolution

To simulate a realistic spread in the measured times, t_{TDC} is smeared in the digitization according to a Gaussian distribution. The width of the distribution is defined as a function of the distance between the particle and the wire. The resolution is determined from data and the procedure is discussed in detail in the next chapter. Figure 3.6 shows the drift time distributions before and after the smearing, performed by a Gaussian with a width of 3 ns, which is close to the average drift time resolution in data.

In an ideal detector the resolution is expected to be independent of the distance from the particle to the wire, however, this is not the case due to residual detector

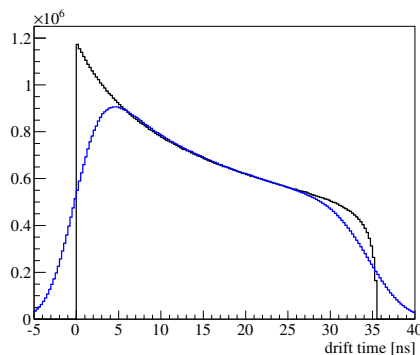


Figure 3.6: Drift time distributions before and after smearing. Note that drift time spectrum before smearing includes the cell efficiency effect.

misalignment (see Section 4.6). In addition, due to the fact that ionization clusters are distributed along the particle trajectory, the resolution deviates from a Gaussian shape.

Propagation time

The propagation time t_{prop} is determined from the distance between the hit and the read-out electronics along the straw. Assuming a constant propagation velocity, the propagation time is:

$$t_{prop} = \frac{|y_{read-out} - y_{hit}|}{v_{prop} \cdot \cos(\theta_{stereo})}, \quad (3.7)$$

where $y_{read-out}$ and y_{hit} are the y -coordinates of the read-out and of the hit, respectively, θ_{stereo} is the stereo angle of the straw, which is $\pm 5^\circ$ for L1 and L2 layers, and $v_{prop} = 4 \text{ ns/m}$ is the signal propagation velocity [47].

In the real detector the time measurement relies on the discriminator pulse, and therefore the measured time, i.e. the time when the signal passes the threshold, depends on the signal amplitude (this is commonly called “walk”). Consequently, those parts of the detector with systematically larger pulse height appear as if the propagation time is smaller than expected. The details of this effect will be discussed in next chapter.

Cross-talk, noise and double pulses

In addition to signal hits produced by real particles (including spill-over hits), also hits from noise and cross-talk are simulated. Cross-talk is a fake (spurious) hit which is not caused by a real particle crossing the straw, but is induced by a signal in a neighboring channel. This effect occurs in the straws, as well as in the amplifier and the TDC input. Its combined effect was measured in 2005 beam test [46] and was determined to be less than 4% per straw for straws in the same mono-layer, whereas the cross-talk between mono-layers was determined to be negligible (less than 1%). In the digitization the cross-talk is set to 5% for straws in the same mono-layer and no cross-talk is simulated between the mono-layers.

Noise hits are not caused by real particles and originate from the noise in the read-out electronics. The constant level of noise is simulated in the OT at the level of 10 kHz for every straw. This noise level gives a probability of having a noise hit within a considered time window of 75 ns equal to $10^4 \text{ kHz} \cdot 75 \text{ ns} = 75 \cdot 10^{-5}$, which corresponds to an occupancy below 0.1% per straw.

In addition to the direct signal from the particle, consecutive signals in the same channel can be produced. These so-called double pulses originate from multiple ionization clusters, signal reflection and photon feedback. In the last case the photon is emitted close to the anode wire and hits the straw wall, producing a new ionization cluster. This ionization cluster from photon feedback will, if registered, produce a second signal about 35 ns later, equal to the maximum drift time from the straw to the wire.

The double pulses are observed in data and are implemented in the digitization as a probability to register a second signal after a given time. The average probability to have a double pulse following a real hit, as estimated from real data [48], is about 30%.

Spill-over

The LHC operates at a bunch crossing intervals of 25 ns or 50 ns. Consequently, some particles produced in previous (or later) bunch crossing will contribute to the current event of interest. In particular, the hits with a long drift time in previous bunch crossings and with a short drift time in later bunch crossings are observed in the TDC spectrum. These hits are called spill-over hits. The measured time for spill-over hits is:

$$t_{TDC} = t_{tof} + t_{drift} + t_{prop} + t_{FE} + t_{spill}, \quad (3.8)$$

where t_{spill} is the time of the spill-over bunch crossing relative to the current one. There are in total five spills, including the current one, that are considered in the OT digitization: the so-called Prev-Prev, Prev, Current, Next and Next-Next, corresponding to time offsets of -50, -25, 0, 25 and 50 ns, respectively. Figure 3.7 shows the t_{TDC} distribution of hits from Prev-Prev, Current and Next-Next spills for simulated events with 50 ns bunch spacing for station T3. Note that each spill is simulated with the same pile-up conditions.

Although the spill-over hits are produced by real particles, their trajectories are typically not well reconstructed, since part of the hits fall outside of the read-out window and are not retrieved during read-out or, alternatively, do not correctly

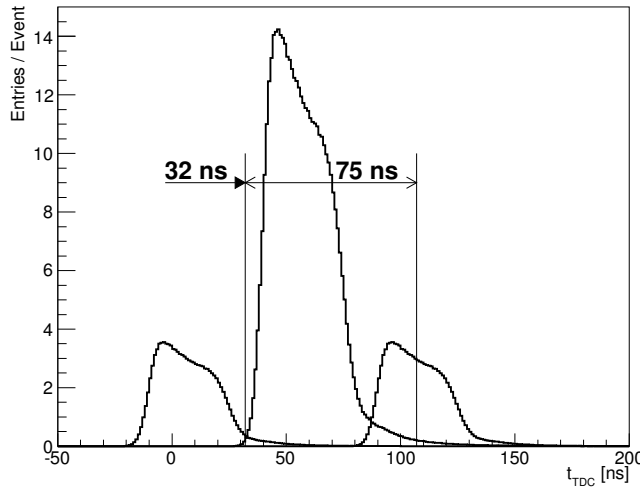


Figure 3.7: Distribution of t_{TDC} for Prev-Prev, Current and Next-Next spills for simulated events with 50 ns bunch spacing for station T3. The 75 ns wide read-out window, starting at 32 ns, is indicated.

line up after t_0 correction for the current spill. Therefore, these hits are regarded as background.

Start of the time measurement

The start of the time measurement, t_{clock}^{FE} , defines the phase of the TDC clock relative to the collision time. The time measured by the front-end (FE) electronics, therefore, is:

$$t_{TDC} = t_{tof} + t_{drift} + t_{prop} + t_{spill} - t_{clock}^{FE}. \quad (3.9)$$

In the OT digitization the values of t_{clock}^{FE} are set to the time that it takes for a particle (traveling with the speed of light) to reach the center of the station. This corresponds to the values of 28 ns, 30 ns and 32 ns for T1, T2 and T3, respectively. In Eq. (3.9) t_{FE} is assumed to be the same for all channels in simulation, and it is effectively absorbed in the t_{clock}^{FE} .

Dead time

The read-out electronics consist essentially of an amplifier (ASDBLR - Amplifier Shape Discriminator with Base Line Restoration) and a time-to-digital converter (OTIS - OT Time Information System). The signal from the wire is amplified and discriminated against a threshold value in ASDBLR. The time when the signal passes the threshold is measured relative to the collision time by the OTIS and is converted to a 6-bit TDC time.

Several features from the electronics are described in the digitization. First, there is a dead time that corresponds to the time that it takes to process the signal in the amplifier chip. During this period any subsequent signal is ignored. The amplifier has a dead time ranging between 10 and 15 ns (depending on the input signal characteristics). However, the OTIS TDC can only digitize one hit per bunch crossing, which essentially sets the effective dead time to 25 ns.

Given the maximum drift time of about 35 ns and the maximum propagation time of about 10 ns, and ignoring variations in the time-of-flight, the maximum detection time is 45 ns. This time range falls within the read-out window of two bunch crossing, however, to accommodate for resolution effects and collect the hits from current bunch crossing with high efficiency, the read-out window of the OTIS is set to three bunch crossings (75 ns). The read-out scheme of the TDC chip is designed to only record the first hit within the 75 ns wide read-out window¹. Effectively, this gives a dead time of up to 75 ns.

Time-to-digital conversion

The final step in the digitization is the conversion of the “measured” time t_{TDC} to the digital 6-bit TDC time relative to each 25 ns bunch crossing, resulting in a step size of $25 \text{ ns}/64 \approx 0.4 \text{ ns}$. In addition, 2 bits encode the bunch crossing number

¹Another read-out scheme allows to record the hits in every bunch crossing, but is not used for data taking.

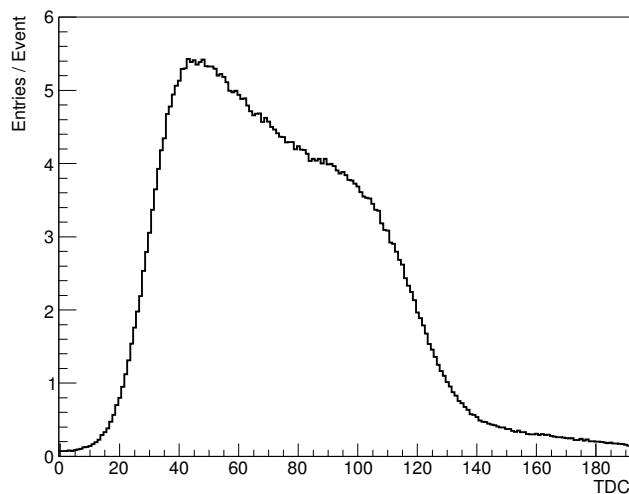


Figure 3.8: TDC spectrum of simulated hits in T3.

within the 75 ns read-out window. In total there are 192 TDC bins that cover a time range of 75 ns. The TDC value, n_{TDC} , is therefore:

$$n_{TDC} = t_{TDC} \cdot \frac{192}{75}, \quad (3.10)$$

where n_{TDC} is rounded to the closest integer. Figure 3.8 shows a TDC spectrum of simulated hits in station T3.

3.3 Summary

In this chapter the simulation and digitization of the OT has been described. In the next chapter the timing calibration, including the t_0 , walk, TR-relation and resolution calibration, is described. The TR-relation and resolution, obtained from data, are used in the OT simulation to provide an accurate and realistic detector response.

Chapter 4

OT calibration

The track reconstruction algorithm finds charged particle trajectories using information from different detectors. The hits from VELO, TT, IT and OT are combined and used in the track fitting algorithm to obtain the best estimate for the track parameters. About 70% of the reconstructed tracks pass through the active area of the OT, and for these tracks about half of the hits (measurements) are provided by the OT. These hits contribute mainly to the momentum estimate of the particle and the trajectory slope determination in the RICH detectors. The calibration of the OT, which includes timing and spatial alignment, allows to improve the single hit resolution, consequently improving the precision of the track-parameter estimates.

In this chapter the timing calibration of the OT is discussed. Section 4.1 gives an overview of the time measurement and describes the contributions of different sources to the hit resolution. These procedures are t_0 calibration, walk correction and TR-relation calibration, and are described in Sections 4.2 to 4.4, respectively. In Section 4.6 a mono-layer shift and its effect on the resolution are discussed. Finally, in Section 4.7 the stability of the calibration parameters and the achieved resolution are discussed.

4.1 The OT time measurement

The track reconstruction software uses the hit information from different detectors to reconstruct the particle trajectories. Different types of tracks are defined based on their hit composition or, equivalently, on the detectors that the particle traversed. The most interesting tracks pass through the VELO, TT and IT/OT stations. The particles corresponding to these tracks are mainly produced in primary collisions and in decays of short lived intermediate particles, such as B and D mesons. Most of the physics analyses rely on these tracks.

The OT measures the time corresponding to the ionization cluster produced by the charged particle passing the straw. The measured TDC time is defined as the time difference between the LHC clock and the time of the hit as recorded by the TDC. It includes the time-of-flight of the particle to reach the straw from the

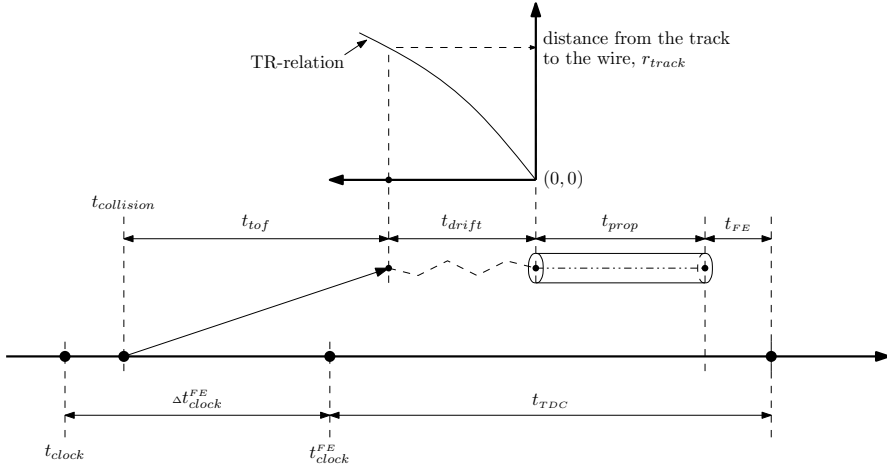


Figure 4.1: OT time diagram, showing the schematic of all contributions to the measured TDC time in the OT. The various contributions are described in the text. Note that the time scales are arbitrary.

collision point, the drift time of the ionization cluster produced by the particle to reach the wire, the propagation time of the signal along the wire to the module front-end and a combination of readout electronics delays.

Figure 4.1 shows the time diagram with all contributions to the measured TDC time. The relation between these contributions can be written as:

$$t_{TDC} = t_{collision} + t_{tof} + t_{drift} + t_{prop} + t_{FE} - t_{clock}^{FE}, \quad (4.1)$$

where t_{clock}^{FE} is the phase of the clock at the TDC input, $t_{collision}$ is the collision time, t_{tof} is the time of flight from the collision point to the straw, t_{drift} is the drift time, t_{prop} is the propagation time along the wire to the readout, t_{FE} is the hit signal transit time inside the FE box to the TDC input, and t_{TDC} is the measured drift time difference.

In the detector the reference time for the TDC is provided by the LHC bunch crossing clock signal t_{clock} , which is provided by the LHC clock distribution system [49]. The clock signal is distributed to the various sub-detectors by the LHCb Timing and Fast Control (TFC) system.

Figure 4.2 shows a schematic view of the OT clock distribution system. The OT receives the LHC clock signal from the TFC separately for the two detector sides (OTA and OTC) through 120 m fiber cables, which introduce in first approximation a constant delay to t_{clock} . For both sides the timing signal is then distributed to 12 control boxes (CB) through 20 m fiber cables. There are two control boxes per C-frame (top and bottom), each servicing 18 front-end (FE) boxes. Each control box allows to adjust the clock phase in the range from 0 to 25 ns. The signal from each control box to the FE boxes is distributed through equal-length SCSI cables of about 6.5 m length.

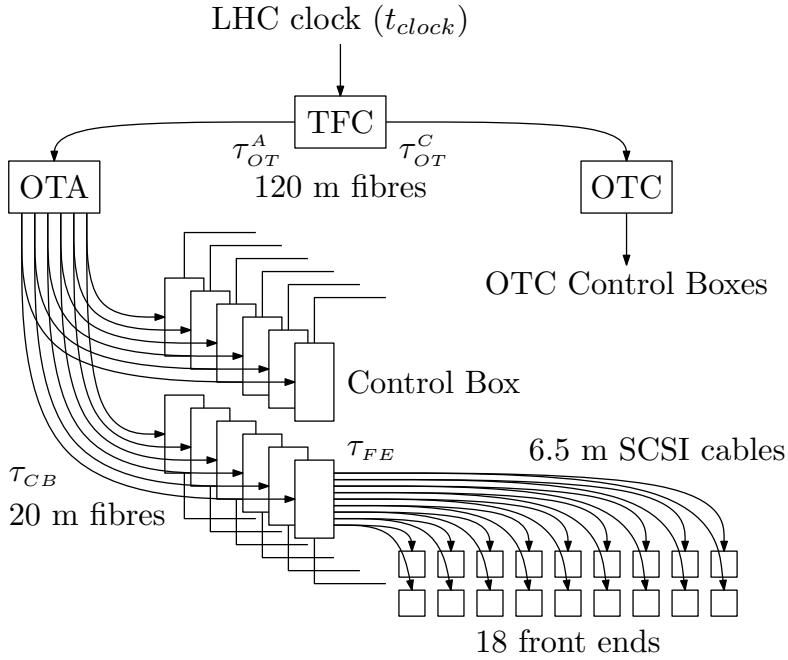


Figure 4.2: OT clock distribution system. The LHC clock (t_{clock}) is distributed through TFC to two detector sides: OTA and OTC. For both sides the signal is distributed to individual front-ends through 12 control boxes. The τ_{OT} and τ_{CB} are cable delays, and Δt_{CB} is a delay in the control box. The τ_{FE} is a combination of the signal transit time inside the control box, in the cable between the CB and the FE, and inside the FE box to the TDC clock input.

The t_{clock}^{FE} value for the arriving clock signal at the FE is therefore:

$$t_{clock}^{FE} = t_{clock} + \Delta t_{clock}^{FE} \approx t_{clock} + \tau_{OT}^{\{A,C\}} + \tau_{CB} + \Delta t_{CB} + \tau_{FE}, \quad (4.2)$$

where τ_{OT} and τ_{CB} are cable delays, and Δt_{CB} is a delay that can be set in the control box. The τ_{FE} is a combination of the signal transit time in the control box, in the cable between the CB and the FE, and inside the FE box to the TDC clock input.

Neglecting the difference in the cable lengths, the main contribution to the timing differences for the arriving clock signal, t_{clock}^{FE} , between different FEs originates from the differences in the signal transit time in the control box, which can amount up to several ns.

As the t_{clock}^{FE} essentially defines the start of the TDC time, the variation in t_{clock}^{FE} leads to a shift in the TDC spectra for different FEs.

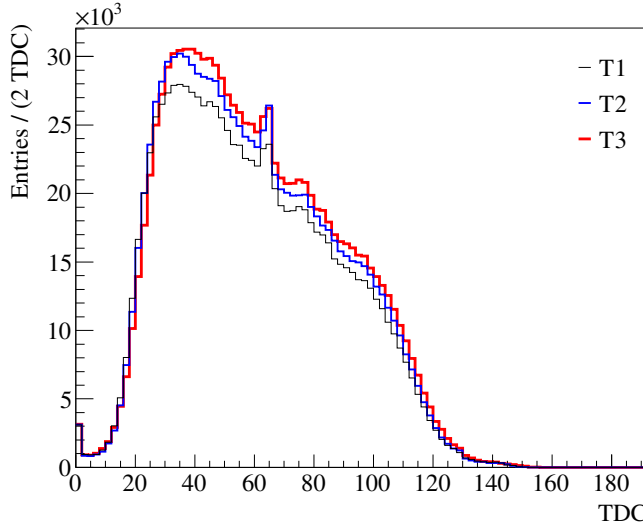


Figure 4.3: TDC spectra for station T1 (black), T2 (blue) and T3 (red). Each entry corresponds to the hit on track with momentum $P > 3.2 \text{ GeV}/c$ and $\chi_{ub}^2/N_{DoF} < 2$.

From Eqs. (4.1) and (4.2) the TDC time can be written as

$$t_{TDC} = (t_{collision} - t_{clock}) + t_0 + t_{tof} + t_{drift} + t_{prop}, \quad (4.3)$$

where

$$t_0 = t_{FE} - \Delta t_{clock}^{FE}. \quad (4.4)$$

The difference $t_{collision} - t_{clock}$ accounts for variations of the phase of the LHC clock received at the LHCb experiment control. This difference is found to be below 0.5 ns (see Section 4.7) and is further omitted. The t_{clock}^{FE} phases are set separately for each detector station, to compensate for the difference in the arrival times of the particles. The same Δt_{clock}^{FE} values are used for all module front-ends in the corresponding station. The current values are 28, 30 and 32 ns for T1, T2 and T3, respectively, reflecting their 0.7 m geometric separation. With these settings the TDC spectra start approximately at the same point as shown in Fig. 4.3. Note that the integrals of the spectra are not the same, as more secondary particles are produced in the downstream direction. In addition, in the upstream direction, due to higher occupancy in the middle of the station, more hits are masked, as only the first hit in the read-out window is recorded.

The time of flight from the collision point to the straw is calculated with the assumption that the particle is produced at the collision point and travels with the speed of light, which is a good approximation given the energies of the produced particles. The correction to the time of flight due to the bending in the magnetic field is calculated using the so-called “ p_T -kick” method [50, 51]. The value for t_{tof} is known with a precision better than 0.1 ns, as determined from MC simulations.

The drift time t_{drift} is the time that it takes for an ionization cluster produced by the particle to reach the wire. In the track fit the drift time is converted to a distance using the TR-relation, which maps the drift time to the closest distance from the track to the wire. The knowledge of the TR-relation is essential to achieve a good spatial resolution. The procedure for obtaining the TR-relation is explained in detail in Section 4.3.

The propagation time t_{prop} describes the time delay imposed by signal propagation along the anode wire and depends on the distance from the hit to the readout front-end and the signal propagation velocity. The distance from the hit to the readout front-end is obtained from the reconstructed track and is known with a precision better than 1 mm. Given the propagation velocity of about 4 ns/m [47] the contribution to the final time resolution is negligible. However, the “effective” propagation velocity is observed to be not constant and depends on the distance to the straw end. The source and the calibration of this dependence will be discussed in Section 4.4.

4.2 t_0 calibration

The t_0 values contain delays which can vary from one module front-end to another. The aim of the t_0 calibration is to find the optimal values for every module front-end. The t_0 values are obtained by minimizing the difference between the measured drift time t_{drift} and the estimated drift time, calculated using the TR-relation and the distance from the track to the wire. This drift time residual is defined as

$$\Delta t = t_{drift} - t(r), \quad (4.5)$$

where $t(r)$ is the drift time estimate and r is the distance from the reconstructed track to the wire.

To demonstrate the calibration of one module, a bias, Δt_0 , for the current t_0 value is assumed relative to the true t_0 value. In this case the measured drift time $t_{drift}^{(meas)}$ and “true” drift time $t_{drift}^{(true)}$ are calculated as:

$$t_{drift}^{(meas)} = t_{TDC} - t_{tof} - t_{prop} - t_0, \quad (4.6)$$

$$t_{drift}^{(true)} = t_{TDC} - t_{tof} - t_{prop} - t_0 - \Delta t_0, \quad (4.7)$$

and the measured value of the drift time residual can be written as

$$\begin{aligned} \Delta t^{(meas)} &= t_{drift}^{(meas)} - t(r) \\ &= t_{drift}^{(true)} - t(r) + \Delta t_0 \\ &= \Delta t^{(true)} + \Delta t_0, \end{aligned} \quad (4.8)$$

where $\Delta t^{(true)}$ is the “true” drift time residual.

The average of the “true” drift time residual should be zero, and therefore the average shift in the measured drift time is equal to a shift in the value of t_0 :

$$\Delta t_0 = \langle \Delta t^{(meas)} \rangle. \quad (4.9)$$

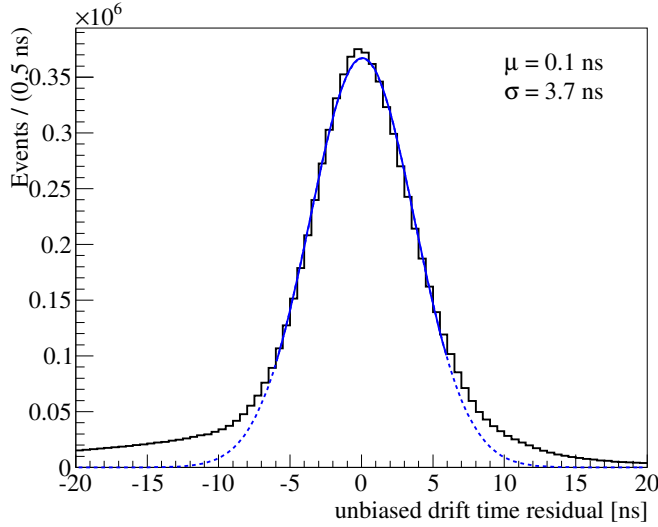


Figure 4.4: Unbiased drift time residual distribution for hits from tracks with a momentum $p > 3.2 \text{ GeV}/c$ and $\chi_{ub}^2/N_{DoF} < 2$. The solid line shows the Gaussian fit to the distribution in the region $\pm 6 \text{ ns}$. The dotted line shows the continuation of the fit function to the full range. μ and σ are the mean and sigma of the Gaussian fit.

Consequently the corrected t_0 value is

$$t_0^{(new)} = t_0 + \langle \Delta t^{(meas)} \rangle. \quad (4.10)$$

The value of $t_0^{(new)}$ is equal to $t_0^{(true)}$ only if the track parameters do not depend on the module hits for which t_0 is currently extracted. This is achieved by not including the hits of the corresponding module in the track fit. These hits are further referred to as unbiased hits. The track fit χ^2 with removed hits is linked to the unbiased hit and is called unbiased chi-square, χ_{ub}^2 . For each unbiased hit the drift time and the distance from the track to the wire are calculated and are referred to as unbiased drift time and unbiased distance, respectively.

Instead of using the average value of the drift time residuals, a fit to the distribution of unbiased drift time residuals is performed in a narrow range around the peak. This allows to reduce the contribution of incorrectly assigned hits¹. In addition, only hits with $\chi_{ub}^2/N_{DoF} < 2$ are used. Figure 4.4 shows the unbiased drift time residual distribution of all OT hits with this condition on χ_{ub}^2 and for tracks with momentum $p > 3.2 \text{ GeV}/c$. The background on the left and right sides of the distribution will be discussed later.

The calibration is performed for all 432 module front-ends in the OT. After the calibration the values of the t_0 change, which in turn leads to changes in the value of the track parameters, as the track fit is performed with new t_0 values. This can

¹Incorrectly assigned hits occur for example when two tracks traverse the same straw. In such a case only the first hit is recorded.

in turn lead to a bias in the extracted t_0 values. Consequently the calibration is performed in iterations, until the values of t_0 stabilize.

Figure 4.5 shows an example of the distribution of Δt values of all module front-ends, obtained at three consecutive iterations. At the third iteration the difference Δt becomes negligible for all modules and does no longer give any contribution to the change of track parameters. Usually the calibration is performed on a particular run starting from the calibration values of the previous run. The variation of t_0 values, from run to run, are expected to be small, and can only occur due to the drift in readout electronics delays or global time constants, such as drift in the difference $t_{\text{collision}} - t_{\text{clock}}$ (see Eq. (4.3)). Usually the differences between t_0 values from run to run are small and the number of iterations needed to converge is one or two. In this particular example the calibration was performed starting from the same t_0 value for all module front-ends, $t_0 = 0$ ns, and the calibration converged already after three iterations.

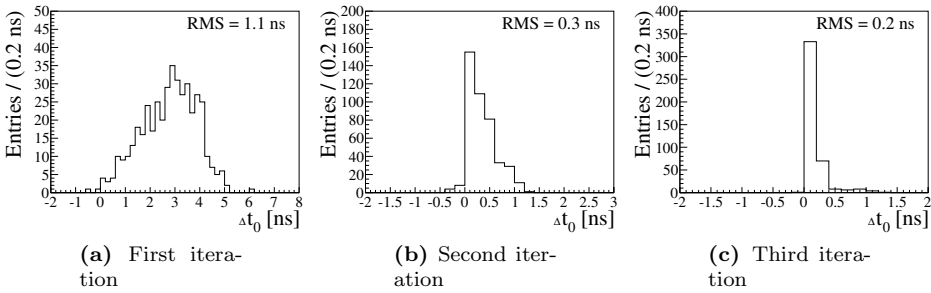


Figure 4.5: Distributions of Δt of all 432 module front-ends for three calibration iterations. The initial t_0 values, before the first iteration, are set to zero for all module front-ends, $t_0 = 0$ ns. Note the different scales along the axes.

The granularity of the calibration constants, i.e. one t_0 value per module front-end, was chosen as the electronics components inside a module front-end are identical and should not introduce a variation from one straw to another. The size of this straw-to-straw variation is discussed in Section 4.7. Figure 4.6 shows the value of t_0 versus the absolute module number, which is defined as:

$$n_{\text{module}} = m + 9 \cdot (q + 4 \cdot (l + 4 \cdot s)) \quad (4.11)$$

where m , q , l and s are the module, quarter, layer and station numbers, respectively (see Chapter 3).

As discussed above, the t_0 values include three different sources: the $\Delta t_{\text{clock}}^{FE}$ values, the synchronization between collision time and the LHC clock, and the electronics read-out delays. Since the $\Delta t_{\text{clock}}^{FE}$ values are set for each station and the LHC synchronization is better than 0.5 ns, the relative variation in t_0 values mainly corresponds to the variation in read-out electronics delays between module front-ends. This variation amounts to approximately 4 ns, as seen from the spread of

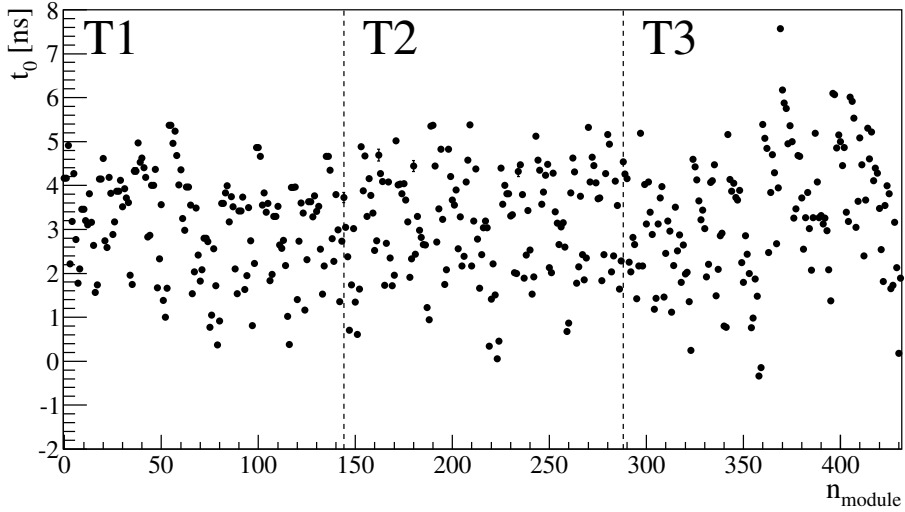


Figure 4.6: t_0 values for all 432 module front-ends versus the module number, n_{module} . t_0 is defined with respect to the $\Delta t_{\text{clock}}^{FE}$ values of the corresponding station.

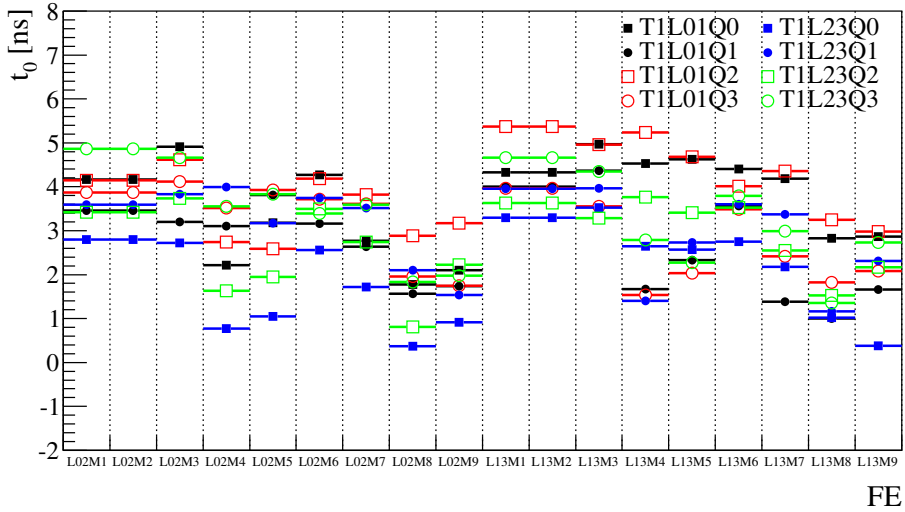


Figure 4.7: t_0 values versus the FE number for control boxes of station T1. Different data points indicate different control boxes.

data points in Fig. 4.6. Figure 4.7 shows the t_0 values versus the front end number for different control boxes of station T1. All control boxes have similar systematic shifts of t_0 versus the front-end number. These shifts amount to approximately 2 ns and are mainly due to the differences in cable lengths inside the control boxes, which are of the order of 0.5 m. The remaining differences between control boxes can be due to the distribution of the input clock signal from one control box to another.

4.3 TR-relation calibration

The TR-relation maps the measured drift time to the closest distance from the track to the wire. Figure 4.8 shows the schematic view of a particle passing the straw and producing ionization clusters along its path inside the straw. In ArCO₂ [45] the ionization length, λ , is approximately 0.3 mm.² The number of produced ionization clusters directly affects the hit efficiency profile, which quantifies the efficiency to see a hit from the track at a given distance to the wire. This means that the smaller the ionization length the higher the hit efficiency, as more ionization clusters are produced. After the ionization is produced the electrons drifts to the wire due to the electrical field between the wire and the straw. When the ionization cluster approaches the wire, the electrons ionize the gas due to the high electric field around the wire. Subsequently a signal is induced on the wire and propagates to the readout electronics. The signal is registered if it passes a threshold value of 800 mV of the module front-end discriminator, corresponding to a charge of about 4 fC. A variation of the signal height introduces a variation in the time when the signal passes the threshold and is considered to be the main contribution to the TDC resolution.

In the track reconstruction software an effective TR-relation is used. It only describes the relation between the drift time and the distance from the track to the wire, which differs from the distance to the ionization cluster. However, the readout electronics only records the first signal, which corresponds to the ionization cluster closest to the wire, and the difference between these two distances is small, except for the case when the particle passes the straw close to the wire.

The shape of the TR-relation is defined by the drift velocity of the ionization cluster inside the straw. The electric field increases towards the wire, leading to a non linear TR-relation. Currently a parabolic dependence is used.

The parameterization of the TR-relation can be extracted from the fit to the distribution of the measured drift time versus the reconstructed distance from the track to the wire. In addition to the TR-relation parameters the resolution dependence is extracted. This is done by constructing the TR-relation Probability

²The observed (effective) ionization length λ_{eff} is larger due to the fact that not all clusters reach the wire and/or not all induced signals pass the discriminator threshold. The value of the effective ionization length is discussed later in this section.

Density Function (PDF):

$$f_{TR}(t, r) = \int_{-r_m}^{r_m} G_t(t | t(r_0), \sigma_t(r_0)) \cdot G_r(r | r_0, \sigma_r) \cdot \varepsilon(r_0) \cdot dr_0 \quad (4.12)$$

where r_0 is the distance from the particle to the wire, $r_m = 2.45$ mm is the radius of the straw, and the integral describes the probability for the particle to pass the straw at any distance to the wire. The Gaussian functions G_t and G_r describe two contributions: the resolution $\sigma_t(r_0)$ with which the drift time t is measured, and the error σ_r on the reconstructed distance r from the track to the wire. $t(r_0)$ is the TR-relation parameterization, and the function $\varepsilon(r_0)$ gives the probability for the particle to produce at least one ionization cluster (see Eq. (3.5)). The detailed description of the TR-relation PDF, as well as the description of random hits, is given in Appendix A.

The initial parameterization for the TR-relation is taken from beam test results [46] and has the following quadratic form:

$$t(r) = \left(20.1 \cdot \frac{|r|}{r_m} + 14.4 \cdot \frac{r^2}{r_m^2} \right) \text{ ns}, \quad (4.13)$$

where r_m is the straw radius and r is the distance from the track to the wire. From this parameterization it can be seen that the maximum drift time is about 35 ns.

The fit is performed on the sample of unbiased hits from tracks with a momentum $p > 10$ GeV/ c and $\chi_{ub}^2/N_{Dof} < 2$. This selection reduces the contribution

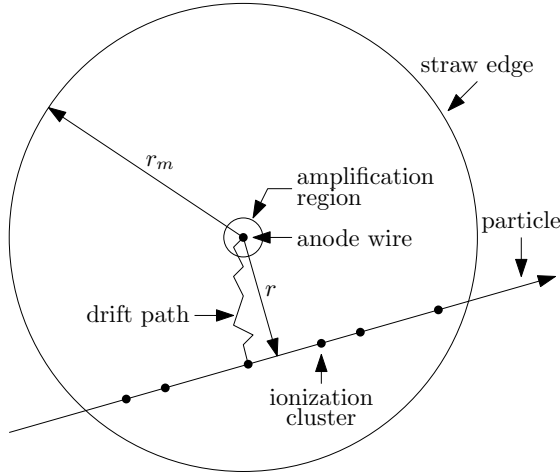


Figure 4.8: Schematic view of a particle passing the straw and producing ionization clusters. The ionization cluster electrons drift to the wire and induce the signal. Only the earliest signal is detected. The closest distance from the track to the wire, r , and radius of the straw, $r_m = 2.45$ mm, are also indicated.

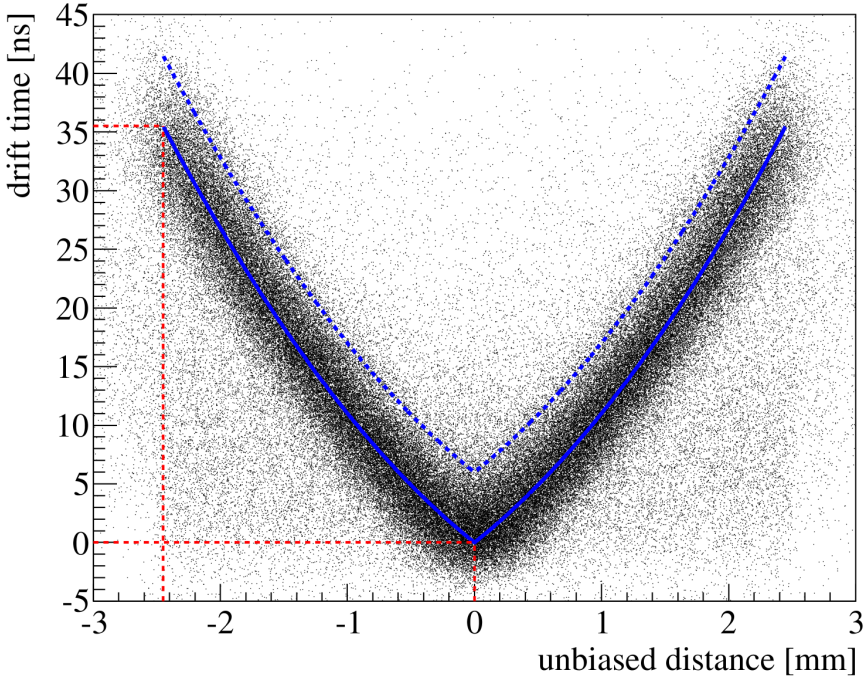


Figure 4.9: The drift time versus the unbiased distance distribution with the overlaid TR-relation curve, obtained from the fit (blue line). The red dotted lines show the points with minimum and maximum drift times. The blue dotted line illustrates the selection $\Delta t < 6$ ns.

of noise. In addition, the fit is constrained to the hits which satisfy the criteria on unbiased drift time residual $\Delta t < 6$ ns. The fit is performed in the range of $-5 < t_{drift} < 45$ ns and $|r| < 2.45$ mm.

The drift time versus the unbiased distance distribution and the result of the fit are shown in Fig. 4.9. The noise hits under the main distribution, i.e. at earlier times, are due to primary or secondary particles (δ -rays) passing the straw at a closer distance to the wire, consequently producing an earlier signal. The noise hits above the main distribution, however, are mainly due to ionization clusters not being produced at the point on the track which is closest to the wire. In addition, when a particle does not produce any ionization cluster inside the straw, any other particle passing the same straw will produce a random signal. This effect is strongest close to the edges of the straw, where the path that the particle takes inside the straw is shortest.

Figure 4.10 shows the projections of the drift time and unbiased distance distributions with the overlaid fit projections. The unbiased distance distribution is expected to be flat, as the particles pass the straw at random distances. The observed dip at the distance $r = 0$ mm is due to the fit constraint $\Delta t < 6$ ns. This selection removes the hits that correspond to ionization clusters produced far away

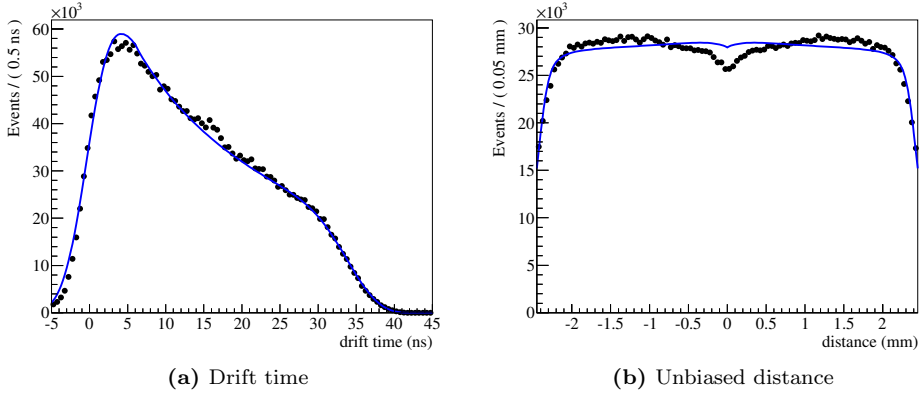


Figure 4.10: Drift time and unbiased distance distributions in data overlaid with the corresponding projections of the TR-relation PDF. The small dip in the PDF at $r = 0$ is due to the lower drift time limit ($-5 < t_{drift} < 45$ ns). The dip in the data is due to requirement $\Delta t < 6$ ns as explained in the text.

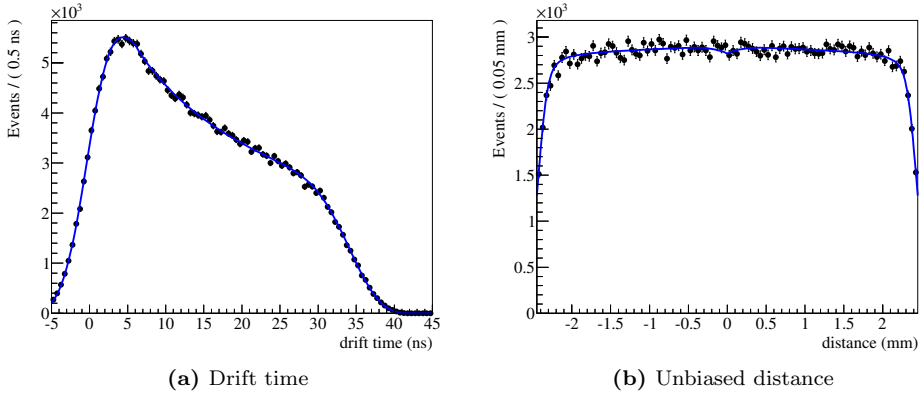


Figure 4.11: Drift time and unbiased distance distributions in MC overlaid with the corresponding projections of the TR-relation PDF. The small dip in PDF at $r = 0$ is due to lower limit on drift time ($0 < t_{drift}$).

from the point on the particle trajectory that is closest to the wire. This effect is strongest for particles passing the straw close to the wire, i.e. $r = 0$.

The TR-relation obtained from the fit describes the relation between the drift time and the distance from the track to the wire as it is seen from the reconstruction point of view. The parameterization is effective (empirical) and does not describe the underlying physics processes. For example, it can absorb residual effects from misalignment and/or asymmetry in the drift time residual distribution, in particular when the track passes the straw close to the wire.

The TR-relation PDF also allows to extract the effective ionization length, which is found to be $\lambda_{eff} = 0.8\text{mm}$. However, due to the cut $\Delta t < 6\text{ns}$ the resulting value is expected to be biased. In Section 4.5 an alternative method to extract the ionization length is described.

Finally, from the fit, the resolution dependence on the distance from the wire is extracted, which has the form $\sigma_t(r) = (2.6 + 0.9 \cdot |r|/r_m)\text{ns}$. This shows that the time resolution changes linearly from 2.6 ns close to the wire to 3.5 ns at the straw edge. From the physics point of view there is no obvious reason for the resolution to depend on the distance between the track and the wire. A possible source of this dependence will be discussed further in Section 4.6.

The TR-relation PDF describes all contributions that are implemented in the OT simulation. As a cross-check, the fit is performed on MC data and the result of the fit is shown in Fig. 4.11. The parameters of the fit, in particular the ionization length, TR-relation and resolution parameterization, agree with the ones used to simulate the data.

Comparisons between data and MC distributions for drift time and reconstructed distance are shown in Fig. 4.12. The normalization is chosen for the drift time on the right edge and for the distance on the plateau. The difference between data and MC in the drift time distribution is due to a different occupancy. In data the occupancy is about twice as high as in the MC, which leads to a relatively higher amount of earlier hits. For the reconstructed distance distribution the data-MC difference comes from the fact that in the data the mono-layers inside the modules are shifted with respect to their nominal position, such that there is an inefficiency at distance $|r| \sim r_m$, the inner edge of the straw. This effect will be discussed later in Section 4.6.

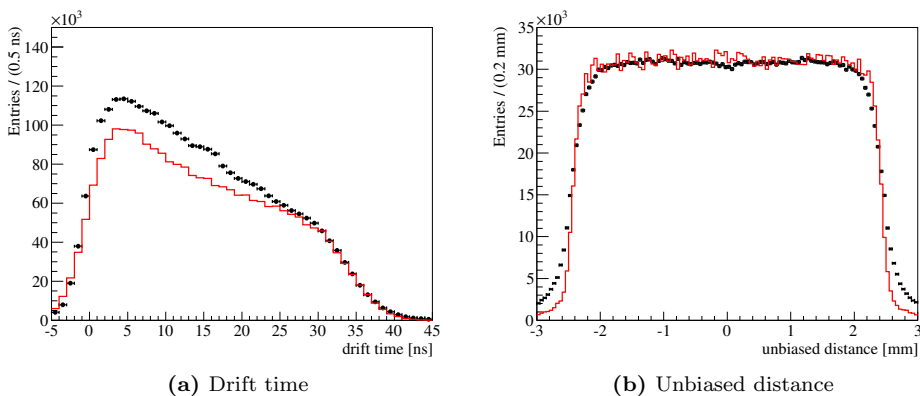


Figure 4.12: Comparison of drift time and unbiased distance for data (black points) and MC (solid line).

4.4 Walk correction

The read-out electronics measures the time when the signal passes the discriminator threshold. The variation in signal height leads to a variation of the measured TDC time. The scale of this variation can be estimated from the plot of the drift time residual versus the threshold value. Figure 4.13 shows how the t_0 value changes relative to the nominal setting. Close to the nominal threshold value of 800 mV, t_0 changes by approximately 0.5 ns per 100 mV.

After the signal is induced on the wire it propagates in both directions, toward the module front-end, and toward the straw end where it is reflected. Usually these signals do not interfere with each other and only the first one is used to measure the time. However, when the particle passes the straw close to the straw end at $y = 0$, the signal and its reflection sum up with some relative delay, effectively increasing the amplitude of the signal. The slope of the signal leading edge is proportional to the signal height. Therefore, larger signals pass the threshold earlier than smaller ones. This effect is called “walk” and is schematically illustrated in Fig. 4.14. In addition, the timing variation, due to a variation in amplitude of the signal, is smaller for larger signals. This means, that close to the straw end, where the signal is higher, the precision in the measured drift time is better than close to the read-out end. The effect of the walk can be parameterized as a function of distance from particle impact point to the straw end.

Figure 4.15 shows the average drift time residual versus the distance to the straw end. As expected, the hits are recorded earlier closer to the straw end where the walk effect is strongest. Note that a correction for the constant signal propagation speed along the wire has already been applied. Further away from the straw end, the drift time residual stabilizes, as the reflected signal is well separated in time from the original signal. The remaining slope towards the module front-end (the right hand side of the plot) is attributed to the attenuation of the signal along the wire.

To correct for this effect, a correction to the propagation time is applied depending on the distance to the straw end. This correction is assumed to be the same for all modules. The following parameterization for the walk is used:

$$walk(l) = b_{walk} + a_{walk} \cdot \left(\tanh \frac{l}{l_{walk}} - 1 \right) + v_{walk} \cdot l \quad (4.14)$$

where l is the distance from the hit to the straw end along the wire, a_{walk} is an amplitude of the walk effect, l_{walk} describes the effective length of the signal along the wire, v_{walk} describes the “walk” caused by the attenuation of the signal in the wire and b_{walk} is absorbed into definition of the t_0 .

The parameters of this dependence are extracted by fitting the distribution of the drift time residual versus the hit y position. The result of the fit is shown in Fig. 4.15. This correction changes the drift time for each hit of the track, and therefore the “walk” calibration is performed iteratively and simultaneously with the t_0 calibration, as it obviously changes the result of t_0 . The modified Eq. (4.3) has following form:

$$t_{TDC} = t_0 + t_{tof} + t_{drift} + t_{prop} + walk(l). \quad (4.15)$$

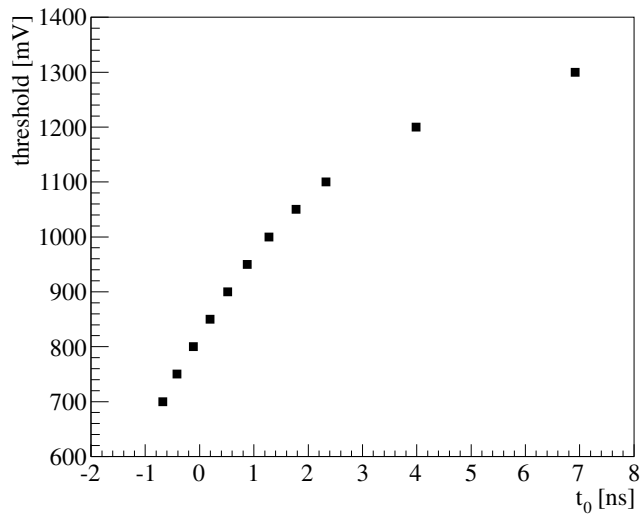


Figure 4.13: The value of t_0 versus the discriminator threshold. At 800 mV the slope is approximately 0.5 ns per 100 mV. The points are based on the calibration runs 69578-69611 of 2010 data taking.

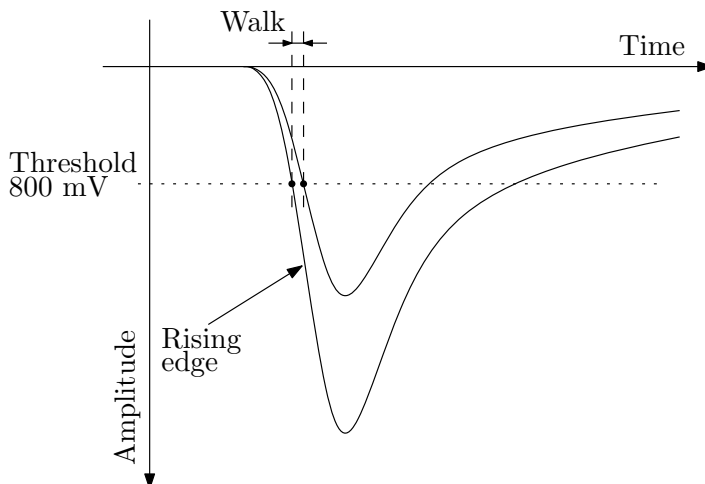


Figure 4.14: Illustration of walk. A higher signal passes the threshold earlier than a smaller signal.

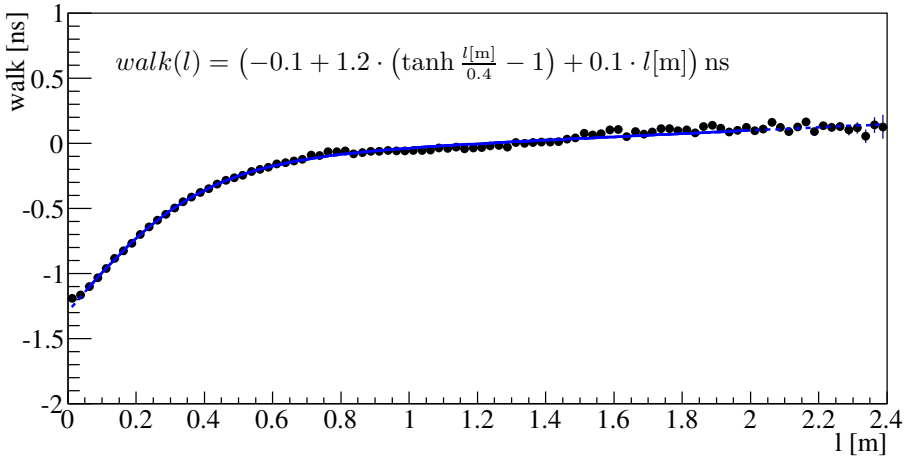


Figure 4.15: Average drift time residual versus the distance to the straw end along the wire. The line shows the walk parameterization fit.

The walk correction does not change the resolution significantly but improves the track reconstruction efficiency for tracks with a large vertical slope in the zy -plane. This is due to the fact that mainly the hits at large $|y|$ (small l) are affected by the walk correction, since the larger number of hits at small $|y|$ (due to tracks at small angles) dominate the t_0 calibration. The walk amplitude over the straw amounts to about 1 ns. Without the walk correction, this can lead to a small inefficiency in the pattern recognition, and hence an inefficiency in the track reconstruction.

4.5 The average OT time and spatial resolution

The time and spatial resolution of the OT are important performance parameters. The average resolution can be extracted from the drift time and distance residual distributions.

The resolution, as obtained from the fit to the unbiased distance residual distribution, is overestimated due to the finite precision of the track parameters and hence, by the precision of the reconstructed distance from the track to the wire at the position of the hit. This can be corrected by applying a scale factor α_r to every residual:

$$\alpha_r = \sqrt{\frac{\sigma_{meas}^2}{\sigma_{meas}^2 + \sigma_{track}^2}}, \quad (4.16)$$

where σ_{meas} and σ_{track} are the uncertainty on the measurement and track, respectively. The same scale factor can be used for both the drift time residual and the distance residual distributions.

The corrected distributions for the time residual and distance residual are shown

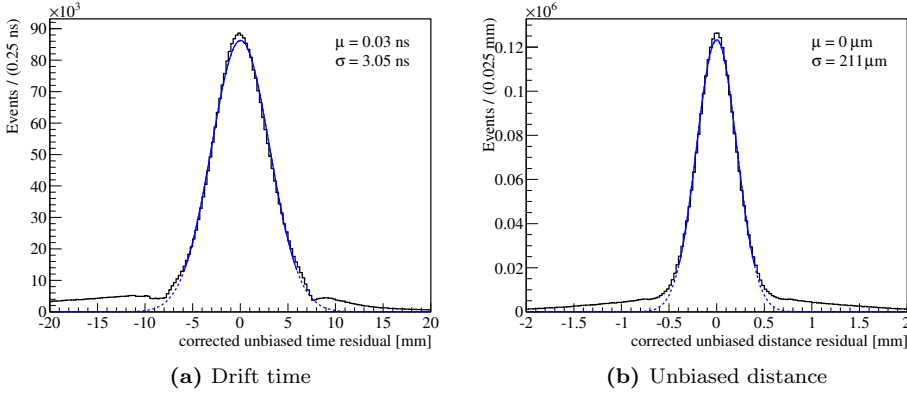


Figure 4.16: Drift time (a) and distance (b) residual distributions corrected for the finite track precision. The hit sample is for tracks with $p > 10$ GeV/ c and $\chi_{ub}^2/N_{Dof} < 2$. Lines show the Gaussian fits to the distributions in the range $\pm 2\sigma$, dotted lines show the continuation to the full range. Parameters μ and σ are the mean and sigma of the Gaussian fits.

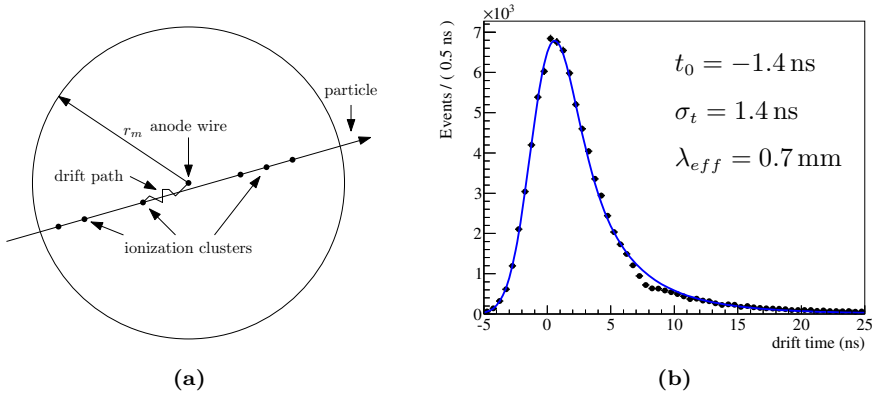


Figure 4.17: (a) - illustration of a particle passing the straw close to the wire, the distance to the closest ionization cluster is large; (b) - drift time distribution for the hits with the distance from the track to the wire $|r| < 0.1$ mm. From this distribution the effective ionization length can be determined and amounts to $\lambda_{eff} = 0.7$ mm.

in Fig. 4.16. The average drift time resolution is 3 ns and the corresponding spatial resolution is 211 μm .

As can be seen, noise is present on both sides of the distance distribution, and a long tail on the left side of the drift time residual distribution. This noise comes mainly from secondary hits, that are recorded at earlier times and mask the real ones. On the right side of the drift time residual distribution there is a small excess which comes from the fact that ionization clusters are produced not at the closest point between the track and the wire, and the measured time is higher (for the distance residual these two effects are averaged on the left and right hand side). This effect is strongest when the particle passes the straw close to the wire. Figure 4.17 illustrates such an event and shows the drift time distribution for tracks with a reconstructed distance to the wire $|r|$ smaller than 0.1 mm.

Assuming that the particle passes the straw at distance $r = 0$, the simplified drift time PDF that takes into account the distribution of ionization clusters along the particle trajectory can be constructed:

$$f(t_{\text{drift}}) = \int_0^{r_m} G_t(t_{\text{drift}} | t_0 + t(l), \sigma_t) \exp\left(-\frac{2}{\lambda_{\text{eff}}} \cdot l\right) dl, \quad (4.17)$$

where the exponent defines the probability to find an ionization cluster at distance l from the wire, the Gaussian describes the drift time resolution effect. The parameters of the TR-relation $t(l)$ in the PDF are fixed to the values obtained in the standard fit, but the offset t_0 is necessary as the meaning of the TR-relation here is different. A fit with such a PDF to the drift time distribution, shown in Fig. 4.17 (b), gives for the ionization length $\lambda_{\text{eff}} = 0.7 \text{ mm}$. This value is very close to the one obtained in the standard fit ($\lambda_{\text{eff}} = 0.8 \text{ mm}$).

Momentum dependence

The hit resolution shows a dependency on the momentum of the track (Fig. 4.18). The explanation for this effect partly comes from the fact that low momentum tracks are bent more in the magnetic field and hits are distributed over the full width of the OT. For low momentum tracks the hit resolution is thus dominated by the contribution from long modules. For high momentum tracks, however, the main contribution to the resolution comes from the central short modules. As will be explained in Section 4.6 the resolution is different for short and long modules. In addition, the resolution also depends on the y -position of the hit due to the walk, as was explained in Section 4.4.

Figure 4.18 (a) shows the hit resolution dependence on the momentum of the track. From 3.2 GeV/ c to 50 GeV/ c the resolution changes from 280 μm to 210 μm . Consequently the width of the pull distribution is not flat. This dependence is partly due to the different hit resolution in the short and long modules (see Section 4.6). Introducing separate resolution parameterizations for long and short modules (Eq. (4.23) and Eq. (4.24)) allows to reduce this effect. Figure 4.18 (b) shows the pull width dependence on the momentum, where for each hit the resolution parameterization of corresponding module (short or long) is used. Consequently, the relative change in pull width is smaller than the corresponding change

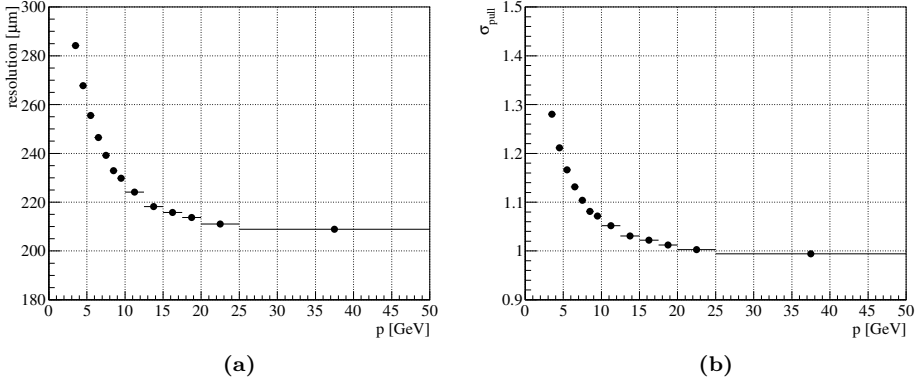


Figure 4.18: The dependence of the hit resolution (a), and the width of the pull distribution (b) on the momentum. The hit resolution is corrected for multiple scattering using the α_r factor of Eq. (4.16). The pull value is calculated using different resolution parameterizations for short and long modules.

in hit resolution. The remaining effect comes from the dependence of the resolution on the distance from the hit to the readout end, as the signal is higher at the straw end, the resolution is better. Currently this effect is not implemented in the track reconstruction.

4.6 Mono-layer shift

A misalignment of the detector contributes to the overall OT resolution. Currently the alignment of the OT is performed on the level of modules. Aligning individual straws within modules is not envisaged in the current implementation of the detector geometry. The choice of this granularity was driven by the fact that the structure of a module was assumed to be well fixed during production.

Each module consists of two mono-layers (shown in Fig. 4.19) which can be shifted with respect to each other. This shift is the same for all straws inside one mono-layer, but in opposite directions in mono-layer one and two. If a mono-layer has a shift $\Delta x > 0$ relative to the nominal position, the measured drift time for a particle passing the straw from the left side of the wire ($x < x_{\text{wire}}$) or right side of the wire ($x > x_{\text{wire}}$) will be higher or lower than nominal one, respectively. The reconstructed distance from the track to the wire does not correct for this, as the used geometry in the reconstruction software is the same. Figure 4.20 illustrates this effects.

Consequently, due to the mono-layer shift the drift time residual distributions have approximately the same shift in opposite directions for particles passing the straws from left or right sides of the wires. In addition, as the mono-layers are shifted in opposite directions, the corresponding shifts are also in opposite direc-

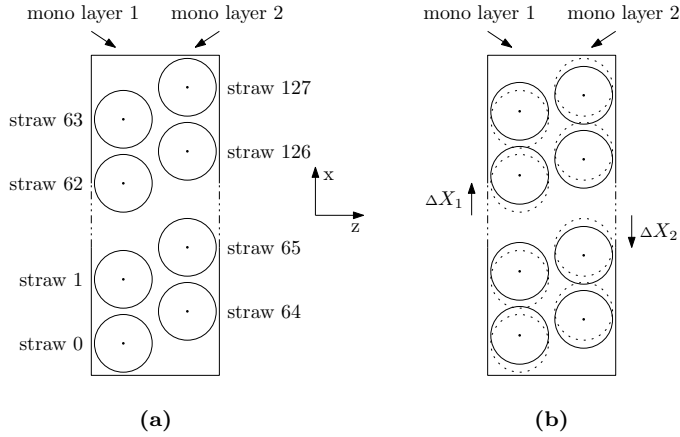


Figure 4.19: Structure of the module, showing the numbering and position of a mono-layers (a), and illustration of mono-layer misalignment (b). On the right plot the solid lines show the “true” position of the straws, and the dotted lines illustrate the nominal position of the straws as used by reconstruction software.

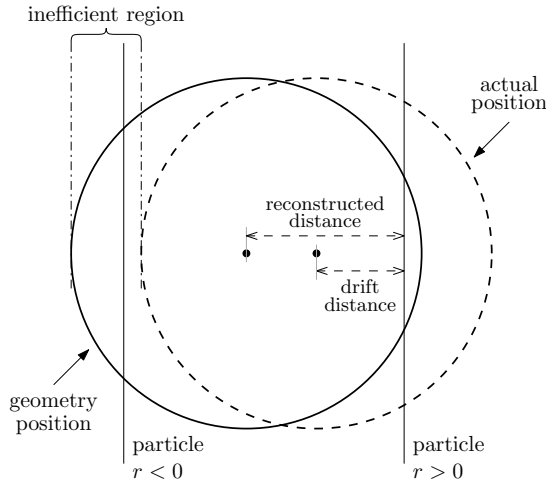


Figure 4.20: Illustration of the straw misalignment effect. The dashed line shows the actual position of the straw that is shifted to the right relative to the position of the straw as used in the reconstruction software (solid line). For track passing the straw from the right side ($r > 0$) of the wire the reconstructed distance r_{rec} is bigger than the drift distance r_{drift} . Consequently the drift time estimated from the TR-relation $t(r_{rec})$ is bigger than measured drift time.

tions for mono-layers 1 and 2. Figure 4.21 shows the drift time residual distributions for one module that illustrates the double Gaussian structure that is the result of the mono-layer shift. By decomposing contributions for left and right tracks in each mono-layer, the Gaussian structure of both contributions becomes apparent and the distributions are shifted in opposite directions in time.

In addition, the mono-layer shifts are not constant and can depend on the y -position. Figure 4.22 shows for one module the average distance residual in slices of the y -position for different groups of straws. The wires are fixed at the module ends (same offset) and the deviation becomes larger towards the center of the module. The discontinuities at ± 80 cm and ± 160 cm correspond to the positions of wire locators in the straws. The average mono-layer shifts also depend on the length of the module. Shorter modules exhibit an average shift that is smaller than that of long modules.

The knowledge of the mono-layer shifts leads to a small modification of the t_0 calibration procedure. The t_0 value for each module front-end is calculated by fitting the drift time residual distributions with a Gaussian function. Due to the mono-layer shift the time residual distribution has a double Gaussian structure and the fit becomes less robust and precise. This is especially important for modules that have significant shifts. A more robust way is, therefore, to extract t_0 separately for each mono-layer and for tracks passing the straw from the left or right side, as shown in Fig. 4.21. The final value for t_0 is the average over these four values. This method also allows to reduce the effect of inefficiency in the pattern recognition that arises at the straw edges due to a shift of the mono-layer and imperfect alignment. This inefficiency is the source of the difference in height of the distributions for tracks passing from the left or right side shown in Fig. 4.21.

The effect of the mono-layer shift on the resolution can be studied by performing a “local” alignment on the level of half mono-layers of 32 straws. This is done by applying the correction to the distance from the track to the wire that corresponds to the shift of the half mono-layer. The shift is approximately equal to the average distance residual of all hits corresponding to this mono-layer. By applying this correction to all hits one can construct the corrected TR-relation distribution, shown in Fig. 4.23, and extract the resolution.

The TR distribution after alignment shows a considerably narrower band. By performing the TR-relation fit to the aligned distribution the extracted parameterization of the TR-relation remains unchanged, but the resolution dependence becomes flat and does no longer depend on the distance to the wire. This shows that the main contribution to the observed dependence of the resolution on the distance from the wire to the track comes from the mono-layer shift. Figure 4.24 shows the distribution of drift time and unbiased distance corrected for α_r before and after “local” alignment. The resolution obtained from a fit to this distributions is 2.6 ns and 179 μ m, which is about 20% better than before the alignment. Currently the mono-layer alignment is not implemented in the reconstruction since the smallest geometry unit being defined is the module, and an implementation of a mono-layer geometry would be required to perform the alignment at this level.

The distribution of the shifts for all modules in the OT has a Gaussian structure with a width of about 150 μ m, but it is different for long and short modules. This

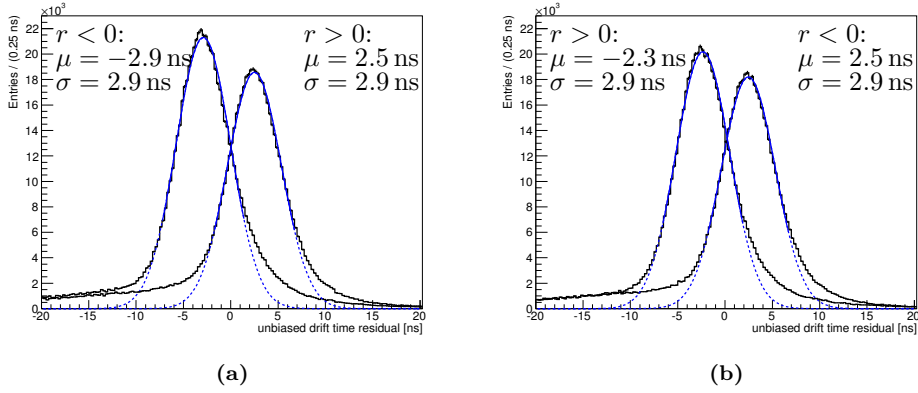


Figure 4.21: Drift time residual distribution for first (a) and second (b) mono-layers, and for tracks traversing the straw from the left ($r < 0$) and right ($r > 0$) sides.

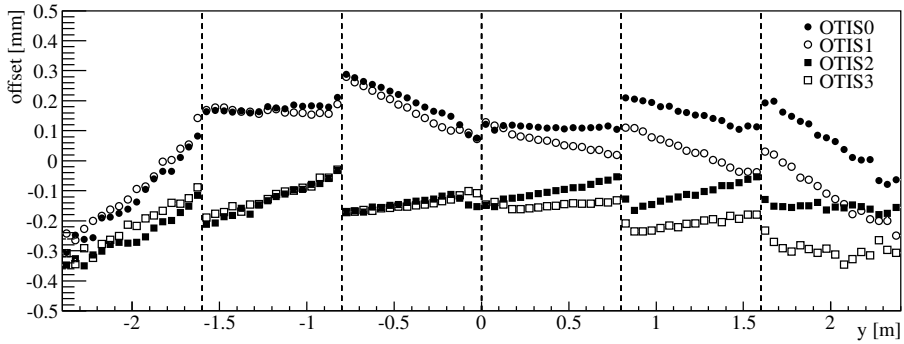


Figure 4.22: Detailed structure of the mono-layer misalignment for one detector module (T3L3Q1M7). Each point corresponds to the average drift time residual in a slice of y . Circles and squares correspond to the first and second mono-layer, respectively. Filled and open points correspond to channels 0-31 and 32-63, respectively.

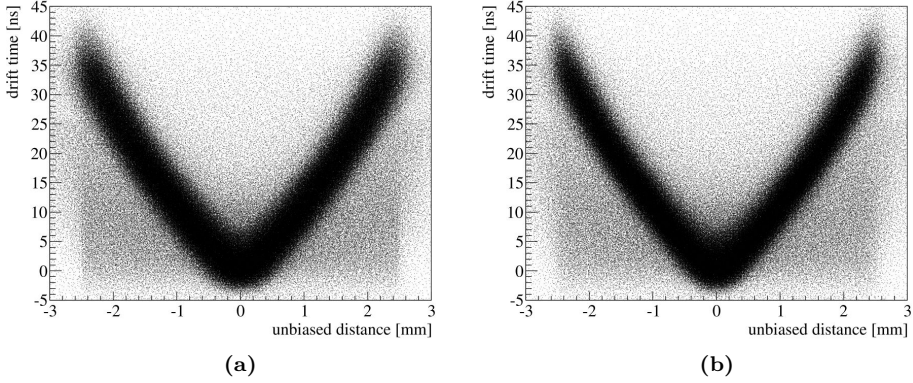


Figure 4.23: Drift time to distance distribution before (a) and after (b) “local” half mono-layer alignment. Plot (b) has a narrower band than plot (a).

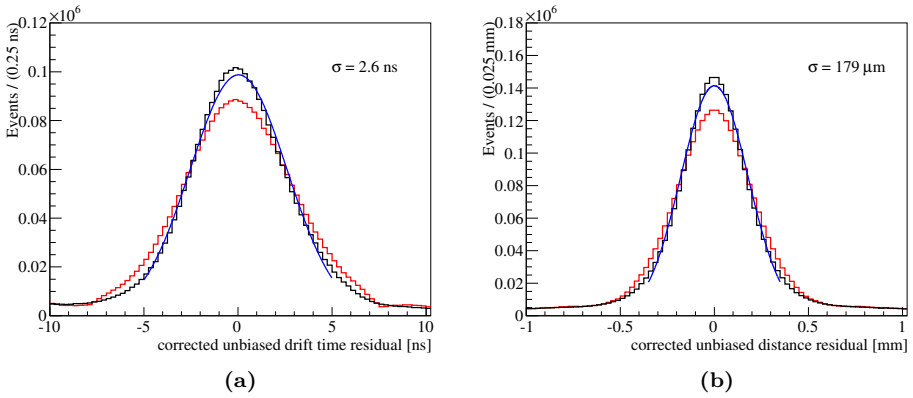


Figure 4.24: Drift time (a) and distance (b) unbiased residual distributions corrected for α_r , for tracks with a momentum $p > 10$ GeV/ c and $\chi^2_{ub}/N_{DoF} < 2$, before (red histograms) and after (black histograms) “local” alignment. Lines show the Gaussian fit to the aligned distributions.

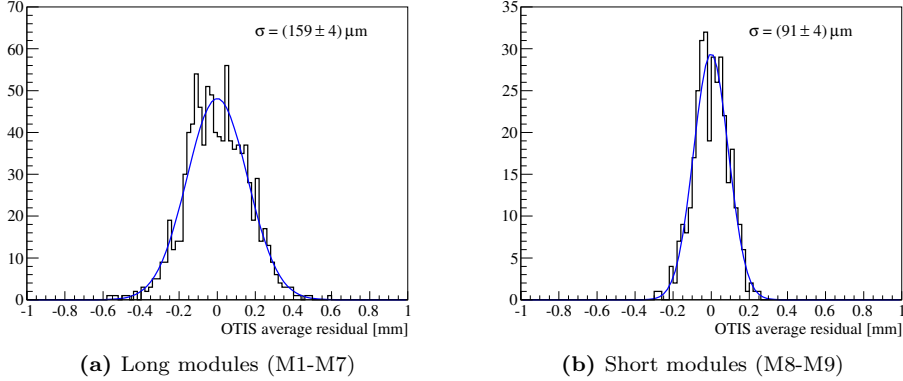


Figure 4.25: Distribution of OTIS average residual for modules M1-M7 (a) and M8-M9 (b).

leads to a different resolution for these groups of modules. As shown in Fig. 4.25 the width for long modules is $159 \mu\text{m}$ and for short ones is $91 \mu\text{m}$. Performing the TR-relation fit separately for long and short modules gives a resolution of $\sigma_t = (2.7 + 1.0 \cdot r/r_m)$ ns and $\sigma_t = (2.6 + 0.6 \cdot r/r_m)$ ns for long and short modules, respectively.

The consistency of these numbers can be shown as follows. The “true” resolution is obtained from the fit to the “aligned” detector, see Fig. 4.23 (b), and amounts to 2.4 ns. By calculating the contribution from misalignment using the TR-relation and employing error propagation, one can extract the final resolution for the “unaligned” detector, corresponding to Fig. 4.23 (a). The TR-relation is given by:

$$t(r) = \left(21.1 \frac{r}{r_m} + 14.4 \frac{r^2}{r_m^2} \right) \text{ ns}, \quad (4.18)$$

and the conversion of time to space resolution is given by:

$$\delta_t = \partial_r t(r) \cdot \delta_r, \quad (4.19)$$

where

$$\partial_r t(r) = \frac{dt(r)}{dr} = \left(8.6 + 11.8 \frac{r}{r_m} \right) \text{ ns/mm}. \quad (4.20)$$

For short modules the misalignment of $91 \mu\text{m}$ translates into a contribution to the time resolution of $\partial_r t(r=0) \cdot 0.091 \approx 0.8$ ns and $\partial_r t(r=r_m) \cdot 0.091 \approx 1.9$ ns; for long modules the misalignment of $159 \mu\text{m}$ translates into $\partial_r t(r=0) \cdot 0.159 \approx 1.4$ ns and $\partial_r t(r=r_m) \cdot 0.159 \approx 3.2$ ns. Adding these contributions to the “true” time resolution in quadrature gives:

$$\sigma_t^{(S)} = \sqrt{2.4^2 + 0.8^2} \left(1 - \frac{r}{r_m} \right) + \sqrt{2.4^2 + 1.9^2} \frac{r}{r_m} = \left(2.5 + 0.6 \frac{r}{r_m} \right) \text{ ns} \quad (4.21)$$

and

$$\sigma_t^{(L)} = \sqrt{2.4^2 + 1.4^2} \left(1 - \frac{r}{r_m}\right) + \sqrt{2.4^2 + 3.2^2} \frac{r}{r_m} = \left(2.8 + 1.2 \frac{r}{r_m}\right) \text{ ns}, \quad (4.22)$$

where the $\sigma_t^{(S,L)}$ are the resolution for short (long) modules.

Comparison of these values with the values obtained from a fit, for short and long modules separately, gives

$$\sigma_t^{(S)} = \left(2.6 + 0.6 \frac{r}{r_m}\right) \text{ ns} \quad (4.23)$$

and

$$\sigma_t^{(L)} = \left(2.7 + 1.0 \frac{r}{r_m}\right) \text{ ns}, \quad (4.24)$$

and shows that they are equal within 0.3 ns. The difference might be due to the use of a linear parameterization for the resolution dependence.

4.7 Results

Full fit including all calibrations

The full calibration procedure consists of t_0 calibration, TR-relation and resolution fit, and walk correction. It is essential that all these calibrations are performed at the same time, as a change in any of them can influence parameters of the others. Figure 4.26 shows the flow chart of the calibration procedure.

Each iteration consists of the full reconstruction of the events, following by the t_0 , walk and TR-relation calibrations, and finally the update of the condition database. This procedure is repeated until the changes in the parameters do not exceed 10% of the average drift time resolution, which is 0.3 ns.

Table 4.1 shows the parameters for TR-relation, resolution and walk for different runs of 2011 that correspond to the beginning of the data taking periods after technical stops.

Comparing the values of different parameters, the variation around their average is summarized below:

- $\Delta t_m < 0.3 \text{ ns}$
- $\Delta t_c < 0.1 \text{ ns}$
- $\Delta \sigma_t(r = 0) < 0.1 \text{ ns}$
- $\Delta \sigma_t(r = r_m) < 0.1 \text{ ns}$
- $\Delta a_{walk} < 0.1 \text{ ns}$ (see Eq. (4.14))
- $\Delta l_{walk} < 1 \text{ cm} \approx \sigma_y$ - hit resolution along y -axis
- $\Delta v_{walk} < 0.03 \text{ ns/m} \approx 0.1 \text{ ns}$ over the straw length

In the final calibration the values of all parameters, except for the t_0 values, were chosen to be the same, as the TR-relation and walk correction do not depend on the run period.

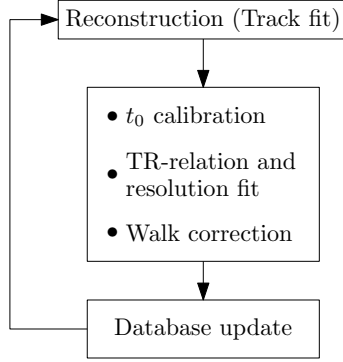


Figure 4.26: Flow chart of calibration procedure.

	Run					
	87891 2011-03-23 Fill 1645	89350 2011-04-15 Fill 1711	91933 2011-05-20 Fill 1795	96641 2011-07-21 Fill 1962	101414 2011-09-08 Fill 2086	104034 2011-10-24 Fill 2242
t_m [ns]	35.6	35.4	35.3	35.3	35.3	35.1
t_c [ns]	3.5	3.6	3.5	3.4	3.4	3.4
$\sigma_t(r=0)$ [ns]	2.5	2.6	2.6	2.6	2.6	2.7
$\sigma_t(r=r_m)$ [ns]	3.2	3.2	3.2	3.2	3.2	3.4
a_{walk} [ns]	1.22	1.12	1.15	1.14	1.16	1.14
l_{walk} [m]	0.40	0.39	0.39	0.39	0.40	0.40
v_{walk} [ns/m]	0.09	0.15	0.12	0.12	0.11	0.11

Table 4.1: Summary table of different calibration parameters for different runs. Each run corresponds to the start of a different data taking period of 2011.

t_0 stability

It is important to know the stability during data taking of the t_0 values and the parameters that describe the walk correction and TR-relation. There are two factors that can influence the t_0 stability: one is a drift of the LHC clock, the other is the drift of the electronic read-out delays. The first one can be estimated from the average of the drift time residual distributions calculated separately for every run over a period of time. The second one can be estimated from the difference in t_0 values for two calibrations of runs from different data taking periods.

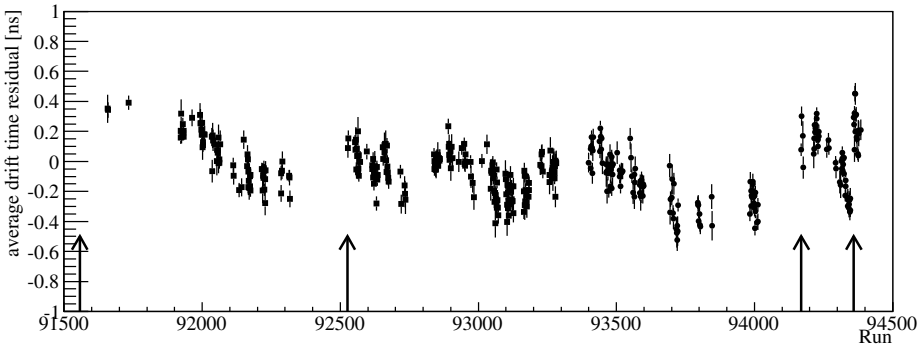


Figure 4.27: The stability of timing versus the run number. Every point is an average of drift time residual distribution for all hits in the run. Squares and circles correspond to runs taken with magnet down and magnet up polarities, respectively. Arrows indicate the points where the LHC clock was adjusted.

Figure 4.27 shows the variation of the LHC clock time versus the run number for the data taking period from May to July of 2011. Each point corresponds to one run (up to one hour of data taking). Squares (circles) correspond to runs taken with magnet down (up) polarity. Arrows show when the clock t_{clock} was adjusted. As can be seen the average drift time residual is stable within the range of ± 0.5 ns, which is well below the time resolution of 3 ns, and does not contribute significantly to the resolution.

Figure 4.28 (a) shows the difference in the values of t_0 between runs 87891 and 89350. These runs correspond to the beginning of two data taking periods in May and July. Most module front-ends have differences in the values of t_0 grouped in a narrow band with a width smaller than 0.1 ns. The absolute shift of about 0.2 ns can be attributed to the drift of the t_{clock} value.

Even though the stability is adequate there have been cases where the module t_0 changed significantly. One such change was observed in the beginning of May 2011 due to the adjustment of Δt_{clock}^{FE} . Figure 4.28 (b) shows the difference in the values of t_0 between runs 87891 and 89350. The shift of -4 ns and -2 ns are due to the adjustment of Δt_{clock}^{FE} from 28 ns to 32 ns and 30 ns in T3 and T2, respectively. The Δt_{clock}^{FE} for T1 did not change, however, due to the cleaning of the fiber that carries the clock signal to one control box, the offset of +1 ns was observed for 18

module front-ends in T1.

The t_0 calibration is performed at the level of modules. This granularity was chosen because the variations of the t_0 values from straw to straw for a particular module are small. Figure 4.29 (a) shows the t_0 value versus straw number for module T0L0Q0M8. As can be seen the t_0 values vary from straw to straw, but the variations are below ± 0.5 ns within the groups of 32 straws, which correspond to one OTIS chip. Figure 4.29 (b) shows the distribution of t_0 values, calculated for 16 straws, for the whole OT. The distribution has a sigma of 0.4 ns which is much smaller than the resolution of the detector.

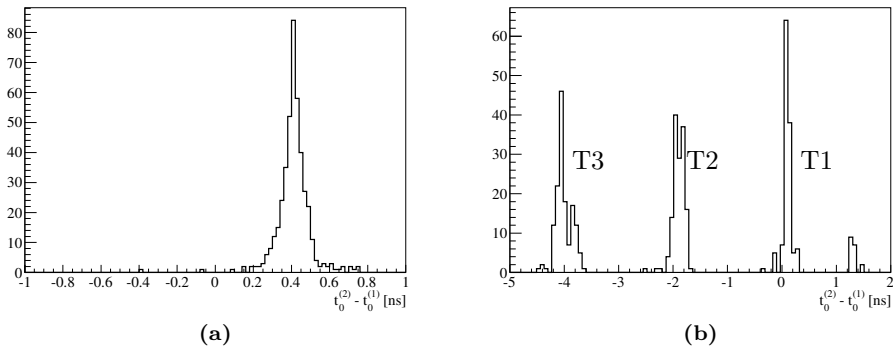


Figure 4.28: Difference in the values of t_0 between runs 87891 and 89350 (a), and between runs 89350 and 91933 (b). Each entry corresponds to one module front-end.

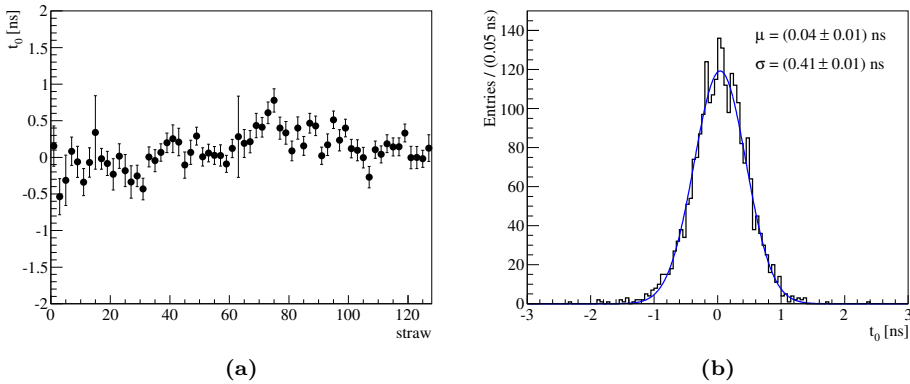


Figure 4.29: (a) The value of t_0 as a function of the straw number in module T0L0Q0M8, averaged over four adjacent straws. (b) The distribution of t_0 values, averaged over groups of 16 consecutive straws, for the whole OT.

Future development and prospects

The current calibration is robust and is currently used as the main algorithm for the OT time calibration in LHCb. There is still room for improvement. For example the alignment of half mono-layers could improve the resolution by 10 to 20%. In addition, there are specific tunes that can be implemented in the pattern recognition and track reconstruction algorithms that would take into account the structure of the time residual distribution and improve the hit on track efficiency. Also, the remaining effect of the hit resolution dependence on the momentum can be corrected for by introducing a resolution dependence on the distance to the straw end, in addition to the resolution parameterization per module.

As for the stability, it is possible to implement an additional extension to the calibration database, for example, the global t_0 offset that describes the synchronization between t_{clock} and $t_{collision}$. Furthermore, it is possible to implement a t_0 calibration per individual OTIS chip, as it was shown that t_0 values can vary from straw to straw by about 0.5 ns.

In the simulation a more detailed digitization procedure can also be implemented, for example a correct simulation of the distribution of ionization clusters along the particle trajectory. This correction could improve the description of the drift time spectra at small distances to the wire, but will require the implementation of a complicated calibration procedure.

The currently achieved average time resolution is about 3 ns. With the implementation of half mono-layer alignment in groups of 32 straws the resolution can be improved to approximately 2.4 ns. This corresponds to an improvement in the average spatial resolution from 210 μm to 180 μm , which is similar to what was measured in the OT beam test of 2005 [46].

Chapter 5

D^0 and D^{*+} production cross section

The measurement of hadron production in proton-proton collisions allows to test predictions of quantum chromodynamics (QCD). In addition, knowledge of the charm production cross section is particularly important for estimates of the sensitivity of LHCb for measurements of CP violation, mixing and rare decays in the charm system.

In this chapter the measurement of the production cross section of D^0 and D^{*+} mesons is described.¹ The measurement was performed using 15 nb^{-1} of proton-proton collision data collected with the LHCb detector at 7 TeV center-of-mass energy in May 2010.

In pp collisions charmed mesons are produced either directly, or through the immediate decay of excited charm resonances, or in the decay of B mesons. The first two are referred to as prompt production and the latter is called secondary production. The present work measures the production cross section of prompt charm mesons.

The analysis is performed on fully reconstructed decays of D^0 and D^{*+} mesons in the decay modes:

- $D^0 \rightarrow K^-\pi^+$ and
- $D^{*+} \rightarrow D^0\pi^+$ where $D^0 \rightarrow K^-\pi^+$.

The cross section was measured in 8 equal size bins of transverse momentum p_T in the range $0 < p_T < 8\text{ GeV}/c$ and 5 equal size bins of rapidity y in the range $2.0 < y < 4.5$.

Section 5.1 summarizes the data sample used for the analysis and the conditions under which the data were taken. Section 5.2 describes the selections that were applied to the reconstructed D^0 and D^{*+} candidates. Section 5.3 presents the yield extraction procedure. Section 5.4 discusses the selection efficiency, including particle identification (PID), and describes the Monte Carlo (MC) samples used

¹In this chapter the charge conjugate modes are implied, unless stated otherwise.

for the efficiency calculation. Section 5.5 lists the sources and magnitudes of the systematic uncertainties. The final results for the measured cross sections and their ratio, and a comparison with theoretical predictions are given in Section 5.6. In Section 5.7 the measurement of the polarization of the D^{*+} meson as a function of p_T is described. Finally, in Section 5.8 a summary of the cross section measurement is given and possible improvements are discussed.

5.1 Data set

The measurement of the charm production cross section is based on 15 nb^{-1} of proton-proton collision data collected with the LHCb detector at 7 TeV center-of-mass energy in May 2010.

These data were taken under low pile-up conditions, where most events contained only one reconstructed primary vertex. The cross section measurement is performed on a subset of the events that have passed the micro-bias trigger. This trigger is implemented in the High Level Trigger (HLT) and requires the presence of at least one reconstructed track in the VELO or T stations. As determined from MC, the micro-bias trigger has 100% efficiency for the events that contain a D^0 or D^{*+} meson in the LHCb acceptance. Therefore, the efficiency is independent of the decay mode and kinematics of the charm meson, allowing the measurement of the cross section in low p_T region.

During the data taking two trigger configurations were used, further denoted as data samples I and II. These trigger configurations were designed for low pile-up data of 2010. The total integrated luminosity corresponding to these data samples are provided by the Luminosity Working Group [52]:

- $L_I = 1.87 \pm 0.07 \text{ nb}^{-1}$,
- $L_{II} = 13.09 \pm 0.46 \text{ nb}^{-1}$.

In data sample I all events that have passed the micro-bias trigger were kept, such that the efficiency $\varepsilon_I^{mb} = 1$. In data sample II, however, to reduce the rate, only part of the micro-bias triggered events were kept. The bulk of the events pass the “rate limited” trigger line, that limits the rate to 100 Hz. The luminosity corresponding to the micro-bias triggered events for data sample II was determined using an unbiased “scaled” trigger line, that reduces the rate by a constant fraction 100. The combined efficiency of scaled and limited lines is $\varepsilon_{II}^{mb} = 0.2399 \pm 0.0019$. The total effective integrated luminosity that corresponds to micro-bias triggered data is:

$$L^{mb} = \sum_{i=I,II} \varepsilon_i^{mb} L_i = (5.01 \pm 0.18) \text{ nb}^{-1}, \quad (5.1)$$

where index “ mb ” denotes the micro-bias.

Signal MC

A full event and detector simulation is used for signal studies, and to estimate the generator and reconstruction efficiency. The event samples were generated with

the LHCb tune of PYTHIA [53], followed by a full GEANT event simulation and LHCb reconstruction.

During the event simulation the products of D^0 and D^{*+} decays are required to have their momentum pointing into the angular acceptance of LHCb. This requirement is referred to as the generator cut. Only events that have passed this requirement were saved and subsequently reconstructed.

In total $3 \cdot 10^6$ events for each signal mode (D^0 decaying to $K^-\pi^+$, and D^{*+} decaying to $D^0\pi^+$ where $D^0 \rightarrow K^-\pi^+$) and for each magnet polarity were simulated and stored for subsequent analysis. The simulation was performed with an average number of interactions per bunch crossing $\nu = 1$, however, to simulate the low instantaneous luminosity environment of the data only events with one interaction were used to estimate the reconstruction efficiencies.

The procedure to estimate the generator and reconstruction efficiency are described in detail in Section 5.4.

5.2 Event selection

The analysis is based on fully reconstructed decays of D^0 and D^{*+} mesons. The D^0 candidates are reconstructed in the final state $K^-\pi^+$, and D^{*+} candidates are reconstructed in the final state $D^0\pi^+$ where $D^0 \rightarrow K^-\pi^+$. The events used for the analysis are required to pass the micro-bias trigger and have at least one reconstructed primary vertex.

D^0 selection

The D^0 candidates are reconstructed from two oppositely charged long tracks, where one track has the kaon mass assigned and the other track has the pion mass assigned. Both tracks are required to have a track fit $\chi^2_{tr} \equiv \chi^2/N_{DoF} < 5$, and the minimum Kullback-Leibler [54] (KL) distance $d_{KL} > 5000$ with respect to all other tracks.² These requirements allow to reduce the contribution of “fake” ghost and clone tracks that can be produced by the pattern recognition software.

To suppress random combinations and backgrounds from reflections the particle identification (PID) information is used. The kaon and pion tracks are required to have the ratio of kaon to pion likelihoods ($\log(\mathcal{L}_K/\mathcal{L}_\pi)$) larger and smaller than zero, respectively. The likelihood values are mainly based on the information provided by the RICH detectors and are assigned to each track by the LHCb PID algorithms. The PID efficiency is determined from a calibration data sample for each track type and subsequently used for the determination of the total PID efficiency of the D^0 and D^{*+} in (p_T, y) bins. Consequently, the phase space of the kaon and pion tracks, for which the PID efficiency cannot be determined, is vetoed. The kaon and pion tracks are required to have momentum $3.2 < p < 100$ GeV/c, pseudo-rapidity $2 < \eta < 5$ and transverse momentum $p_T < 5$ GeV/c. Additional criteria are applied to the kaon and pion tracks due to the limited size of the calibration data sample and are discussed in Section 5.4.

²The KL distance measures the difference between PDFs that describe track parameters. If the distance is small then two tracks are likely to be clones.

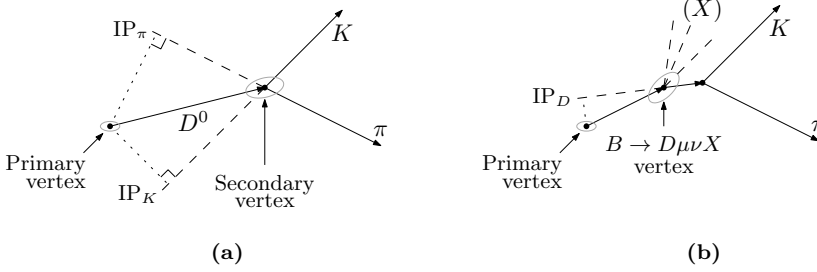


Figure 5.1: (a) Illustration of D^0 decaying to kaon (K) and pion (π) at a secondary vertex, and their impact parameters (IP_K and IP_π) with respect to the primary vertex. (b) Illustration of $B \rightarrow D^0 \mu \nu X$ decay, where the D^0 produced in the B decay does not point to the primary vertex.

The D^0 candidates are required to have a reconstructed mass in a wide mass window $1790 < m_{K\pi} < 1940 \text{ MeV}/c^2$ to allow signal and background determination.

The following selection criteria are used to further reduce background based on the properties of the D^0 decay:

- A lower limit on the impact parameter (IP) significance $\chi_{IP}^2 \sim IP/\sigma_{IP}$ of the kaon and pion produced in the D^0 decay with respect to the reconstructed primary vertex. This requirement suppresses the background containing tracks that originate from the primary vertex, as the final state particles produced in the D^0 decay do not generally point to the primary vertex (see Fig. 5.1).
- An upper limit on the D^0 vertex fit $\chi_{vtx}^2 \equiv \chi^2/N_{Dof}$. This requirement ensures that kaon and pion tracks have a common origin (the secondary vertex).
- A lower limit on the D^0 proper time ($c\tau$). This requirement suppresses background from particles produced at the primary vertex, as the D^0 has a lifetime $c\tau = 123 \mu\text{m}$ and its decay vertex is displaced from the primary vertex, whereas the background peaks at zero.
- A cut on the angle between the pion momentum direction and the D^0 momentum direction in the D^0 rest frame (θ_π). The D^0 is a scalar meson, consequently, the pion has an isotropic angular distribution in the D^0 rest frame, whereas background peaks at $\theta_\pi \sim 0^\circ$. The cut is applied to the function $\cos(\theta_\pi)$.

These selections are optimized for minimal yield uncertainty, as it directly translates into the cross-section uncertainty. The optimization procedure and the final selection values are discussed later in this section.

In addition to the above variables, the χ_{IP}^2 of the D^0 with respect to primary vertex is used to separate the prompt and secondary D^0 mesons. For promptly produced D^0 the χ_{IP}^2 should be small, while for secondary production the χ_{IP}^2

should be large. For example, in the $B \rightarrow D\mu\nu X$ decay, where X can be anything, the B meson decays further from the primary vertex and the D^0 produced in the B decay does not point back to the primary vertex. Figure 5.1 shows an illustration of the D^0 decay produced promptly (a) and in the decay of the B meson (b). In this analysis the prompt and secondary components are separated by performing simultaneous fits to mass variables and $\log_{10}(\chi_{IP}^2)$ of the reconstructed D^0 .

Due to the high rate, only those events that have passed the pre-selection criteria are written to disk and are available for the analysis. In particular, due to high background at large $D^0 \chi_{IP}^2$, the cut $\chi_{IP}^2 < 100$ is applied, consequently limiting the prompt/secondary separation capability. This effect will be discussed further in Section 5.3.

D^{*+} selection

The D^{*+} candidates are reconstructed from D^0 candidates by combining them with a charged long track, to which the pion mass is assigned.

The pion track is required to have the track fit $\chi_{tr}^2 < 5$. To ensure that pion and D^0 are produced from the same vertex, the D^{*+} vertex fit is required to have $\chi_{vtx}^2 < 16$. To separate the signal and background the difference between the reconstructed masses of the D^{*+} ($m_{K\pi\pi}$) and D^0 ($m_{K\pi}$) is used, $\Delta m = m_{K\pi\pi} - m_{K\pi}$. To limit the event rate the Δm is required to be less than $155 \text{ MeV}/c^2$.

Note that there is no requirement on KL distance or the PID of the pion. Due to the low momentum of the pion the PID requirement did not show any significant improvement in the signal to background ratio, while KL distance was considered not reliable at this momentum scale.

Optimization procedure

The selections for four variables (kaon/pion χ_{IP}^2 , $D^0 \chi_{vtx}^2$, D^0 proper time $c\tau$, and $\cos(\theta_\pi)$ in the D^0 rest frame) are optimized, such that the total yield in the kinematic range of $0 < p_T < 8 \text{ GeV}/c$ and $2.0 < y < 4.5$ is determined with the best possible precision.

The optimization is performed by studying the value of the relative yield uncertainty σ_s/s versus the applied cut value, where s is the D^0 yield, and σ_s is the statistical uncertainty on the yield given by the fit with a Gaussian and linear background to the D^0 mass distribution. The optimization is performed on data using all available statistics of the D^0 sample.

The selections are optimized one by one, meaning that in order to optimize any particular cut its value was varied while all others are kept fixed at their optimal values. The procedure is iterated several times in different orders to ensure stability of the optimal values and their independence on the order of optimization. The final values are chosen conservatively to be slightly softer than the optimal values.

Figure 5.2 shows the relative yield uncertainty versus the cut value for different variables with all other cuts being set to the corresponding pre-selections, final selections, and final selections with the additional cut of $D^0 \chi_{IP}^2 < 9$, respectively.

The $D^0 \chi_{IP}^2 < 9$ cut significantly reduces the background and suppresses the contribution of secondary fraction. With this selection the positions of the optima

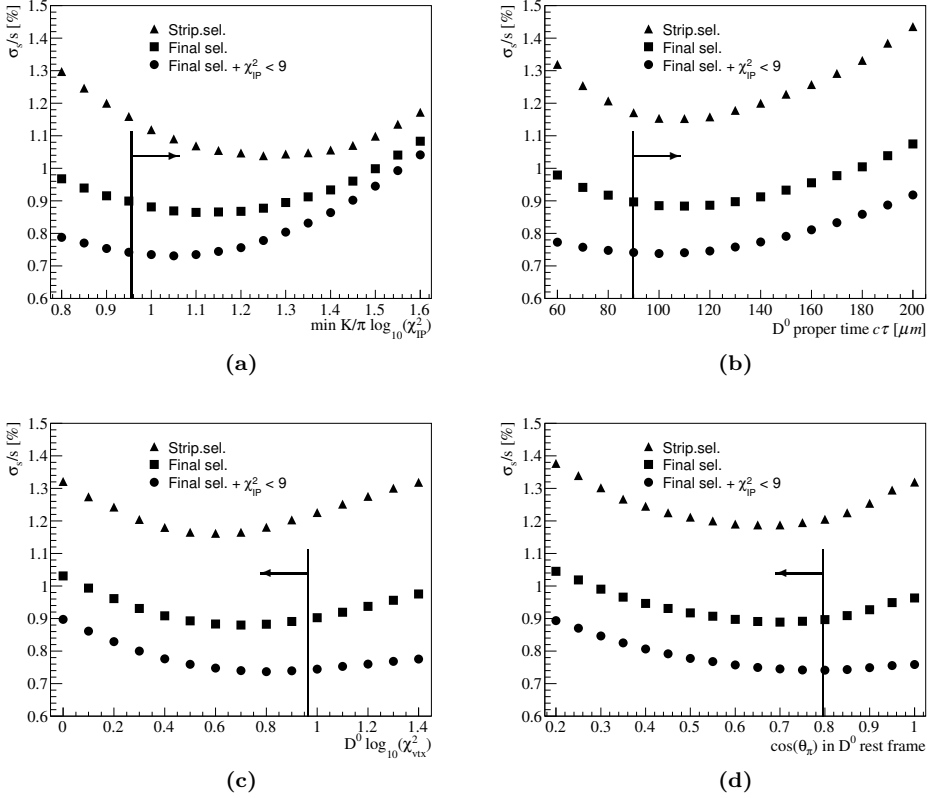


Figure 5.2: Optimization plots for D^0 showing the σ_s/s as a function of kaon/pion χ^2_{IP} (a), D^0 proper time $c\tau$ (b), D^0 χ^2_{vtx} (c), and $\cos(\theta_\pi)$ in the D^0 rest frame (d). The triangles, squares and circles correspond to pre-selections, final selections and final selections with the additional cut of D^0 $\chi^2_{IP} < 9$, respectively. The arrows show the final selections.

do not change, showing that $D^0 \chi_{IP}^2$ is uncorrelated with other variables. Consequently, the fit method used for yield extraction (see Section 5.3) that utilizes the information about $D^0 \chi_{IP}^2$ shape will give the same optima.

It is possible that the optimization results depend on conditions under which the data sample has been taken, and especially on the magnet polarity. For this reason the optimization procedure was checked separately for data with magnetic field up and down, respectively. Both samples give consistent results for the optima.

Other variables are not optimized. For example, the χ_{tr}^2 and d_{KL} criteria are set to values commonly used by other LHCb analyses. The $\log(\mathcal{L}_K/\mathcal{L}_\pi)$ criteria are not optimized due to the pre-selection requirements and large PID systematic effects (see Section 5.5).

Final selection criteria

The list of pre-selection and final selection criteria for D^0 are shown in Table 5.1. The PID requirements applied to the kaon and the pion are not shown and will be discussed in Section 5.4. The list of selection criteria used for D^{*+} , that are applied in addition to D^0 selection criteria, is shown in Table 5.2.

	Variable	Pre-selection	Final selection
h^\pm	χ_{tr}^2		< 5
	d_{KL}		> 5000
	χ_{IP}^2	> 6	> 9
	p	—	$\in [3.2, 100] \text{ GeV}/c$
	p_T	—	$< 5 \text{ GeV}/c$
	η	—	$\in [2.0, 5.0] \text{ GeV}/c$
K^-	$\log(\mathcal{L}_K/\mathcal{L}_\pi)$		> 0
π^+	$\log(\mathcal{L}_K/\mathcal{L}_\pi)$		< 0
D^0	χ_{vtx}^2	< 25	< 9
	$c\tau$	$> 60 \mu\text{m}$	$> 90 \mu\text{m}$
	$\cos(\theta_\pi)$	—	< 0.8
	χ_{IP}^2		< 100
	$m_{K\pi}$		$\in [1790, 1940] \text{ MeV}/c^2$

Table 5.1: Selection criteria for $D^0 \rightarrow K^- \pi^+$ candidates. h denotes the daughter pion or kaon of a D^0 .

	Variable	Pre-selection	Final selection
π^+	χ_{tr}^2		< 5
D^{*+}	χ_{vtx}^2	< 25	< 16
	Δm		$< 155 \text{ MeV}/c^2$

Table 5.2: Selection criteria for $D^{*+} \rightarrow \pi^+ D^0$ candidates.

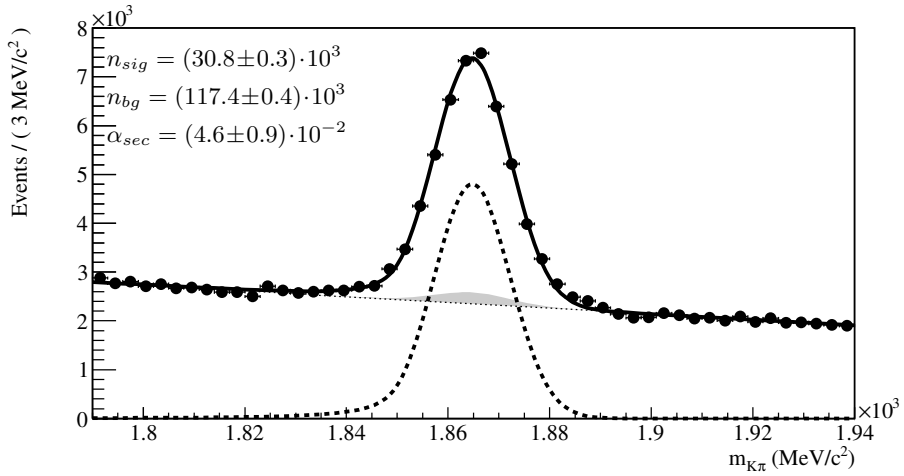


Figure 5.3: The mass distribution $m_{K\pi}$ of D^0 candidates that passed all selections in the kinematic range $0 < p_T < 8 \text{ GeV}/c$ and $2.0 < y < 4.5$. n_{sig} and n_{bg} are the total number of D^0 and background events in the full mass range, respectively.

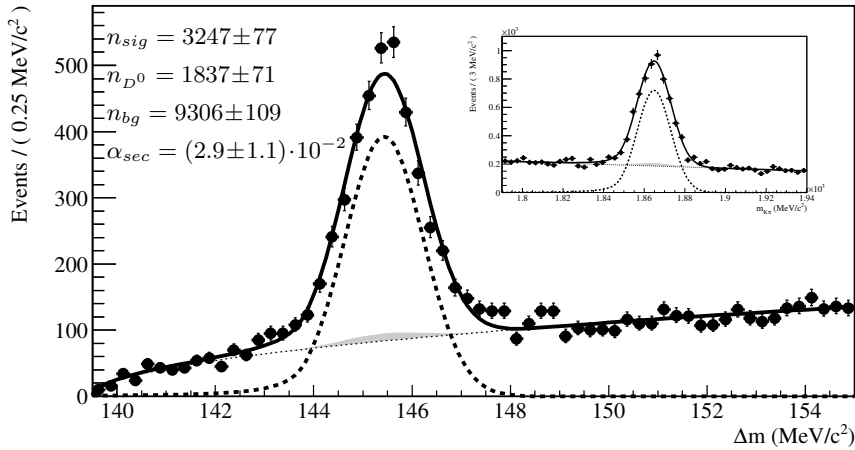


Figure 5.4: The distribution of the mass difference Δm of D^{*+} candidates that passed all selections in the kinematic range $0 < p_T < 8 \text{ GeV}/c$ and $2.0 < y < 4.5$. n_{sig} , n_{D^0} and n_{bg} are the total number of D^{*+} , D^0 and background events, respectively. The inner plot shows $m_{K\pi}$ distribution of the D^0 candidates in the D^{*+} sample.

After all D^0 selections in total 149682 D^0 candidates were selected. Figure 5.3 shows the distribution of the reconstructed D^0 mass $m_{K\pi}$ for these candidates. The total number of prompt D^0 is extracted from the fit to the $m_{K\pi}$ and $\log_{10}(\chi_{IP}^2)$ distribution. The fit is described in detail in the next section. The total number of prompt D^0 is found to be $n_{sig} = 30759 \pm 304$ and the secondary fraction $\alpha_{sec} = (4.6 \pm 0.9) \cdot 10^{-2}$.

After all D^{*+} selections in total 14544 D^{*+} candidates were selected. Figure 5.4 shows the distribution of the mass difference Δm of the selected D^{*+} candidates. The total number of prompt D^{*+} is extracted from the simultaneous fit to the $m_{K\pi}$, Δm and $\log_{10}(\chi_{IP}^2)$, and is found to be $n_{sig} = 3247 \pm 77$ and the secondary fraction $\alpha_{sec} = (2.9 \pm 1.1) \cdot 10^{-2}$.

5.3 Yield extraction

The yield is extracted through a simultaneous fit to the mass $m_{K\pi}$ and $\log_{10}(\chi_{IP}^2)$ for D^0 , and the mass $m_{K\pi}$, mass difference Δm and $\log_{10}(\chi_{IP}^2)$ for D^{*+} candidates.

The fit is performed with probability density functions (PDF) that are constructed individually for D^0 and D^{*+} . The PDFs contain description of prompt and secondary signal components, and background component.

The D^0 PDF is defined as

$$f(m, x) = n_{bg} \cdot f_{bg}(m) \cdot f_{bg}(x) + n_{sig} \cdot f_{sig}(m) \cdot (f_{sig}(x) + \alpha_{sec} \cdot f_{sec}(x)), \quad (5.2)$$

where m is the invariant mass $m_{K\pi}$, $x = \log_{10}(\chi_{IP}^2)$ is the logarithm of the D^0 χ_{IP}^2 , n_{bg} , n_{sig} and $n_{sec} = \alpha_{sec} \cdot n_{sig}$ are the event numbers of background, prompt and secondary D^0 , respectively, with α_{sec} being the fraction of the secondary component, and $f_{\{bg, sig, sec\}}(\{m, x\})$ are the background, signal and secondary PDFs for m and x , respectively.

The D^{*+} PDF is defined as

$$f(m, \Delta m, x) = n_{bg} \cdot f_{bg}(m) \cdot f_{bg}(\Delta m) \cdot f_{bg}(x) + n_{sig} \cdot f_{sig}(m) \cdot f_{sig}(\Delta m) \cdot (f_{sig}(x) + \alpha_{sec} \cdot f_{sec}(x)) + n_{D^0} \cdot f_{sig}(m) \cdot f_{bg}(\Delta m) \cdot (f_{sig}(x) + \alpha_{sec} \cdot f_{sec}(x)), \quad (5.3)$$

where n_{sig} is the number of prompt D^{*+} , n_{D^0} is the number of D^0 that are not produced via D^{*+} decays, α_{sec} is the secondary fraction, and $f_{\{bg, sig\}}(\Delta m)$ are the background and signal PDFs for Δm .

The PDFs are normalized such that the fitted parameters $n_{\{bg, sig\}}$ give the observed yields for background and signal events. The fit is performed with the RooFit package [55]. The PDF functions for the signal, background and secondary components for m , Δm and x are shown in Table 5.3.

The $f_{bg}(m)$ is described with the 1st order Chebyshev polynomial PDF:

$$f_{bg}(m) = \frac{(1 - p_m) \cdot (1940 - m) + (1 + p_m) \cdot (m - 1790)}{(1940 - 1790)^2}, \quad (5.4)$$

$f_{bg}(m)$	1 st order Chebyshev polynomial PDF
$f_{sig}(m)$	Crystal Ball PDF, $CB(m, \mu_m, \sigma_m, \alpha_m)$
$f_{bg}(\Delta m)$	$(\Delta m - m_\pi)^{p_{\Delta m}}$
$f_{sig}(\Delta m)$	Crystal Ball PDF, $CB(\Delta m, \mu_{\Delta m}, \sigma_{\Delta m}, \alpha_{\Delta m})$
$f_{bg}(x)$	$AGE(x, \mu_{ip/bg}, \sigma_{ip/bg}, 0, \rho_{ip/bg}, \rho_{ip/bg})$
$f_{sig}(x)$	$AGE(x, \mu_{ip/sig}, \sigma_{ip/sig}, \varepsilon_{ip/sig}, \rho_{L,ip/sig}, \rho_{R,ip/sig})$
$f_{sec}(x)$	$AGE(x, \mu_{ip/sec}, \sigma_{ip/sec}, 0, \rho_{ip/sec}, \rho_{ip/sec})$

Table 5.3: PDF components. The details of the PDF functions are explained in the text.

where parameter p_m is defined in range $[-1, 1]$ and describes the background slope. The Crystal Ball PDF [56] is defined as

$$CB(x, \mu, \sigma, \alpha, n) = \begin{cases} \exp(-\frac{(x-\mu)^2}{2\cdot\sigma^2}) & \text{if } \mu - \alpha \cdot \sigma < x \\ \frac{(n/\alpha)^n \cdot \exp(-\alpha^2/2)}{((x-\mu)/\sigma + n/\alpha - \alpha)^n} & \text{if } x < \mu - \alpha \cdot \sigma \end{cases} \quad (5.5)$$

where α defines where the tail behavior starts in numbers of σ . The parameter $n = 2$ is fixed.³

The $AGE(x, \mu, \sigma, \varepsilon, \rho_L, \rho_R)$ PDF is an asymmetrical Gaussian with exponential tails and is defined as

$$AGE(x, \mu, \sigma, \varepsilon, \rho_L, \rho_R) = \begin{cases} \exp(\frac{\rho_L^2}{2} + \frac{x-\mu}{\sigma \cdot (1-\varepsilon)} \cdot \rho_L) & \text{if } x < \mu - \rho_L \cdot \sigma \cdot (1 - \varepsilon) \\ \exp(-\frac{(x-\mu)^2}{2 \cdot \sigma^2 \cdot (1-\varepsilon)^2}) & \text{if } \mu - \rho_L \cdot \sigma \cdot (1 - \varepsilon) < x < \mu \\ \exp(-\frac{(x-\mu)^2}{2 \cdot \sigma^2 \cdot (1+\varepsilon)^2}) & \text{if } \mu < x < \mu + \rho_R \cdot \sigma \cdot (1 + \varepsilon) \\ \exp(\frac{\rho_R^2}{2} - \frac{x-\mu}{\sigma \cdot (1+\varepsilon)} \cdot \rho_R) & \text{if } \mu + \rho_R \cdot \sigma \cdot (1 + \varepsilon) < x \end{cases} \quad (5.6)$$

The parameters $\rho_{\{L,R\}}$ define how many sigmas from the center the exponential behavior starts, and the asymmetry parameter ε allows to describe the width of the PDF with only parameter σ , when both ρ and ε are fixed. In case of background and secondary components ($f_{bg}(x)$ and $f_{sec}(x)$), AGE is reduced to a symmetrical form with $\varepsilon = 0$ and $\rho = \rho_L = \rho_R$.

Figures 5.5 and 5.6 show fits to the data in the kinematic range of $0 < p_T < 8 \text{ GeV}/c$ and $2.0 < y < 4.5$ for D^0 and D^{*+} , respectively, with the above PDFs (Eqs. (5.2) and (5.3)).

The shapes of the prompt and secondary $\log_{10}(\chi_{IP}^2)$ distributions are extracted from MC and were fixed during the fit to data. Due to the cut of $\chi_{IP}^2 < 100$ the shift of the IP distribution for the secondary component can not be extracted from the fit to the data and was fixed to the value obtained from the fit to the MC distributions (Fig. 5.5 (a) and Fig. 5.6 (a)).

To extract yields in (p_T, y) bins the kinematic range was first divided into large bins. For D^0 the large bins are defined in two dimensions with p_T binning: from 0 to 2, from 2 to 4, and from 4 to 8 GeV/c, whereas the bins in rapidity went from 2.0 to 3.0, from 3.0 to 3.5, and from 3.5 to 4.5. In total there are nine large bins. For

³ $n = 1$ leads to a divergent integral, and $n = 2$ is chosen as simplest case.

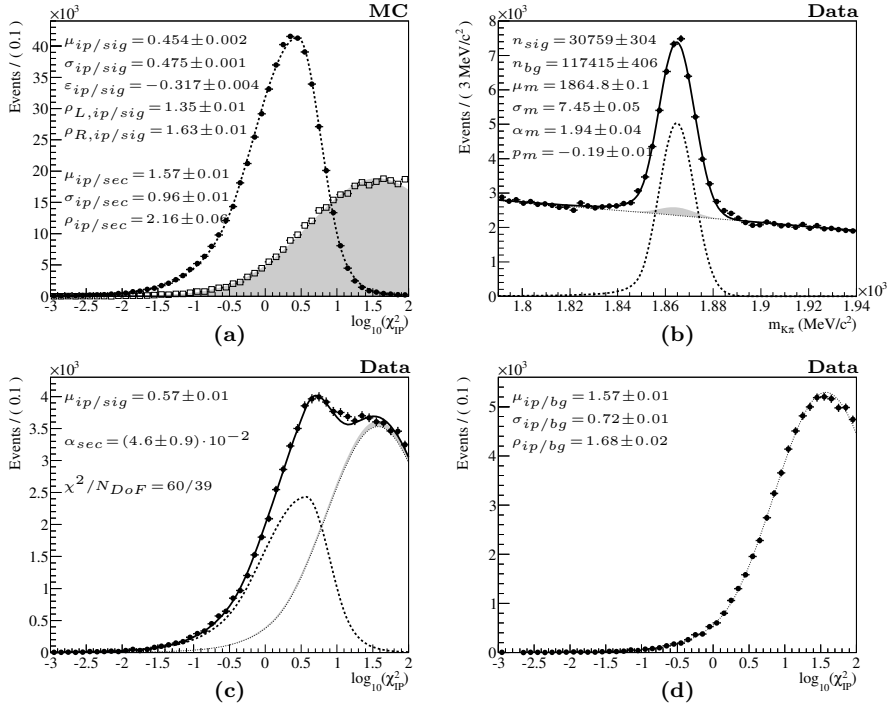


Figure 5.5: Fit to the D^0 data. (a) The distribution of prompt (circles) and secondary (open squares) $D^0 \log_{10}(\chi^2_{IP})$ in MC with overlaid fit projections. (b) The distribution of $D^0 m_{K\pi}$ in data with the overlaid fit projection. (c) and (d) The distribution of $D^0 \log_{10}(\chi^2_{IP})$ in data with the overlaid fit projection with $|m_{K\pi} - 1865| < 30$ (signal) and $|m_{K\pi} - 1865| > 30$ (background), respectively. The dashed line, shaded area and dotted line show the prompt, secondary and background fit components, respectively.

p_T (GeV/c)	y				
	(2.0, 2.5)	(2.5, 3.0)	(3.0, 3.5)	(3.5, 4.0)	(4.0, 4.5)
(0, 1)	815.1 \pm 39.1	1840.2 \pm 66.5	1947.5 \pm 78.6	1357.4 \pm 70.7	481.0 \pm 45.0
(1, 2)	1201.1 \pm 47.2	2972.6 \pm 82.8	2899.3 \pm 87.2	2030.7 \pm 81.5	710.9 \pm 45.3
(2, 3)	1003.1 \pm 37.2	2246.7 \pm 57.4	2043.0 \pm 56.6	1387.5 \pm 48.2	434.9 \pm 27.9
(3, 4)	688.6 \pm 29.3	1244.2 \pm 39.3	1185.3 \pm 39.6	712.3 \pm 31.5	175.9 \pm 14.7
(4, 5)	395.0 \pm 20.8	651.1 \pm 27.1	601.3 \pm 27.8	337.2 \pm 21.2	44.8 \pm 6.8
(5, 6)	202.2 \pm 14.3	350.0 \pm 19.0	245.2 \pm 16.2	143.6 \pm 12.6	10.7 \pm 3.2
(6, 7)	92.5 \pm 9.5	127.7 \pm 11.1	87.8 \pm 9.6	49.4 \pm 7.2	
(7, 8)	30.5 \pm 5.4	45.6 \pm 6.7	21.9 \pm 4.7	10.7 \pm 3.2	

Table 5.4: Prompt D^0 raw yields. Dotted lines indicate the large bins.

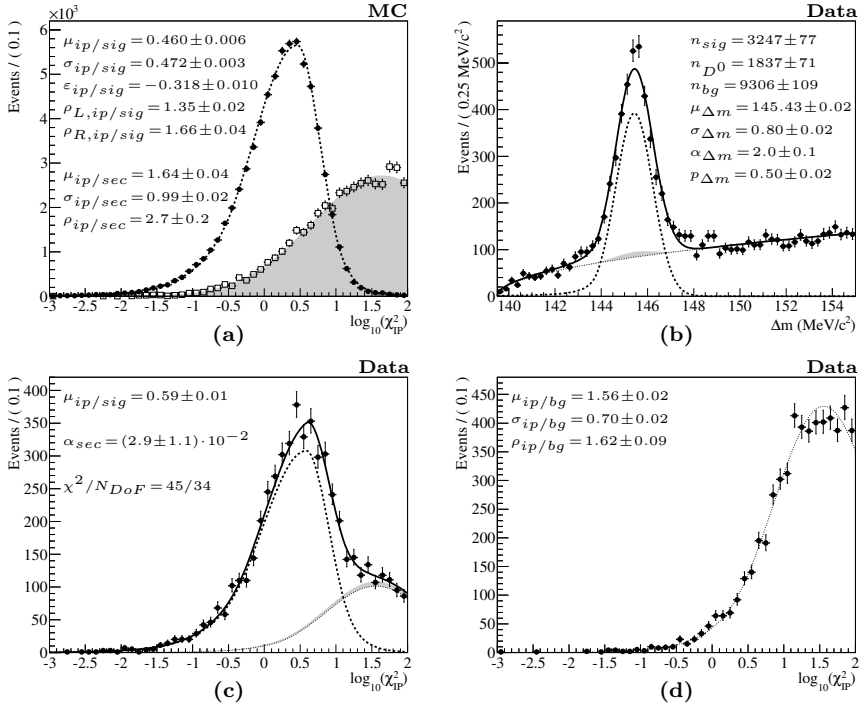


Figure 5.6: Fit to the D^{*+} in data. (a) The distribution of prompt (circles) and secondary (open squares) D^0 $\log_{10}(\chi^2_{IP})$ in MC. (b) The distribution of D^{*+} Δm in data with the overlaid fit projection. (c) and (d) The distribution of D^0 $\log_{10}(\chi^2_{IP})$ in data with the overlaid fit projection with $|m_{K\pi} - 1865| < 30$ and $|\Delta m - 145.5| < 3.0$ (signal), and $|m_{K\pi} - 1865| > 30$ (background), respectively. The dashed line, shaded area and dotted line show the prompt, secondary and background fit components, respectively.

p_T (GeV/c)	y				
	(2.0, 2.5)	(2.5, 3.0)	(3.0, 3.5)	(3.5, 4.0)	(4.0, 4.5)
(0, 1)			43.8 ± 8.6	74.7 ± 12.3	31.5 ± 8.6
(1, 2)		74.8 ± 9.5	379.6 ± 24.2	295.5 ± 23.7	96.5 ± 13.1
(2, 3)		155.8 ± 13.2	350.0 ± 21.7	282.5 ± 20.8	89.3 ± 11.4
(3, 4)	25.7 ± 5.1	193.5 ± 14.2	265.6 ± 17.9	168.4 ± 14.7	29.0 ± 6.0
(4, 5)	39.4 ± 6.4	107.5 ± 11.2	143.6 ± 13.1	80.8 ± 9.5	14.0 ± 4.2
(5, 6)	21.6 ± 4.6	71.0 ± 8.7	74.7 ± 9.2	34.2 ± 6.1	
(6, 7)	16.2 ± 4.0	30.6 ± 5.6	19.4 ± 4.7	8.9 ± 3.1	
(7, 8)	8.3 ± 2.8	13.0 ± 3.6	3.8 ± 1.9		

Table 5.5: Prompt D^{*+} raw yields. Dotted lines indicate the large bins.

the D^{*+} the binning in p_T is from 0 to 4, and from 4 to 8 GeV/c, with the rapidity binning the same as in the D^0 case, which gives six large bins for the D^{*+} .

Every large bin is further divided into smaller bins with a binning of 1 GeV/c for p_T and 0.5 units for rapidity. In each large bin a simultaneous fit to the D^0 (D^{*+}) data is performed with the corresponding PDF.

The simultaneous PDFs are defined for every large bin with some of the parameters defined per small bin and other parameters shared between small bins. The selection of parameters, which were determined individually in each small bin, was based on the amount of statistics available in the large bin. In the D^0 case for the large bins with $p_T < 4$ GeV/c the parameters determined in each small bin include the signal and background yields, the signal mass shape parameters μ_m and σ_m , the background parameter p_m and the χ^2_{IP} shape parameters $\mu_{ip/\{bg,sig,sec\}}$ and $\sigma_{ip/\{bg,sig,sec\}}$; all other parameters were common between all small bins of one large bin. For large bins with $p_T > 4$ GeV/c the signal and background yields are small and it is not possible to constrain all parameters in small bins. For these bins, only the yield parameters were defined per small bin. In the D^{*+} case for large bins with $p_T < 4$ GeV/c, the parameters determined per small bin are the signal and background yields, the signal mass parameters μ_m and σ_m , the background parameters p_m and p_{dm} , and the prompt χ^2_{IP} shape parameters $\mu_{ip/sig}$ and $\sigma_{ip/sig}$. For large bins with $p_T > 4$ GeV/c, only yield parameters are defined per small bin.

The initial values for the parameters describing the χ^2_{IP} shapes were taken from MC by fitting the corresponding distributions with χ^2_{IP} PDFs $f_{\{bg,sig,sec\}}(x)$. The shape of the prompt χ^2_{IP} distribution is well described by MC, and to stabilize the fit to the data the parameters $\sigma_{ip/sig}$, $\varepsilon_{ip/sig}$, $\rho_{L,ip/sig}$ and $\rho_{R,ip/sig}$ were fixed from the fit to the MC prompt χ^2_{IP} distribution, leaving only the mean as free parameter. As was pointed out, due to the cut of $\chi^2_{IP} < 100$ it is not possible to extract the mean of the secondary shape from the fit to data, consequently in addition to the shape parameters of the secondary χ^2_{IP} distribution the mean was also fixed from the fit to MC secondary χ^2_{IP} distribution, i.e. $\mu_{ip/sec}$, $\sigma_{ip/sec}$ and $\rho_{ip/sec}$.

Individual fits for each large bin are shown in Appendix B. Tables 5.4 and 5.5 show the raw yields for D^0 and D^{*+} in (p_T, y) bins extracted with the fit procedure described above.

5.4 Efficiency

The full event and detector simulation is used for signal studies and to estimate the generator, selection and PID efficiency. The signal event samples were generated with PYTHIA, followed by a full GEANT event simulation and LHCb reconstruction.

Generator efficiency

During the event generation only the events in which all charged particles of the final state have their momentum vector pointing into the angular acceptance of the LHCb are saved and subsequently available for analysis. This requirement is referred to as the generator cut. The efficiency of this cut was determined using the generator-level MC, where the samples of D^0 and D^{*+} were generated with no cut

p_T (GeV/ c)	y				
	(2.0, 2.5)	(2.5, 3.0)	(3.0, 3.5)	(3.5, 4.0)	(4.0, 4.5)
(0, 1)	75.14 \pm 0.40	91.75 \pm 0.27	95.12 \pm 0.22	90.96 \pm 0.32	77.55 \pm 0.52
(1, 2)	79.81 \pm 0.35	93.71 \pm 0.22	97.07 \pm 0.17	93.99 \pm 0.26	82.89 \pm 0.47
(2, 3)	86.00 \pm 0.40	96.68 \pm 0.22	98.31 \pm 0.17	95.94 \pm 0.30	87.81 \pm 0.58
(3, 4)	90.79 \pm 0.46	98.62 \pm 0.20	99.18 \pm 0.17	97.31 \pm 0.36	92.43 \pm 0.70
(4, 5)	93.38 \pm 0.55	99.49 \pm 0.17	99.51 ^{+0.16} _{-0.21}	99.07 ^{+0.28} _{-0.35}	96.80 \pm 0.67
(5, 6)	95.96 \pm 0.60	99.90 ^{+0.08} _{-0.15}	99.86 ^{+0.10} _{-0.21}	99.81 ^{+0.14} _{-0.28}	97.81 ^{+0.73} _{-0.93}
(6, 7)	97.04 \pm 0.69	100.00 ⁺⁰ _{-0.21}	100.00 ⁺⁰ _{-0.30}	99.59 ^{+0.30} _{-0.62}	96.93 ^{+1.18} _{-1.57}
(7, 8)	97.93 ^{+0.69} _{-0.88}	100.00 ⁺⁰ _{-0.42}	100.00 ⁺⁰ _{-0.47}	100.00 ⁺⁰ _{-0.77}	100.00 ⁺⁰ _{-1.84}

Table 5.6: Generator efficiency (in %) for $D^0 \rightarrow K^- \pi^+$ in bins of (p_T, y) .

p_T (GeV/ c)	y				
	(2.0, 2.5)	(2.5, 3.0)	(3.0, 3.5)	(3.5, 4.0)	(4.0, 4.5)
(0, 1)	74.45 \pm 0.36	88.38 \pm 0.28	86.49 \pm 0.31	69.64 \pm 0.45	36.71 \pm 0.52
(1, 2)	79.04 \pm 0.30	93.62 \pm 0.19	96.87 \pm 0.15	93.35 \pm 0.23	75.93 \pm 0.45
(2, 3)	85.71 \pm 0.33	95.95 \pm 0.20	98.78 \pm 0.12	95.22 \pm 0.27	87.21 \pm 0.48
(3, 4)	90.39 \pm 0.38	98.17 \pm 0.19	98.62 \pm 0.18	97.35 \pm 0.28	91.25 \pm 0.59
(4, 5)	92.85 \pm 0.44	99.29 \pm 0.16	99.86 ^{+0.07} _{-0.10}	98.66 \pm 0.28	95.48 \pm 0.63
(5, 6)	96.19 \pm 0.45	99.63 ^{+0.13} _{-0.18}	99.84 ^{+0.09} _{-0.15}	99.35 ^{+0.23} _{-0.30}	97.91 \pm 0.62
(6, 7)	96.63 \pm 0.55	100.00 ^{+0.00} _{-0.13}	99.86 ^{+0.10} _{-0.21}	99.59 ^{+0.23} _{-0.38}	98.61 ^{+0.59} _{-0.83}
(7, 8)	98.42 \pm 0.50	99.81 ^{+0.14} _{-0.29}	100.00 ^{+0.00} _{-0.29}	100.00 ^{+0.00} _{-0.48}	100.00 ^{+0.00} _{-0.75}

Table 5.7: Generator efficiency (in %) for $D^{*+} \rightarrow \pi^+ D^0 (K^- \pi^+)$ in bins of (p_T, y) .

applied. The generator efficiency ε_{gen} was determined in (p_T, y) bins of generated D^0 and D^{*+} particles as the fraction of events that have passed the generator cut.

In total 0.5M signal events were generated for each signal mode and for each magnet polarity. The generator efficiency for the D^0 and D^{*+} are shown in Tables 5.6 and 5.7, respectively.

Selection and reconstruction efficiency

The selection efficiency is estimated using the signal MC event samples. The signal MC sample for every generated event contains the D^0 decaying to $K^- \pi^+$ or D^{*+} decaying to $D^0 \pi^+$, where D^0 decays to $K^- \pi^+$. The charm mesons are mainly produced promptly from the primary vertex but can also be produced in the decay of B mesons (secondary production). The selection efficiency is calculated using promptly produced charm mesons.

The efficiency is defined as the number of true D^0 (D^{*+}) reconstructed candi-

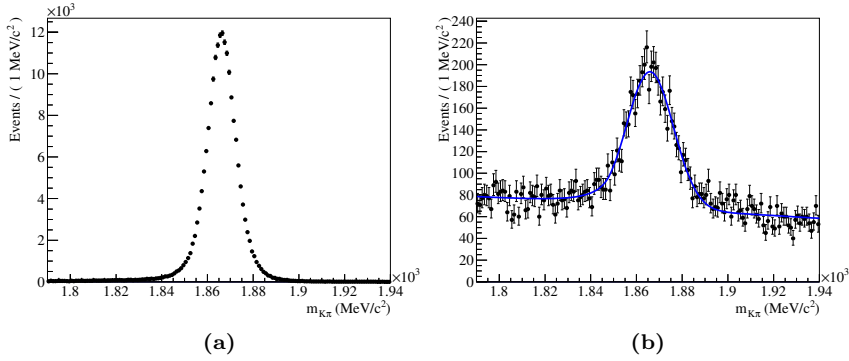


Figure 5.7: Fully (a) and partially (b) matched D^0 candidates. The number of partially matched candidates is extracted from the fit to the corresponding mass distribution.

p_T (GeV/ c)	y				
	(2.0, 2.5)	(2.5, 3.0)	(3.0, 3.5)	(3.5, 4.0)	(4.0, 4.5)
(0, 1)	0.49 ± 0.18	0.94 ± 0.16	1.85 ± 0.23	2.25 ± 0.29	2.14 ± 0.38
(1, 2)	1.06 ± 0.21	1.16 ± 0.17	1.87 ± 0.21	2.60 ± 0.31	2.02 ± 0.38
(2, 3)	0.85 ± 0.19	1.21 ± 0.16	2.07 ± 0.19	2.50 ± 0.29	2.88 ± 0.45
(3, 4)	0.97 ± 0.21	1.41 ± 0.18	2.01 ± 0.23	2.97 ± 0.33	2.72 ± 0.60
(4, 5)	1.01 ± 0.24	1.52 ± 0.27	2.20 ± 0.33	3.23 ± 0.44	4.18 ± 1.24
(5, 6)	1.11 ± 0.29	1.80 ± 0.37	3.22 ± 0.47	3.84 ± 0.70	3.89 ± 2.58
(6, 7)	1.26 ± 0.47	2.26 ± 0.54	2.43 ± 0.63	0.74 ± 0.57	
(7, 8)	0.00 ± 1.57	2.46 ± 1.06	3.77 ± 1.22	4.45 ± 2.32	

Table 5.8: Fraction of partially matched D^0 candidates (in %).

p_T (GeV/ c)	y				
	(2.0, 2.5)	(2.5, 3.0)	(3.0, 3.5)	(3.5, 4.0)	(4.0, 4.5)
(0, 1)	6242 ± 80	15007 ± 124	14723 ± 125	9966 ± 103	4298 ± 67
(1, 2)	7990 ± 90	17645 ± 135	16342 ± 131	11016 ± 109	4391 ± 68
(2, 3)	6116 ± 79	12426 ± 113	11245 ± 107	7389 ± 88	2733 ± 53
(3, 4)	4399 ± 67	8069 ± 90	6972 ± 84	4711 ± 69	1322 ± 37
(4, 5)	2951 ± 55	4640 ± 69	3926 ± 63	2540 ± 51	434 ± 21
(5, 6)	1592 ± 40	2420 ± 50	1900 ± 44	1131 ± 34	89 ± 10
(6, 7)	756 ± 28	983 ± 31	770 ± 28	442 ± 21	
(7, 8)	309 ± 18	367 ± 19	265 ± 16	102 ± 10	

Table 5.9: Corrected number of D^0 candidates.

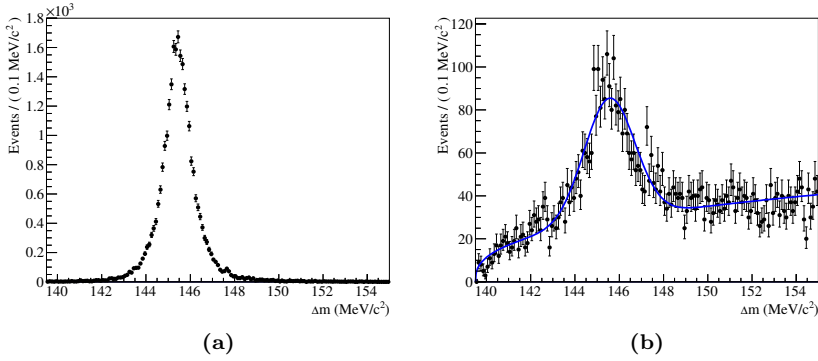


Figure 5.8: Fully (a) and partially (b) matched D^{*+} candidates. The number of partially matched candidates is extracted from the fit to the corresponding mass distribution.

p_T (GeV/ c)	y				
	(2.0, 2.5)	(2.5, 3.0)	(3.0, 3.5)	(3.5, 4.0)	(4.0, 4.5)
(0, 1)			3.80 ± 2.03	7.26 ± 2.34	5.05 ± 3.73
(1, 2)		7.22 ± 1.90	7.29 ± 1.03	8.64 ± 1.14	7.77 ± 1.77
(2, 3)		4.04 ± 0.93	6.81 ± 0.82	7.02 ± 0.93	5.02 ± 1.40
(3, 4)	3.59 ± 1.71	5.63 ± 0.87	5.80 ± 0.79	5.41 ± 0.91	7.86 ± 1.91
(4, 5)	0.93 ± 1.08	4.86 ± 0.94	3.81 ± 0.74	5.86 ± 1.06	5.01 ± 2.24
(5, 6)	1.95 ± 1.17	5.64 ± 1.09	3.74 ± 0.99	6.63 ± 1.52	
(6, 7)	1.29 ± 1.26	4.57 ± 1.39	7.07 ± 1.77	7.99 ± 2.37	
(7, 8)	0.68 ± 1.59	2.59 ± 1.47	4.00 ± 2.23		

Table 5.10: Fraction of partially matched D^{*+} candidates (in %).

p_T (GeV/ c)	y				
	(2.0, 2.5)	(2.5, 3.0)	(3.0, 3.5)	(3.5, 4.0)	(4.0, 4.5)
(0, 1)			547 ± 25	576 ± 27	171 ± 14
(1, 2)		548 ± 25	3046 ± 62	2422 ± 54	827 ± 31
(2, 3)		1333 ± 38	2989 ± 58	2095 ± 48	676 ± 27
(3, 4)	261 ± 16	1525 ± 40	2153 ± 48	1413 ± 39	397 ± 21
(4, 5)	342 ± 19	1233 ± 36	1316 ± 37	821 ± 29	140 ± 12
(5, 6)	254 ± 16	723 ± 27	688 ± 27	419 ± 21	
(6, 7)	177 ± 13	374 ± 20	335 ± 19	181 ± 14	
(7, 8)	70 ± 8	157 ± 13	110 ± 11		

Table 5.11: Corrected number of D^{*+} candidates.

p_T (GeV/ c)	y				
	(2.0, 2.5)	(2.5, 3.0)	(3.0, 3.5)	(3.5, 4.0)	(4.0, 4.5)
(0, 1)	5.62 ± 0.07	12.13 ± 0.11	12.86 ± 0.12	10.54 ± 0.11	6.48 ± 0.10
(1, 2)	5.96 ± 0.07	12.45 ± 0.10	13.00 ± 0.11	10.95 ± 0.11	6.45 ± 0.10
(2, 3)	7.75 ± 0.10	15.84 ± 0.15	16.80 ± 0.17	14.23 ± 0.18	7.79 ± 0.16
(3, 4)	10.14 ± 0.16	19.84 ± 0.24	20.92 ± 0.28	18.69 ± 0.30	7.86 ± 0.23
(4, 5)	12.48 ± 0.24	22.11 ± 0.36	23.07 ± 0.41	20.24 ± 0.44	5.38 ± 0.27
(5, 6)	12.18 ± 0.32	21.36 ± 0.48	21.53 ± 0.55	17.66 ± 0.57	2.27 ± 0.25
(6, 7)	10.33 ± 0.40	15.82 ± 0.54	16.00 ± 0.62	12.94 ± 0.66	
(7, 8)	7.02 ± 0.43	10.11 ± 0.56	9.64 ± 0.62	5.77 ± 0.59	

Table 5.12: $D^0 \rightarrow K^- \pi^+$ reconstruction efficiency (in %) in bins of (p_T, y) .

p_T (GeV/ c)	y				
	(2.0, 2.5)	(2.5, 3.0)	(3.0, 3.5)	(3.5, 4.0)	(4.0, 4.5)
(0, 1)			1.59 ± 0.07	2.44 ± 0.11	1.63 ± 0.14
(1, 2)		1.10 ± 0.05	6.77 ± 0.14	6.87 ± 0.16	3.60 ± 0.14
(2, 3)		4.44 ± 0.13	11.80 ± 0.24	10.48 ± 0.25	5.10 ± 0.21
(3, 4)	1.54 ± 0.10	9.48 ± 0.26	15.89 ± 0.38	14.11 ± 0.41	5.89 ± 0.31
(4, 5)	3.52 ± 0.20	13.97 ± 0.44	18.83 ± 0.57	15.60 ± 0.59	4.13 ± 0.36
(5, 6)	4.59 ± 0.30	14.99 ± 0.60	17.61 ± 0.74	15.31 ± 0.81	
(6, 7)	5.58 ± 0.43	13.67 ± 0.76	15.10 ± 0.90	11.54 ± 0.91	
(7, 8)	3.79 ± 0.46	9.33 ± 0.78	9.24 ± 0.92		

Table 5.13: $D^{*+} \rightarrow \pi^+ D^0(K^- \pi^+)$ reconstruction efficiency (in %) in bins of (p_T, y) .

dates that have passed the same selections as are used for the data (except PID), divided by the total number of generated charm mesons in a specific (p_T, y) bin:

$$\varepsilon_{sel}(i) = \frac{N_{sel}(i)}{N_{gen}(i)}, \quad (5.7)$$

where $N_{sel}(i)$ is the number of reconstructed D^0 (D^{*+}) that have passed all selections, $N_{gen}(i)$ is the number of events that have passed the generator cut, and index i denotes the (p_T, y) bin.

The number of true charm mesons is obtained by performing “truth” matching, which requires that all final state particles in the decay of a charm meson are matched to reconstructed tracks. This procedure has an inefficiency associated with the matching algorithm, consequently underestimating the yield. The correction for this effect is determined by performing the fit in (p_T, y) bins to the $m_{K\pi}$ of the D^0 or Δm of the D^{*+} candidates for which all tracks but one are matched. This

procedure allows to reduce the effect of the matching inefficiency to a negligible level.

Due to limited MC statistics the fit is performed in large and small bins, similar to the fit to data, however, only signal (partially matched candidates) and background yields are defined per small bin.

Figure 5.7 shows the reconstructed mass of the D^0 candidates for fully matched and partially matched candidates. The fit to partially matched candidates is performed using PDF where the signal is described with CB function (Eq. (5.5)) and background is described with a linear function. Tables 5.8 and 5.9 show the fraction of partially matched D^0 candidates extracted from the fit and the corrected number of D^0 candidates, respectively. The mismatch rate for D^0 candidates varies from 0.5% to 4%. This corresponds to the mismatch rate per track from 0.25% to 2%, assuming the same matching inefficiency for kaon and pion.

Figure 5.8 shows the reconstructed mass of D^{*+} candidates for fully matched and partially matched candidates. The fit to partially matched candidates is performed with PDF where the signal is described with a Gaussian and the background is described with the function $(\Delta m - m_\pi)^p$, where p is a free parameter. Tables 5.10 and 5.11 show the fraction of partially matched D^{*+} candidates extracted from the fit and the corrected number of D^{*+} candidates, respectively. The mismatch rate for D^{*+} candidates varies from 1% to 8%, which is factor of 2 larger than in the D^0 case, and is mainly due to the mismatch of the pion from the D^{*+} .

Tables 5.12 and 5.13 show the reconstruction efficiency in (p_T, y) bins for D^0 and D^{*+} , respectively.

PID efficiency

The PID efficiency is estimated from the data due to the poor description of PID variables in the simulation. To illustrate this, Fig. 5.9 shows a data/MC comparison of the background subtracted PID distributions for kaons and pions.

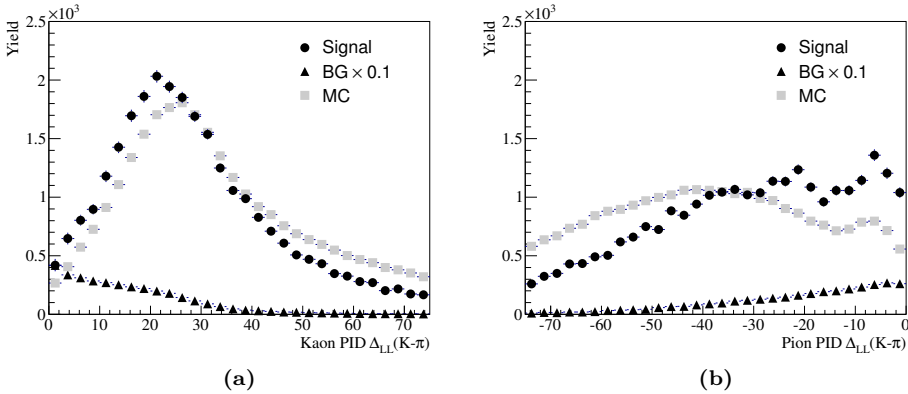


Figure 5.9: Background subtracted distribution of PID likelihood values for kaons (a) and pions (b).

p_T (GeV/c)	y				
	(2.0, 2.5)	(2.5, 3.0)	(3.0, 3.5)	(3.5, 4.0)	(4.0, 4.5)
(0, 1)	87.24 ± 0.10	88.21 ± 0.04	90.35 ± 0.03	90.78 ± 0.03	85.84 ± 0.06
(1, 2)	88.35 ± 0.07	89.58 ± 0.03	91.56 ± 0.03	90.33 ± 0.03	83.69 ± 0.06
(2, 3)	90.29 ± 0.06	92.03 ± 0.03	92.84 ± 0.03	89.72 ± 0.04	81.69 ± 0.08
(3, 4)	92.27 ± 0.06	93.87 ± 0.04	93.80 ± 0.05	88.80 ± 0.06	79.74 ± 0.15
(4, 5)	93.76 ± 0.09	94.70 ± 0.07	93.91 ± 0.08	87.56 ± 0.11	77.41 ± 0.29
(5, 6)	95.09 ± 0.13	95.50 ± 0.13	94.12 ± 0.15	86.37 ± 0.20	76.33 ± 0.44
(6, 7)	96.39 ± 0.20	96.25 ± 0.21	93.95 ± 0.26	84.60 ± 0.36	
(7, 8)	96.90 ± 0.34	96.32 ± 0.36	93.53 ± 0.45	83.48 ± 0.62	

Table 5.14: $D^0 \rightarrow K^- \pi^+$ PID efficiency (in %) in bins of (p_T, y) .

p_T (GeV/c)	y				
	(2.0, 2.5)	(2.5, 3.0)	(3.0, 3.5)	(3.5, 4.0)	(4.0, 4.5)
(0, 1)			90.73 ± 0.03	90.55 ± 0.04	86.27 ± 0.06
(1, 2)		90.13 ± 0.04	91.58 ± 0.03	90.35 ± 0.03	84.00 ± 0.06
(2, 3)		91.97 ± 0.04	92.57 ± 0.03	89.91 ± 0.04	81.95 ± 0.08
(3, 4)	91.85 ± 0.07	93.70 ± 0.04	93.70 ± 0.04	89.25 ± 0.06	80.18 ± 0.13
(4, 5)	93.34 ± 0.09	94.53 ± 0.07	93.80 ± 0.07	87.99 ± 0.09	77.96 ± 0.25
(5, 6)	94.35 ± 0.12	95.25 ± 0.11	93.81 ± 0.12	86.80 ± 0.16	
(6, 7)	95.80 ± 0.17	96.11 ± 0.18	94.32 ± 0.22	86.08 ± 0.28	
(7, 8)	96.69 ± 0.27	96.18 ± 0.30	93.79 ± 0.34		

Table 5.15: $D^{*+} \rightarrow \pi^+ D^0 (K^- \pi^+)$ PID efficiency (in %) in bins of (p_T, y) .

The PID efficiency is estimated using the PID efficiencies of kaons and pions produced in D^0 decays. The kaon and pion PID efficiencies are extracted from data, using the calibration data sample of $K_s^0 \rightarrow \pi^+ \pi^-$ and $\phi \rightarrow K^+ K^-$, in six bins of momentum p and five bins of pseudo-rapidity η :

- p (GeV/c): [3.2, 6.0], [6.0, 9.3], [9.3, 15.6], [15.6, 25.0], [25.0, 40.0], [40.0, 100.0];
- η : [2.0, 2.5], [2.5, 3.0], [3.0, 3.5], [3.5, 4.0], [4.0, 5.0].

This binning scheme is chosen as a compromise between bin size and calibration statistics. Due to the limited statistics of the calibration data samples the region of $\eta > 4.4$ and $p < 8$ GeV/c is vetoed for both kaons and pions. In addition due to RICH acceptance requirements the following kinematic regions are vetoed:

- $2.0 < \eta < 2.5$ and $25 < p < 100$ GeV/c for kaons and pions;
- $3.5 < \eta < 5.0$ and $3.2 < p < 6$ GeV/c for kaons;

- $2.5 < \eta < 3.0$ and $40 < p < 100 \text{ GeV}/c$ for pions;
- $3.0 < \eta < 3.5$ and $60 < p < 100 \text{ GeV}/c$ for pions.

To determine the effect of the PID requirements in the analysis the kaon and pion identification efficiencies are used as weights for reconstructed D^0 candidates in MC. The weight for a given D^0 candidate is calculated as

$$\mathcal{W} = \varepsilon_K \cdot \varepsilon_\pi, \quad (5.8)$$

where ε_K and ε_π are the PID efficiencies of kaons and pions in their corresponding (p, η) bin, respectively.

The PID efficiency for a given (p_T, y) bin of D^0 (D^{*+}) is then calculated as the ratio of weighted matched candidates to the total number of matched candidates (i.e. without PID criteria applied) in this bin:

$$\varepsilon(i) = \frac{\sum_j \mathcal{W}(j)}{N(i)}, \quad (5.9)$$

where index i denotes the (p_T, y) bin of the D^0 (D^{*+}). The sum goes over all MC matched events in bin i and the $N(i)$ is the total number of MC matched candidates in bin i .

A dedicated PID calibration package [57, 58] is used to obtain the PID efficiencies for kaons and pions, as well as a binomial error for the efficiency. The error on the PID efficiency for D^0 (D^{*+}) was calculated using error propagation, assuming no correlation between the kaon and the pion, and their (p, η) bins:

$$\sigma_\varepsilon(i) = \frac{\sqrt{\sum_j (\sigma \mathcal{W}(j))^2}}{N(i)}, \quad (5.10)$$

where $\sigma \mathcal{W} = \sigma(\varepsilon_K) \cdot \varepsilon_\pi + \varepsilon_K \cdot \sigma(\varepsilon_\pi)$.

Tables 5.14 and 5.15 show the PID efficiency for D^0 and D^{*+} in (p_T, y) bins. The errors are calculated using Eq. (5.10).

Total efficiency

The total efficiency is defined as the product of generator, reconstruction and PID efficiency in corresponding (p_T, y) bins:

$$\varepsilon = \varepsilon_{gen} \cdot \varepsilon_{rec} \cdot \varepsilon_{pid}. \quad (5.11)$$

Tables 5.16 and 5.17 show the total efficiency in (p_T, y) bins for D^0 and D^{*+} , respectively. The errors are calculated as the sum of the squares of corresponding efficiency values.

As a cross check the ratio of the efficiencies of D^{*+} to D^0 can be studied. Table 5.18 shows the D^{*+} to D^0 ratios of generator, reconstruction and PID efficiency. The ratio of generator efficiency is approximately 1 in all bins except at very low

p_T (GeV/c)	y				
	(2.0, 2.5)	(2.5, 3.0)	(3.0, 3.5)	(3.5, 4.0)	(4.0, 4.5)
(0, 1)	3.68 ± 0.05	9.82 ± 0.09	11.05 ± 0.10	8.70 ± 0.10	4.32 ± 0.07
(1, 2)	4.20 ± 0.05	10.45 ± 0.09	11.55 ± 0.10	9.30 ± 0.10	4.47 ± 0.08
(2, 3)	6.01 ± 0.09	14.09 ± 0.14	15.33 ± 0.16	12.25 ± 0.16	5.59 ± 0.12
(3, 4)	8.50 ± 0.14	18.37 ± 0.23	19.47 ± 0.26	16.15 ± 0.27	5.79 ± 0.17
(4, 5)	10.93 ± 0.22	20.83 ± 0.34	21.56 ± 0.39	17.55 ± 0.39	4.03 ± 0.20
(5, 6)	11.12 ± 0.30	20.38 ± 0.46	20.23 ± 0.52	15.22 ± 0.50	1.70 ± 0.18
(6, 7)	9.66 ± 0.38	15.23 ± 0.53	15.03 ± 0.59	10.91 ± 0.56	
(7, 8)	6.66 ± 0.41	9.73 ± 0.54	9.02 ± 0.58	4.82 ± 0.50	

Table 5.16: $D^0 \rightarrow K^- \pi^+$ overall efficiency (in %), including reconstruction, generator and PID, in bins of (p_T, y) .

p_T (GeV/c)	y				
	(2.0, 2.5)	(2.5, 3.0)	(3.0, 3.5)	(3.5, 4.0)	(4.0, 4.5)
(0, 1)			1.25 ± 0.06	1.54 ± 0.07	0.52 ± 0.04
(1, 2)		0.93 ± 0.04	6.01 ± 0.12	5.79 ± 0.13	2.30 ± 0.09
(2, 3)		3.92 ± 0.11	10.79 ± 0.22	8.97 ± 0.22	3.64 ± 0.15
(3, 4)	1.28 ± 0.08	8.72 ± 0.24	14.68 ± 0.35	12.26 ± 0.36	4.31 ± 0.23
(4, 5)	3.05 ± 0.17	13.11 ± 0.41	17.64 ± 0.54	13.54 ± 0.52	3.08 ± 0.27
(5, 6)	4.16 ± 0.27	14.22 ± 0.57	16.49 ± 0.69	13.20 ± 0.70	
(6, 7)	5.16 ± 0.40	13.14 ± 0.73	14.22 ± 0.85	9.89 ± 0.78	
(7, 8)	3.60 ± 0.44	8.96 ± 0.75	8.67 ± 0.87		

Table 5.17: $D^{*+} \rightarrow \pi^+ D^0 (K^- \pi^+)$ overall efficiency (in %), including reconstruction, generator and PID, in bins of (p_T, y) .

p_T (GeV/c)	y				
	(2.0, 2.5)	(2.5, 3.0)	(3.0, 3.5)	(3.5, 4.0)	(4.0, 4.5)
(0, 1)	0.991 ± 0.007	0.963 ± 0.004	0.909 ± 0.004	0.766 ± 0.006	0.473 ± 0.007
(1, 2)	0.990 ± 0.006	0.999 ± 0.003	0.998 ± 0.002	0.993 ± 0.004	0.916 ± 0.008
(2, 3)	0.997 ± 0.006	0.993 ± 0.003	1.005 ± 0.002	0.992 ± 0.004	0.993 ± 0.009
(3, 4)	0.996 ± 0.007	0.995 ± 0.003	0.994 ± 0.002	1.000 ± 0.005	0.987 ± 0.010
(4, 5)	0.994 ± 0.008	0.998 ± 0.002	1.004 ± 0.002	0.996 ± 0.004	0.986 ± 0.009
(5, 6)	1.002 ± 0.008	0.997 ± 0.002	1.000 ± 0.002	0.995 ± 0.003	1.001 ± 0.011
(6, 7)	0.996 ± 0.009	1.000 ± 0.002	0.999 ± 0.003	1.000 ± 0.005	1.017 ± 0.016
(7, 8)	1.005 ± 0.009	0.998 ± 0.004	1.000 ± 0.005	1.000 ± 0.008	1.000 ± 0.018

Table 5.18: Ratio of D^{*+} to D^0 generator efficiency in bins of (p_T, y) .

p_T (GeV/c)	y				
	(2.0, 2.5)	(2.5, 3.0)	(3.0, 3.5)	(3.5, 4.0)	(4.0, 4.5)
(0, 1)			0.124 ± 0.006	0.231 ± 0.011	0.251 ± 0.021
(1, 2)		0.089 ± 0.004	0.521 ± 0.012	0.627 ± 0.016	0.559 ± 0.023
(2, 3)		0.280 ± 0.009	0.702 ± 0.016	0.736 ± 0.020	0.654 ± 0.030
(3, 4)	0.152 ± 0.010	0.478 ± 0.014	0.759 ± 0.021	0.755 ± 0.025	0.749 ± 0.045
(4, 5)	0.282 ± 0.017	0.632 ± 0.022	0.816 ± 0.029	0.771 ± 0.034	0.768 ± 0.077
(5, 6)	0.377 ± 0.026	0.702 ± 0.032	0.818 ± 0.040	0.867 ± 0.054	
(6, 7)	0.540 ± 0.047	0.864 ± 0.057	0.944 ± 0.067	0.891 ± 0.084	
(7, 8)	0.539 ± 0.073	0.924 ± 0.093	0.958 ± 0.114		

Table 5.19: Ratio of D^{*+} to D^0 reconstruction efficiency in bins of (p_T, y) .

p_T (GeV/c)	y				
	(2.0, 2.5)	(2.5, 3.0)	(3.0, 3.5)	(3.5, 4.0)	(4.0, 4.5)
(0, 1)			1.004 ± 0.001	0.998 ± 0.001	1.005 ± 0.001
(1, 2)		1.006 ± 0.001	1.000 ± 0.001	1.000 ± 0.001	1.004 ± 0.001
(2, 3)		0.999 ± 0.001	0.997 ± 0.001	1.002 ± 0.001	1.003 ± 0.001
(3, 4)	0.996 ± 0.001	0.998 ± 0.001	0.999 ± 0.001	1.005 ± 0.001	1.006 ± 0.003
(4, 5)	0.996 ± 0.001	0.998 ± 0.001	0.999 ± 0.001	1.005 ± 0.002	1.007 ± 0.005
(5, 6)	0.992 ± 0.002	0.997 ± 0.002	0.997 ± 0.002	1.005 ± 0.003	
(6, 7)	0.994 ± 0.003	0.999 ± 0.003	1.004 ± 0.004	1.017 ± 0.005	
(7, 8)	0.998 ± 0.004	0.999 ± 0.005	1.003 ± 0.006		

Table 5.20: Ratio of D^{*+} to D^0 PID efficiency in bins of (p_T, y) .

p_T and high y , where the pion from the D^{*+} can escape the detector. The PID efficiency ratio is approximately 1 in all bins, showing that in the same (p_T, y) bin the kinematic of D^0 and D^0 from D^{*+} are approximately the same. The reconstruction efficiency ratio effectively corresponds to the reconstruction efficiency of the pion produced in the D^{*+} decay, depending on the kinematics of the D^{*+} .

Efficiency corrected yields

The efficiency corrected yields are calculated as the raw yield divided by the total efficiency. Tables 5.21 and 5.22 show the efficiency corrected yields in (p_T, y) bins for D^0 and D^{*+} , respectively. The errors show only the statistical uncertainty. The errors in the efficiency are regarded as a systematic uncertainty and are discussed in the next section.

p_T (GeV/ c)	y				
	(2.0, 2.5)	(2.5, 3.0)	(3.0, 3.5)	(3.5, 4.0)	(4.0, 4.5)
(0, 1)	815.1 ± 39.1	1840.2 ± 66.5	1947.5 ± 78.6	1357.4 ± 70.7	481.0 ± 45.0
(1, 2)	1201.1 ± 47.2	2972.6 ± 82.8	2899.3 ± 87.2	2030.7 ± 81.5	710.9 ± 45.3
(2, 3)	1003.1 ± 37.2	2246.7 ± 57.4	2043.0 ± 56.6	1387.5 ± 48.2	434.9 ± 27.9
(3, 4)	688.6 ± 29.3	1244.2 ± 39.3	1185.3 ± 39.6	712.3 ± 31.5	175.9 ± 14.7
(4, 5)	395.0 ± 20.8	651.1 ± 27.1	601.3 ± 27.8	337.2 ± 21.2	44.8 ± 6.8
(5, 6)	202.2 ± 14.3	350.0 ± 19.0	245.2 ± 16.2	143.6 ± 12.6	10.7 ± 3.2
(6, 7)	92.5 ± 9.5	127.7 ± 11.1	87.8 ± 9.6	49.4 ± 7.2	
(7, 8)	30.5 ± 5.4	45.6 ± 6.7	21.9 ± 4.7	10.7 ± 3.2	

Table 5.21: $D^0 \rightarrow K^- \pi^+$ efficiency corrected yields.

p_T (GeV/ c)	y				
	(2.0, 2.5)	(2.5, 3.0)	(3.0, 3.5)	(3.5, 4.0)	(4.0, 4.5)
(0, 1)			43.8 ± 8.6	74.7 ± 12.3	31.5 ± 8.6
(1, 2)		74.8 ± 9.5	379.6 ± 24.2	295.5 ± 23.7	96.5 ± 13.1
(2, 3)		155.8 ± 13.2	350.0 ± 21.7	282.5 ± 20.8	89.3 ± 11.4
(3, 4)	25.7 ± 5.1	193.5 ± 14.2	265.6 ± 17.9	168.4 ± 14.7	29.0 ± 6.0
(4, 5)	39.4 ± 6.4	107.5 ± 11.2	143.6 ± 13.1	80.8 ± 9.5	14.0 ± 4.2
(5, 6)	21.6 ± 4.6	71.0 ± 8.7	74.7 ± 9.2	34.2 ± 6.1	
(6, 7)	16.2 ± 4.0	30.6 ± 5.6	19.4 ± 4.7	8.9 ± 3.1	
(7, 8)	8.3 ± 2.8	13.0 ± 3.6	3.8 ± 1.9		

Table 5.22: $D^{*+} \rightarrow \pi^+ D^0 (K^- \pi^+)$ efficiency corrected yields.

5.5 Systematic uncertainties

There are several sources of systematic uncertainties. First, is the uncertainty related to the limited statistics of the MC samples that are used to extract generator, reconstruction and PID efficiencies. Second, is the systematic that comes from the difference between data and MC, in particular the difference in the shapes of the distributions for variables that are used in selections. The third contribution comes from the method of yield extraction, i.e. the systematic fit uncertainties in the data and the correction for the matching inefficiency in MC.

Some systematic uncertainties are correlated and are calculated per bin, i.e. systematic uncertainties on efficiencies. The uncorrelated systematic uncertainties affect the overall scale of the cross section, for example uncertainties on luminosity, branching fractions and the tracking efficiency.

Generator and reconstruction efficiency

The systematic uncertainties of the generator and reconstruction efficiencies are extracted from the number of D^0/D^{*+} in the corresponding MC samples. The relative error in the reconstruction efficiency varies from 1% to 10% depending on the bin. For the generator efficiency the relative errors are less than 1% in all relevant bins.

PID efficiency

There are two sources that contribute to the total systematic uncertainty on the PID efficiency. The first contribution is related to the limited statistic of the calibration data sample and is directly propagated from the uncertainties on the kaon and pion PID values (see Eq. (5.10)). The second contribution is related to the method that is used to determine the PID efficiency. This systematic is determined using MC by comparing the charm signal sample and the calibration sample.

The PID efficiency on the signal MC sample is given as

$$\varepsilon_i^{sig} = \frac{N_i^{pid}}{N_i}, \quad (5.12)$$

where N is the total number of truth matched candidates and N^{pid} is the number of truth matched candidates that have passed the PID requirements. Index i defines a particular (p_T, y) bin.

Alternatively, the PID efficiency ε_i^{clbr} of the MC calibration sample ($K_s^0 \rightarrow \pi^+\pi^-$ and $\phi \rightarrow K^+K^-$) is determined using in the same way as used for data, as described in Section 5.4.

Finally, the difference $\Delta\varepsilon_i = \varepsilon_i^{sig} - \varepsilon_i^{clbr}$ for each (p_T, y) bin is calculated. Due to a possible relative shift in $\log(\mathcal{L}_K/\mathcal{L}_\pi)$ value between data and MC (see Fig. 5.9) the $\Delta\varepsilon_i$ is determined by varying the PID cut over a range of ± 5 units around the nominal value. The maximum absolute difference was taken as an estimate for the systematic uncertainty. Due to the limited MC statistics the PID efficiency in

p_T (GeV/ c)	y				
	(2.0, 2.5)	(2.5, 3.0)	(3.0, 3.5)	(3.5, 4.0)	(4.0, 4.5)
(0, 1)	4.9	3.3	1.9	1.1	4.1
(1, 2)	3.3	3.0	1.5	1.8	3.5
(2, 3)	1.3	2.1	1.5	2.1	5.2
(3, 4)	4.7	2.2	1.3	5.2	5.2
(4, 5)	4.8	4.9	1.6	5.2	5.2
(5, 6)	5.2	5.2	5.2	5.2	5.2
(6, 7)	5.2	5.2	5.2	5.2	5.2
(7, 8)	5.2	5.2	5.2	5.2	5.2

Table 5.23: PID efficiency systematic uncertainties (in %).

some (p_T, y) bins cannot be determined. Consequently, for these bins the maximum found for all other bins is taken as a conservative estimate of systematic uncertainty.

Table 5.23 shows the systematic uncertainty for the PID efficiency in (p_T, y) bins obtained with this method.

The same systematic uncertainty is used for D^0 and D^{*+} as the kinematic of D^0 and D^0 produced in D^{*+} decay is similar (see Section 5.4).

Data/MC difference

The systematic uncertainties related to the difference between data and MC are estimated by comparing the efficiency corrected yields for statistically independent data sets. These data sets are defined by dividing the range of variables (kaon/pion χ_{IP}^2 , D^0 proper time $c\tau$, D^0 χ_{vtx}^2 and $\cos(\theta_\pi)$ in D^0 rest frame) into two non overlapping regions. For the proper time the division point is $200 \mu\text{m}$, which gives two data sets: $90 \mu\text{m} < c\tau < 200 \mu\text{m}$ and $200 \mu\text{m} < c\tau$. In the same way, the data sets for the χ_{IP}^2 , $\cos(\theta_\pi)$ and χ_{vtx}^2 are defined with the separation points at 25, 0.0 and 1, respectively. For each data set the reconstruction and PID efficiencies are calculated and subsequently used to calculate the efficiency corrected yields using the same p_T and rapidity binning as for the main result.

Figure 5.10 shows the pull distributions of efficiency corrected yields for different variables. The pull is defined as

$$Pull = \frac{N_{corr,2} - N_{corr,1}}{\sqrt{\sigma_{corr,2}^2 + \sigma_{corr,1}^2}}, \quad (5.13)$$

where N_{corr} and σ_{corr} are efficiency corrected yields and statistical uncertainties. Each entry in the pull distributions corresponds to one bin in (p_T, y) .

The pull distributions show no evidence of systematic effects for the χ_{IP}^2 and proper time variables, i.e. the kaon/pion χ_{IP}^2 and the life time acceptance are in good agreement between data and MC.

The pull of χ_{vtx}^2 shows a large shift. Further analysis shows that the χ_{vtx}^2 in data is overestimated compared to MC by a scale factor of about 1.25 which corresponds to a constant shift of about 0.1 of $\log_{10}(\chi_{vtx}^2)$ (see Fig. 5.11 (c)). This scale

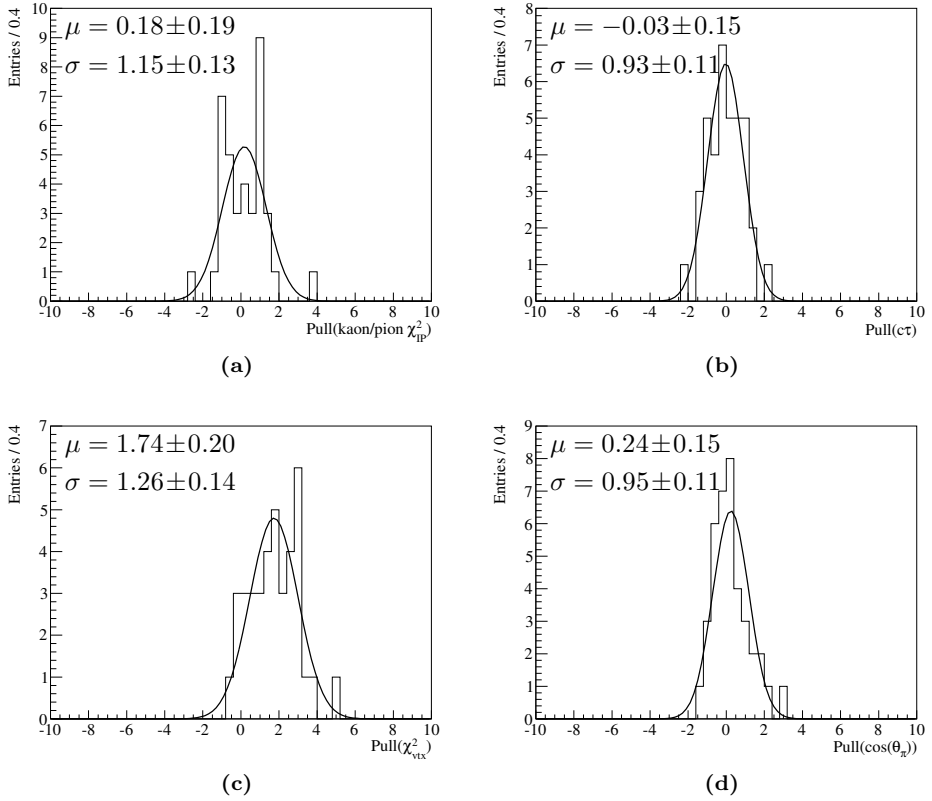


Figure 5.10: Pull distributions of efficiency corrected yields calculated between two independent data samples. The data samples are defined to have different ranges of kaon/pion χ^2_{IP} (a), D^0 proper time $c\tau$ (b), D^0 χ^2_{vtx} (c) and $\cos(\theta_\pi)$ in D^0 rest frame (d).

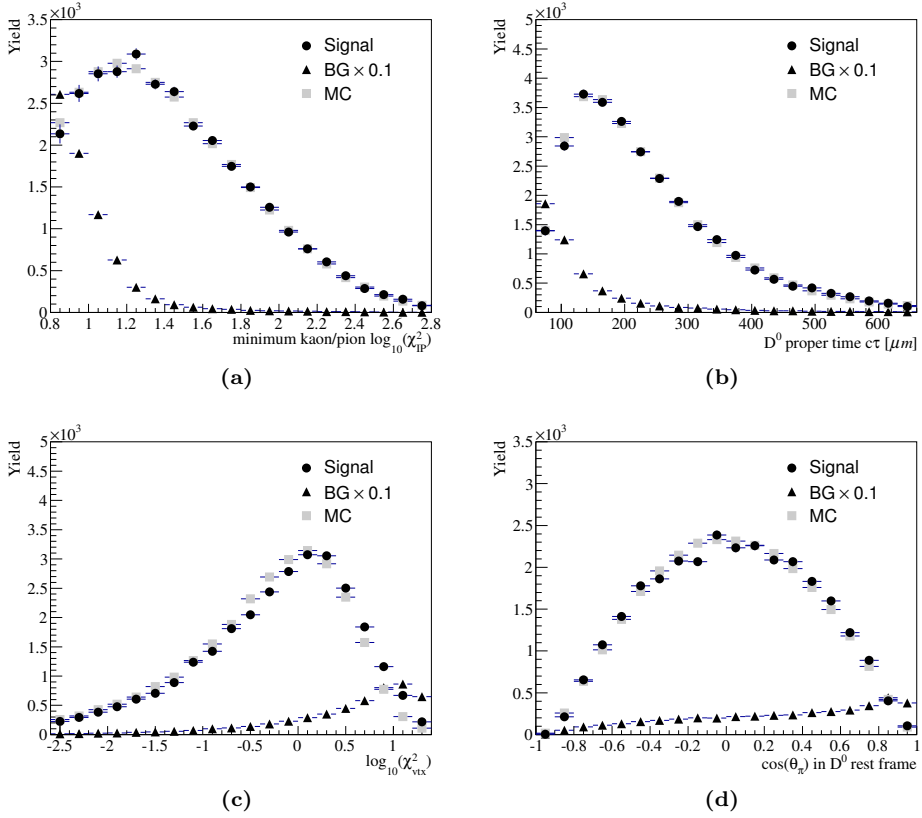


Figure 5.11: Data/MC comparison for kaon/pion χ^2_{IP} (a), D^0 proper time $c\tau$ (b), D^0 χ^2_{vtx} (c), and $\cos(\theta_\pi)$ in D^0 rest frame (d). The circles, squares and triangles correspond to the data background subtracted yield, the data background yield in mass windows $[1790; 1940]$ MeV/c^2 scaled by factor 0.1, and the number of truth matched candidates in MC, respectively.

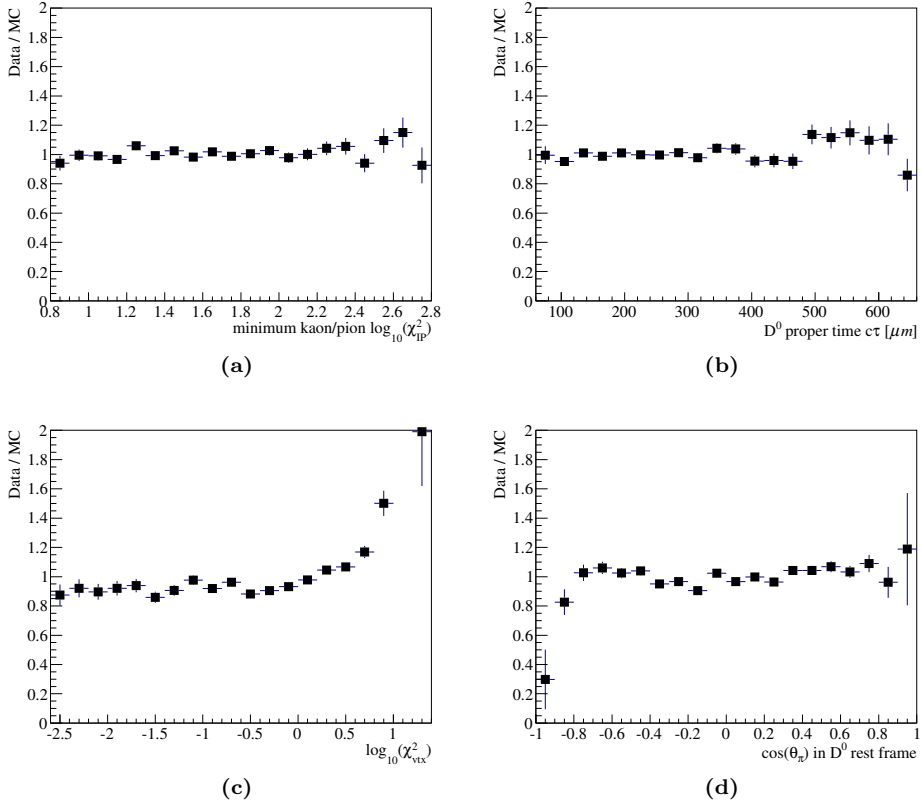


Figure 5.12: Ratio of yield in data to the number of MC truth matched candidates for kaon/pion χ^2_{IP} (a), D^0 proper time $c\tau$ (b), D^0 χ^2_{vtx} (c) and $\cos(\theta_\pi)$ in D^0 rest frame (d).

factor leads to an overestimation of the reconstruction efficiency. The corrected reconstruction efficiency can be extracted by applying the cut in MC on the χ_{vtx}^2 which is adjusted by a factor 1.25: $\chi^2 \cdot 1.25 < 9$. The difference in efficiency values between standard and corrected cut is 1.5%. This value is treated as the systematic error for the χ_{vtx}^2 cut.

Note that the data/MC shift in $D^0 \log_{10}(\chi_{vtx}^2)$ is approximately the same as the shift observed in $D^0 \log_{10}(\chi_{IP}^2)$ (see parameter $\mu_{ip/sig}$ in Fig. 5.5 for MC (a) and data (c)). One would not expect to observe these shifts, as there is no data/MC difference observed for kaon and pion χ_{IP}^2 . However, these variables effectively link together different parts of the detector, through the kaon and pion, and shifts can be due to residual misalignment of the detector, such as scale along x or z axis.

Figure 5.11 shows the distributions of signal yield for data and MC in bins of selection variables. The circles and triangles correspond to the signal and background in data obtained from the fit to the mass distribution with linear background and Gaussian signal shapes. The background is scaled by a factor of 0.1. The squares correspond to the number of MC truth matched events scaled to the data yield. The ratios of data to scaled MC are shown in Fig. 5.12.

The $\cos(\theta_\pi)$ pull distribution shows no evidence of systematic effect. However, the ratio for $\cos(\theta_\pi)$ (Fig. 5.12 (d)) shows a hint for a systematical deviation that can be related to the difference in track acceptance between data and MC for the pion produced in the backward direction in the center-of-mass of the D^{*+} meson ($\cos(\theta_\pi) \approx -1$). This difference affects only a small fraction of events, and the systematic uncertainty is negligible.

Fit systematic uncertainty

The systematic uncertainty of the fit was estimated by performing the fit with different PDFs describing $\log_{10}(\chi_{IP}^2)$, $m_{K\pi}$ and Δm shapes.

For the $\log_{10}(\chi_{IP}^2)$ the Bukin PDF [59] was used as a cross check. The Bukin PDF is defined for $x_1 < x < x_2$ as

$$P(x) \sim \exp \left(-\ln(2) \cdot \left[\frac{\ln \left(1 + 2\xi \sqrt{1+\xi^2} \frac{x-\mu}{\sigma \sqrt{2 \ln(2)}} \right)}{\ln \left(1 + 2\xi^2 - 2\xi \sqrt{1+\xi^2} \right)} \right]^2 \right) \quad (5.14)$$

and for $x < x_1$ or $x_2 < x$ as

$$P(x) \sim \exp \left(\frac{\xi \sqrt{1+\xi^2} (x-x_i) \sqrt{2 \ln(2)}}{\sigma \left(\sqrt{1+\xi^2} - \xi \right)^2 \ln \left(\sqrt{1+\xi^2} + \xi \right)} + \rho_i \left(\frac{x-x_i}{\mu-x_i} \right)^2 - \ln(2) \right), \quad (5.15)$$

where $\rho_i = \rho_1$ and $x_i = x_1$ when $x < x_1$, and $\rho_i = \rho_2$ and $x_i = x_2$ when $x > x_2$. x_1 and x_2 are defined as

$$x_{1,2} = \mu + \sigma \sqrt{2 \ln(2)} \left(\frac{\xi}{\sqrt{1+\xi^2}} \mp 1 \right). \quad (5.16)$$

The parameters μ and σ define the position and width of the core, ρ_1 and ρ_2 define the left and right exponential tails, and ξ is the asymmetry parameter.

Note that the number of parameter is the same as in AGE PDF (Eq. (5.6)). The difference in yields between the standard and the Bukin PDF does not show any sign of a systematic deviation.

For $m_{K\pi}$ and Δm a Gaussian PDF was used as a cross check. The Gaussian shape describes well the $m_{K\pi}$ and Δm distributions, but does not take into account a possible radiation tail on the left side of the mass distributions, which is clearly seen in the data. Possibly other sources than initial/final state radiation of the photon contribute to this tail. Consequently, the average difference in yields between these two PDFs is taken as systematic uncertainty. The difference is found to be the same for $m_{K\pi}$ and Δm , and amounts to 2.5%.

Number of primary vertexes

The number of reconstructed primary vertexes (N_{PV}) in the data is shown in Fig. 5.13. Most of the events contain only one reconstructed primary vertex, while about 10% of events have two or more vertexes.

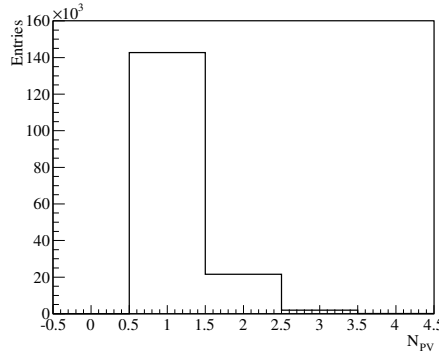


Figure 5.13: Number of reconstructed primary vertexes in a selected D^0 sample.

The reconstruction efficiency differs by up to 10% (relative) for events containing two collisions from those with one collision. Combined with the 10% fraction of events with two reconstructed primary vertexes in data, this gives an estimate of 1% systematic uncertainty.

Binning

As the cross section is measured in (p_T, y) bins, the difference between data and MC distributions of these variables can lead to an additional systematic effect, which is referred to as binning systematics. One can estimate the scale of this effect by performing the measurement in smaller size bins. However, due to the limited statistics this is not possible in two dimensions. Figure 5.14 shows the distribution of p_T and rapidity spectra for data and MC with bin sizes which are half of the standard size: 0.5 GeV/c in p_T , and 0.25 units in y .

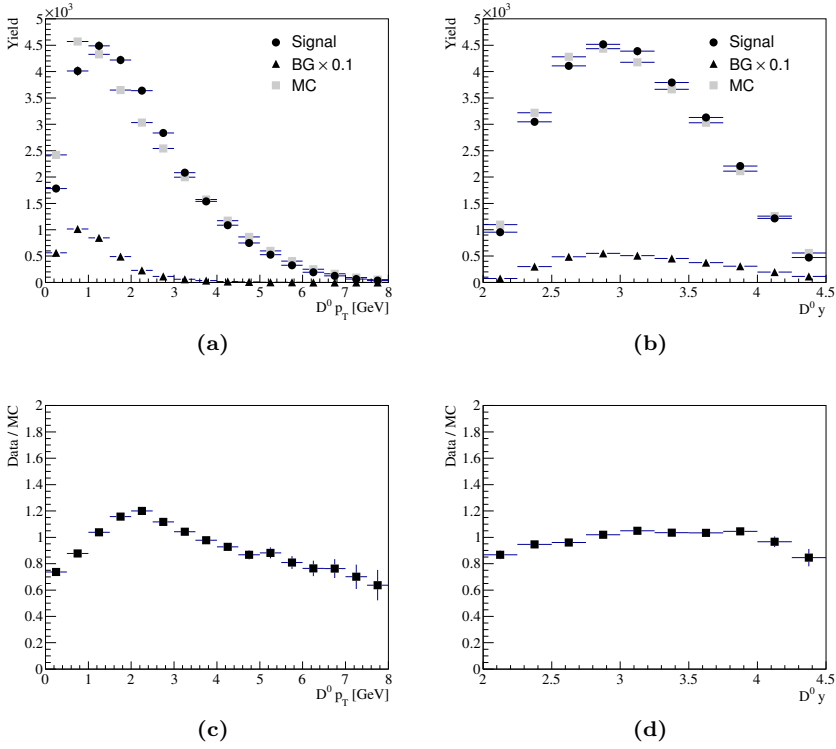


Figure 5.14: Data/MC comparison for $D^0 p_T$ (a) and y (b) spectra and corresponding ratios of data to MC (c,d).

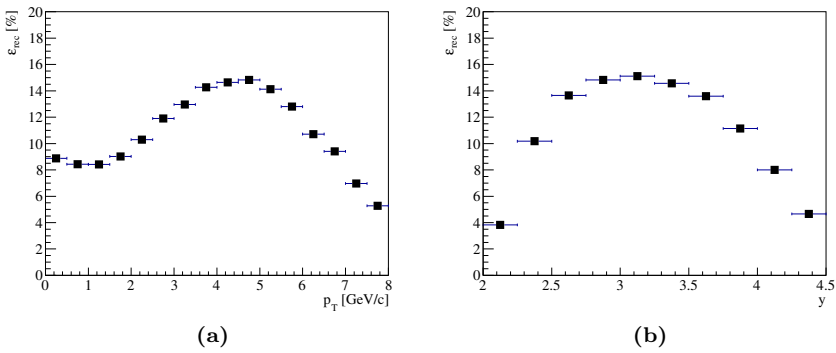


Figure 5.15: D^0 reconstruction efficiency as a function of p_T (a) and y (b).

The ratio of data to MC varies within nominal bins by up to $\pm 10\%$ ⁴. The variation within nominal bin is taken to be the half difference of smaller size bins. However, if the efficiency is constant within a bin, this variation should not introduce any systematic effect. Figure 5.15 shows the reconstruction efficiency as function of p_T (a) and rapidity (b) in half size bins. The efficiency within nominal bins varies by up to $\pm 10\%$, but this variation in turn will not introduce a systematic effect if the data to MC ratio is constant within a bin.

Consequently, the binning systematics can be estimated as the product of the difference between two neighboring bins in the ratio and efficiency. Taking the maximum variations gives an estimate of the systematic uncertainty of 1%.

Multiple candidates

During the selection one expects to find one reconstructed D^0 or D^{*+} candidate per event. Given the total average efficiency of less than 10% the probability to reconstruct a pair of D^0 or D^{*+} particles is less than 0.1%, consequently, other candidates in the same event usually correspond to background coming from the presence of ghost or clone tracks.

After all selections are applied the number of selected D^0 candidates in the full mass range is 145618, and the fraction of events with two or more candidates per events accounts for 1.4%. Selecting candidates with $D^0 \chi_{IP}^2 < 9$ and $|m_{K\pi} - 1865| < 25 \text{ MeV}/c^2$ gives about 90% of the signal events with only a small contribution of background. The fraction of events with two or more candidates with these selections is 0.2%. This number is a conservative estimate of the double counting systematic uncertainty for D^0 and is negligible.

In case of D^{*+} , the total number of selected candidates after all selections is 14544. The fraction of events with 2 or more candidates amounts to 17%. Selecting the signal D^{*+} region with $D^0 \chi_{IP}^2 < 9$, $|m_{K\pi} - 1865| < 25 \text{ MeV}/c^2$ and $|\Delta m - 145.5| < 2.5 \text{ MeV}/c^2$ leaves about 7.3% of events with 2 or more candidates. In MC the fraction of events with 2 or more candidates in the same kinematic region amounts to about 6.6%. The difference in these numbers, i.e. 1%, is taken as an estimate of the double counting systematic uncertainty for D^{*+} .

D^{*+} systematic uncertainties

The D^{*+} selections are based on the D^0 selections, and most systematic uncertainties are the same. The only additional systematic uncertainty comes from the selection of the $D^{*+} \chi_{vtx}^2$ and the correlated tracking systematic uncertainty of the pion from the D^{*+} . The behavior of the $D^{*+} \chi_{vtx}^2$ is similar to that of $D^0 \chi_{vtx}^2$, however, the scale factor is larger and gives systematic uncertainty of 2%.

Total systematic uncertainty

The systematic uncertainties are summarized in Tables 5.24 and 5.25. There are two types of systematic uncertainties. The first type of uncertainties are correlated

⁴.

Source of uncertainty	D^0	D^{*+}
Efficiency (per bin):		
- Generator efficiency	$0.1 \div 0.8$	$0.1 \div 1.4$
- Reconstruction efficiency	$0.9 \div 11.0$	$2.0 \div 12.1$
PID:		
- PID efficiency		< 1
- PID cut variation		$1 \div 5$
N_{PV}	1.0	1.0
Binning	1.0	1.0
Double counting	—	1.0
Quadratic sum	$1.6 \div 12.0$	$2.5 \div 13.2$

Table 5.24: Correlated systematic uncertainties (in %) on measured cross section of D^0 and D^{*+} . The uncertainties shown in combined cells are fully correlated between D^0 and D^{*+} (i.e. PID cut variation). “—” denotes negligible systematic uncertainty.

Source of uncertainty	D^0	D^{*+}
Data/MC:		
- K/π χ^2_{IP}		—
- D^0 proper time $c\tau$		—
- $\cos(\theta_\pi)$ in D^0 rest frame		—
- D^0 χ^2_{vtx}		1.5
- D^{*+} χ^2_{vtx}	n/a	2.0
Fit:		
- D^0 $\log_{10}(\chi^2_{IP})$ shape		—
- $m_{K\pi}$ shape		2.5
- Δm shape	n/a	2.5
Luminosity		3.6
$\mathcal{B}(D^0 \rightarrow K^- \pi^+)$		1.3
$\mathcal{B}(D^{*+} \rightarrow D^0 \pi^+)$	n/a	0.7
Tracking	6.0	10.0
Quadratic sum	7.7	11.5

Table 5.25: Uncorrelated (per bin) systematic uncertainties (in %) on measured cross section of D^0 and D^{*+} . The tracking systematic uncertainty for D^0 includes 3% error for kaon and pion tracks that are summed linearly giving 6% uncertainty. In the D^{*+} case the additional 4% is added linearly giving 10% uncertainty. “—” denotes negligible systematic uncertainty.

between different bins and affect the overall scale of the cross section. The second type are uncorrelated uncertainties that are applied to each bin individually.

The correlated systematic uncertainties include D^0 χ_{vtx}^2 and D^{*+} χ_{vtx}^2 , and fit uncertainties related to the $m_{K\pi}$ and Δm shapes. In addition there are correlated uncertainties on luminosity, branching fractions and tracking efficiency.

The bin-to-bin uncorrelated uncertainties include efficiency, binning and multiple candidates, and the number of primaries. The efficiency systematic uncertainties are calculated per bin with the main contribution coming from reconstruction efficiency and the PID systematic uncertainty that is estimated from the variation of the PID cut. The magnitudes of these uncertainties are limited by the signal MC samples statistics, however, they are still smaller than the statistical uncertainty on the yield in most bins.

In addition to these two types of uncertainty correlations, there are correlations present between the D^0 and D^{*+} uncertainties. Most of the D^0 systematic uncertainties are also applied to D^{*+} . In particular, the luminosity and tracking efficiency systematic uncertainties, that are the main sources for the bin-to-bin correlated uncertainty, are assumed to be fully correlated between D^0 and D^{*+} modes. The bin-to-bin uncorrelated uncertainties that are common to D^0 and D^{*+} include only the PID uncertainties due to the PID cut variation. These D^0/D^{*+} correlated uncertainties cancel in the ratio and will be discussed later.

In summary, the total uncorrelated uncertainty includes a bin-to-bin uncertainty that varies from 1.6% to 12% for D^0 and from 2.5% to 13.2% for D^{*+} , and an additional uncertainty of 1.4% and 1.7% for D^0 and D^{*+} , respectively. The total correlated systematic uncertainty amounts to 7.7% and 11.5% for D^0 and D^{*+} , respectively.

5.6 Cross section

The cross section is calculated in each (p_T, y) bin as

$$\sigma_i = \frac{N_i}{\varepsilon_i \cdot \mathcal{B} \cdot L}, \quad (5.17)$$

where N_i and ε_i are the yield and efficiency in (p_T, y) bin i . \mathcal{B} and L are the branching fraction and luminosity. The branching fractions [60] are $\mathcal{B}(D^0 \rightarrow K^-\pi^+) = (3.89 \pm 0.05)\%$ and $\mathcal{B}(D^{*+} \rightarrow \pi^+ D^0) = (67.7 \pm 0.5)\%$. The luminosity is $L = 5.01 \pm 0.18 \text{ nb}^{-1}$ (Eq. (5.1)).

Tables 5.26 and 5.27 show the differential production cross sections in bins of (p_T, y) calculated with Eq. (5.17) for prompt D^0 and D^{*+} mesons, respectively. The first error is statistical and the second is the uncorrelated systematic uncertainty. The correlated systematic uncertainty is not shown and amounts to 7.7% for D^0 and 11.5% for D^{*+} .

In all bins the correlated systematic uncertainty is less than the corresponding statistical uncertainty, with the exception of low (p_T, y) bins of the D^0 .

p_T (GeV/c)	y				
	(2.0, 2.5)	(2.5, 3.0)	(3.0, 3.5)	(3.5, 4.0)	(4.0, 4.5)
(0, 1)	113.90 \pm 5.46 \pm 6.83	96.40 \pm 3.49 \pm 4.50	90.67 \pm 3.66 \pm 3.47	80.25 \pm 4.18 \pm 2.87	57.34 \pm 5.37 \pm 3.16
(1, 2)	146.95 \pm 5.78 \pm 7.05	146.28 \pm 4.07 \pm 6.57	129.09 \pm 3.88 \pm 4.71	112.37 \pm 4.51 \pm 4.28	81.75 \pm 5.21 \pm 4.12
(2, 3)	85.81 \pm 3.18 \pm 3.20	82.03 \pm 2.10 \pm 3.24	68.55 \pm 1.90 \pm 2.52	58.27 \pm 2.02 \pm 2.36	40.02 \pm 2.57 \pm 2.58
(3, 4)	41.69 \pm 1.77 \pm 2.47	34.85 \pm 1.10 \pm 1.42	31.33 \pm 1.05 \pm 1.16	22.68 \pm 1.00 \pm 1.43	15.62 \pm 1.30 \pm 1.06
(4, 5)	18.59 \pm 0.98 \pm 1.14	16.08 \pm 0.67 \pm 0.98	14.35 \pm 0.66 \pm 0.57	9.88 \pm 0.62 \pm 0.64	5.72 \pm 0.87 \pm 0.45
(5, 6)	9.36 \pm 0.66 \pm 0.62	8.84 \pm 0.48 \pm 0.57	6.23 \pm 0.41 \pm 0.41	4.85 \pm 0.43 \pm 0.33	3.23 \pm 0.98 \pm 0.40
(6, 7)	4.92 \pm 0.51 \pm 0.36	4.31 \pm 0.38 \pm 0.30	3.00 \pm 0.33 \pm 0.22	2.33 \pm 0.34 \pm 0.19	
(7, 8)	2.35 \pm 0.42 \pm 0.20	2.41 \pm 0.36 \pm 0.20	1.25 \pm 0.27 \pm 0.11	1.14 \pm 0.34 \pm 0.14	

Table 5.26: Differential production cross section, $d\sigma/dp_T$, in $\mu\text{b}/(\text{GeV}/c)$, for prompt D^0 mesons in bins of (p_T, y) . The first and second errors are statistical and uncorrelated systematic uncertainties. The correlated systematic uncertainty amount to 7.7% and is not shown.

p_T (GeV/c)	y				
	(2.0, 2.5)	(2.5, 3.0)	(3.0, 3.5)	(3.5, 4.0)	(4.0, 4.5)
(0, 1)			26.66 \pm 5.26 \pm 1.84	36.91 \pm 6.06 \pm 2.49	46.47 \pm 12.74 \pm 4.91
(1, 2)		61.11 \pm 7.76 \pm 4.41	48.03 \pm 3.06 \pm 2.57	38.77 \pm 3.11 \pm 2.15	31.92 \pm 4.34 \pm 2.24
(2, 3)		30.21 \pm 2.57 \pm 1.78	24.65 \pm 1.53 \pm 1.32	23.93 \pm 1.76 \pm 1.36	18.62 \pm 2.38 \pm 1.51
(3, 4)	15.22 \pm 3.03 \pm 1.40	16.86 \pm 1.24 \pm 0.99	13.75 \pm 0.92 \pm 0.75	10.44 \pm 0.91 \pm 0.79	5.12 \pm 1.06 \pm 0.45
(4, 5)	9.82 \pm 1.59 \pm 0.86	6.23 \pm 0.65 \pm 0.47	6.18 \pm 0.57 \pm 0.36	4.53 \pm 0.54 \pm 0.36	3.46 \pm 1.03 \pm 0.39
(5, 6)	3.94 \pm 0.85 \pm 0.38	3.79 \pm 0.47 \pm 0.31	3.44 \pm 0.42 \pm 0.28	1.97 \pm 0.35 \pm 0.17	
(6, 7)	2.39 \pm 0.58 \pm 0.25	1.77 \pm 0.32 \pm 0.16	1.04 \pm 0.25 \pm 0.10	0.68 \pm 0.24 \pm 0.07	
(7, 8)	1.75 \pm 0.59 \pm 0.25	1.10 \pm 0.30 \pm 0.12	0.34 \pm 0.17 \pm 0.04		

Table 5.27: Differential production cross section, $d\sigma/dp_T$, in $\mu\text{b}/(\text{GeV}/c)$, for prompt D^{*+} mesons in bins of (p_T, y) . The first and second errors are statistical and uncorrelated systematic uncertainties. The correlated systematic uncertainties amounts to 11.5% and is not shown.

Comparison with theory

The theoretical predictions for the prompt D^0 and D^{*+} production cross section have been calculated using the Generalized Mass Variable Flavour Number Scheme (GMVFNS [61]) and the Fixed Order Next-to-Leading-Logarithm (FONLL [62]). These calculations provide the differential cross section as a function of p_T and y , and are described in Chapter 1.

Figures 5.16 and 5.17 show the D^0 and D^{*+} cross sections compared with the FONLL and GMVFNS predictions. The measured cross section is shown for different rapidity bins as function of p_T , scaled by a factor 10^{-m} , where m is the rapidity bin index (starting with zero).

The cross section for GMVFNS is shown for $p_T > 3 \text{ GeV}/c$ with the error band corresponding to the scale variation. Below $3 \text{ GeV}/c$ the scale uncertainties for GMVFNS amount to about 65%. The FONLL cross section is available in the full kinematic region.

Note that the FONLL calculation is systematically lower, while the GMVFNS calculation is systematically higher than the measured cross section. However, the results are consistent within the scale uncertainties.

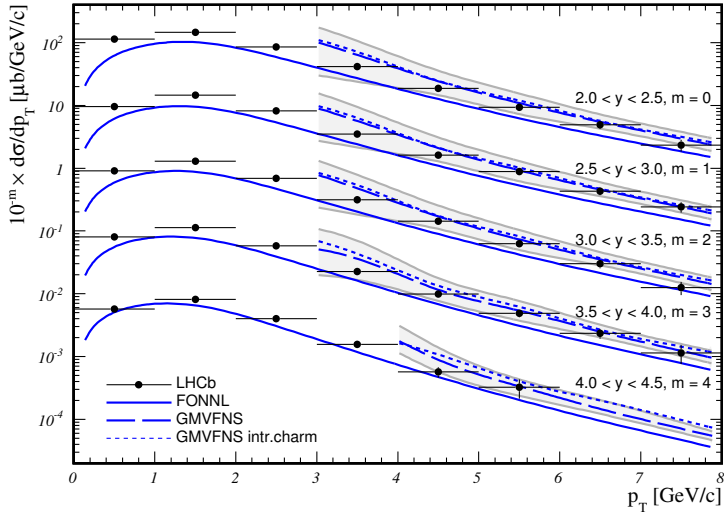


Figure 5.16: Measured D^0 cross section (points) compared with the FONLL (solid line) and GMVFNS (dashed line) theoretical predictions. The shaded area shows the theoretical uncertainty for the GMVFNS results. Dotted line shows GMVFNS prediction with intrinsic charm.

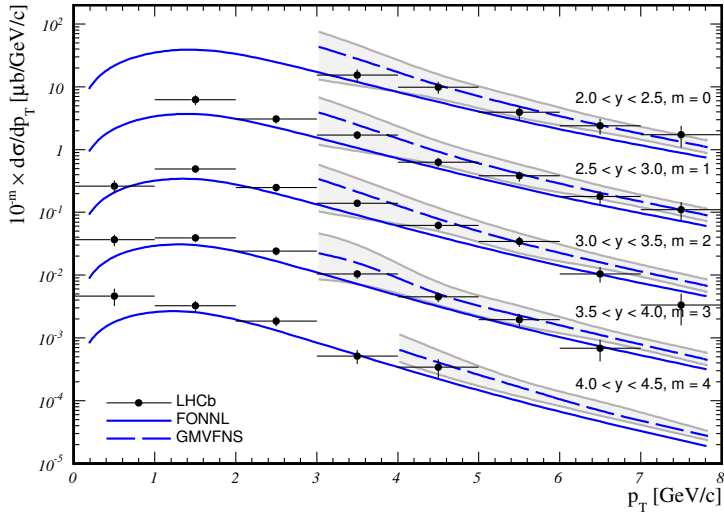


Figure 5.17: Measured D^{*+} cross section (points) compared with the FONLL (solid line) and GMVFNS (dashed line) theoretical predictions. The shaded area shows the theoretical uncertainty for the GMVFNS results.

Cross section ratio

Cross section ratios can be measured with much higher precision as it is free of many systematic uncertainties. All D^0 systematic uncertainties cancel in the ratio and the remaining systematic uncertainties include only the D^{*+} branching fraction, the tracking systematics of the pion from the D^{*+} , and generator and reconstruction efficiencies.

The ratios are calculated in (p_T, y) bins where both D^0 and D^{*+} cross sections are measured. The ratio errors are calculated assuming fully correlated statistical uncertainties:

$$\left(\frac{\sigma_R}{R}\right)^2 = \left(\frac{\sigma_0}{x_0}\right)^2 + \left(\frac{\sigma_*}{x_*}\right)^2 - 2f_c \frac{\bar{\sigma}_0 \bar{\sigma}_*}{x_0 x_*}, \quad (5.18)$$

where $R = x_0/x_*$ is the cross section ratio, $x_{\{0,*\}}$ are the D^0 and D^{*+} cross sections, $\sigma_{\{0,*\}}$ are the total uncertainties, and $\bar{\sigma}_{\{0,*\}}$ are the correlated statistical uncertainties. The f_c parameter is the correlation coefficient estimated as n_*/n_0 , where $n_{\{0,*\}}$ are the D^0 and D^{*+} raw yields.

Table 5.28 shows the cross section ratio in (p_T, y) bins with errors calculated using Eq. (5.18).

The average cross section ratio calculated over all non-empty bins is:

$$\frac{\sigma(D^0)}{\sigma(D^{*+})} = 2.32 \pm 0.06 \pm 0.12, \quad (5.19)$$

with the $\chi^2/N_{Dof} = 43/31$. The first uncertainty is calculated using Eq. (5.18) with bin-to-bin uncorrelated uncertainties (including statistical uncertainties), whereas second uncertainty is calculated using D^0/D^{*+} uncorrelated uncertainties (D^{*+} χ^2_{vtx} , Δm shape, D^{*+} branching fraction and pion tracking efficiency) and amounts to 5.2%. The average cross section ratio is compatible with the ratio of fragmentation fractions [60] of D^0 and D^{*+} :

$$\frac{f(c \rightarrow D^0)}{f(c \rightarrow D^{*+})} = 2.46 \pm 0.09, \quad (5.20)$$

p_T (GeV/ c)	y				
	(2.0, 2.5)	(2.5, 3.0)	(3.0, 3.5)	(3.5, 4.0)	(4.0, 4.5)
(0, 1)			3.42 ± 0.71	2.17 ± 0.39	1.23 ± 0.37
(1, 2)		2.39 ± 0.33	2.71 ± 0.20	2.90 ± 0.27	2.56 ± 0.40
(2, 3)		2.72 ± 0.25	2.80 ± 0.20	2.43 ± 0.21	2.15 ± 0.32
(3, 4)	2.74 ± 0.59	2.07 ± 0.18	2.30 ± 0.18	2.17 ± 0.23	3.05 ± 0.70
(4, 5)	1.89 ± 0.34	2.58 ± 0.30	2.32 ± 0.25	2.18 ± 0.31	1.65 ± 0.58
(5, 6)	2.38 ± 0.56	2.33 ± 0.33	1.81 ± 0.27	2.46 ± 0.51	
(6, 7)	2.06 ± 0.57	2.44 ± 0.52	2.89 ± 0.79	3.42 ± 1.34	
(7, 8)	1.34 ± 0.54	2.18 ± 0.72	3.73 ± 2.07		

Table 5.28: Ratio of D^0 to D^{*+} cross section. The errors show uncorrelated statistical and systematic uncertainty. The correlated systematic uncertainty includes 4% tracking uncertainty and is not shown.

where the uncertainty is calculated assuming no correlation between fragmentation fractions uncertainties.

Total cross section $\sigma(pp \rightarrow c\bar{c}X)$

The differential cross section, integrated over all non-empty bins for D^0 and D^{*+} , is:

- $\sigma(D^0) = (1655 \pm 16 \pm 14 \pm 127) \mu\text{b}$,
- $\sigma(D^{*+}) = (500 \pm 19 \pm 7 \pm 58) \mu\text{b}$,

where the first error is the statistical uncertainty, the second is the uncorrelated systematic uncertainty and the third is the correlated systematic uncertainty.

The extrapolation to the kinematic range of $0 < p_T < 8 \text{ GeV}/c$ and $2.0 < y < 4.5$ was performed using a PYTHIA simulation. The extrapolation factors are 1.002 for D^0 and 1.384 for D^{*+} . The extrapolation error is estimated as $(f_{ext} - 1)/\sqrt{12}$, where f_{ext} is the extrapolation factor. The total cross section in the full kinematic range is:

- $\sigma(D^0) = (1658 \pm 16 \pm 14 \pm 127 \pm 1) \mu\text{b}$,
- $\sigma(D^{*+}) = (693 \pm 26 \pm 10 \pm 80 \pm 56) \mu\text{b}$,

where the last errors corresponds to the uncertainty of the extrapolation factors.

The D^0 and D^{*+} cross sections can be translated to a $c\bar{c}$ production cross section as

$$\sigma(c\bar{c}, D) = \frac{\sigma(D)}{2 \cdot f(c \rightarrow D)}, \quad (5.21)$$

where D denotes charm meson and $f(c \rightarrow D)$ is the fragmentation fraction.

The fragmentation fractions [60] for D^0 and D^{*+} are $f(c \rightarrow D^0) = 0.564 \pm 0.015$ and $f(c \rightarrow D^{*+}) = 0.229 \pm 0.006$, respectively. Using Eq. (5.21) the total $c\bar{c}$ production cross sections calculated for D^0 and D^{*+} are:

- $\sigma(c\bar{c}, D^0) = (1470 \pm 14 \pm 12 \pm 113 \pm 1 \pm 39) \mu\text{b}$,
- $\sigma(c\bar{c}, D^{*+}) = (1512 \pm 58 \pm 22 \pm 174 \pm 121 \pm 40) \mu\text{b}$,

where the last errors correspond to the fragmentation fraction uncertainties. Within errors both values are consistent. However, the statistical uncertainties of D^0 and D^{*+} are partially correlated, as part of D^0 candidates are contained in D^{*+} sample.

The same extrapolation technique using a PYTHIA simulation can be used to obtain the total cross section in the 4π kinematic range. The extrapolation factor for $c\bar{c}$ production going from $0 < p_T < 8 \text{ GeV}/c$ and $2.0 < y < 4.5$ to the full kinematic range is $f_{ext} = 4.95$. The total $c\bar{c}$ cross section is, therefore:

- $\sigma(c\bar{c}, D^0) = (7276 \pm 71 \pm 59 \pm 558 \pm 4 \pm 194) \mu\text{b}$,
- $\sigma(c\bar{c}, D^{*+}) = (7489 \pm 285 \pm 109 \pm 863 \pm 600 \pm 196) \mu\text{b}$,

where no additional systematic uncertainty is assigned for extrapolation factor.

Comparison with the total $b\bar{b}$ cross section [63] shows that $\sigma(pp \rightarrow c\bar{c})$ is about 20 times larger than $\sigma(pp \rightarrow b\bar{b})$. This means that with the inelastic cross section $\sigma_{in} \approx 70 \text{ mb}$ at $\sqrt{s} = 7 \text{ TeV}$ about one $c\bar{c}$ pair is produced in every 10 collisions.

5.7 D^{*+} polarization

In this analysis it is assumed that the D^{*+} is produced with zero polarization. A non-zero polarization can affect the reconstruction efficiency leading to systematic deviations in the measured cross section. Also, knowledge of the polarization of the D^{*+} produced in the pp collisions is important for better understanding of the production mechanism.

The polarization is determined in bins of p_T , integrating over the full rapidity range $2.0 < y < 4.5$. Similar to the fit procedure, described in Section 5.3, the large and small bins were defined in $(p_T, \cos(\theta_\pi^*))$ space, where θ_π^* is the angle between the momentum directions of the slow pion and D^{*+} in the rest frame of the D^{*+} . The large bins have $2 \text{ GeV}/c$ width in p_T and cover the full range in $\cos(\theta_\pi^*)$. The small bins have $2 \text{ GeV}/c$ width in p_T , the same as large bins, and 0.25 units in $\cos(\theta_\pi^*)$, giving 8 bins in the full $\cos(\theta_\pi^*)$ range. A simultaneous fit was performed in each large bin. The parameters $n_{\{sig,bg,D^0\}}$, μ_m , σ_m and $\sigma_{\Delta m}$ were determined

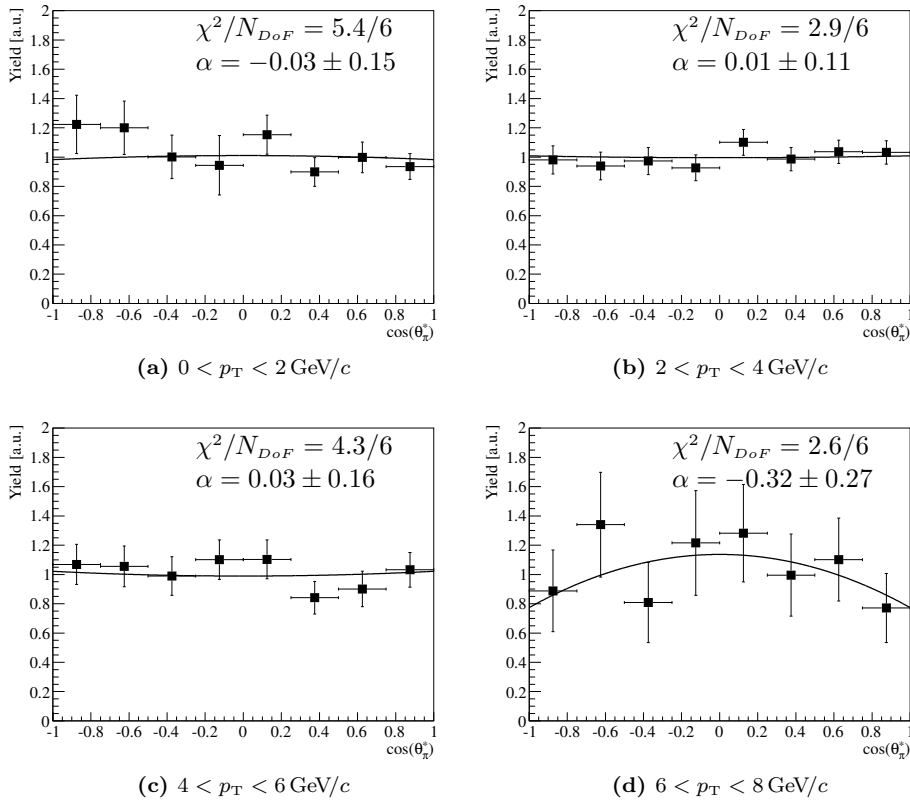


Figure 5.18: Fit to $\cos(\theta_\pi^*)$ in different p_T bins of D^{*+} . The fit is performed with the function $1 + \alpha \cdot \cos^2(\theta_\pi^*)$, where α describes the D^{*+} polarization. The overall normalization is arbitrary.

separately per small bin, with all other parameters shared between small bins.

As the overall scale factor is not important for polarization, the efficiency corrected yields were calculated as a ratio of prompt D^{*+} yields, determined from the fit to data, to the MC yields. This allows to automatically take into account the generator and reconstruction efficiency. The yields are not corrected for the PID efficiency, as it is found to be independent of $\cos(\theta_\pi^*)$; the bin-to-bin variations are smaller than 0.5%. In addition, no PID systematics is assigned to the corrected yields.

Figure 5.18 shows the ratio as a function of $\cos(\theta_\pi^*)$ for different p_T bins fitted with a function $1 + \alpha \cdot \cos^2(\theta_\pi^*)$, where α describes the polarization.

The result of the fit in each p_T bin is consistent with no polarization.

5.8 Summary

The charm production cross section of D^0 and D^{*+} has been measured with an integrated luminosity of 15 nb^{-1} collected in May 2010 at low pileup conditions with the LHCb detector at $\sqrt{s} = 7 \text{ TeV}$. A comparison with theoretical predictions is made, however, the theoretical uncertainties are significantly larger than the measurement uncertainties. The cross section is measured in bins of transverse momentum p_T and rapidity y ; 8 bins of width $1 \text{ GeV}/c$ in the range $0 < p_T < 8 \text{ GeV}/c$, and 5 bins of width 0.5 units in the range $2.0 < y < 4.5$. Also the total cross section in the full kinematic region is determined.

The use of the full integrated luminosity collected with LHCb can allow to improve the precision and extend the kinematic region to higher p_T . However, due to the strong rate limits on the micro-bias trigger, the effective increase in available data is smaller than the increase in luminosity. In addition, due to higher pileup, one has to estimate the efficiency for a different number of primary vertexes. On the other hand, the large available data sample allows to reduce the systematic uncertainties on the PID and tracking, which are the dominant sources of systematic uncertainties.

For the high p_T region, where the production rate is small, the cross section can also be measured using the hadron triggered events. This would allow to significantly increase the available data sample, as the efficiency is high, but requires good understanding of the hadron trigger efficiency.

To implement a better separation of prompt and secondary components, it is possible to perform a separate selection of inclusive $B \rightarrow D\mu\nu X$ decays, where X is “anything”. These decays are the main contribution to secondary production and can allow to extract the precise shape of χ_{IP}^2 for the secondary fraction of D mesons.

Appendix A

TR-relation PDF

The TR-relation PDF describes the two-dimensional distribution of measured drift time versus reconstructed distance. Figure A.1 shows the schematic view of a particle passing the straw at a distance r_0 from the wire and producing the ionization cluster closest to the wire at distance d_0 . Assuming that both measured drift time t and distance from the wire to the reconstructed track r depend only on the distance r_0 the TR-relation PDF can be factorized:

$$P(r, t) = \int_0^{r_m} \varepsilon(r_0) \cdot G_r(r|r_0) \cdot G_t(t|r_0) dr_0, \quad (\text{A.1})$$

where $\varepsilon(r_0)$ is the cell efficiency, and $G(r|r_0)$ and $G_t(t|r_0)$ are drift time and distance PDFs, respectively. The distribution of impact parameters of the incident particles over the straw diameter is assumed to be uniform and is integrated out in the calibration procedure.

The cell efficiency $\varepsilon(r_0)$ describes the probability for a particle to produce at least one ionization cluster that is consequently registered (see Section 3.2):

$$\varepsilon(r_0) = 1 - \exp\left(-\frac{2}{\lambda_{eff}} \cdot \sqrt{r_m^2 - r_0^2}\right), \quad (\text{A.2})$$

where λ_{eff} is an effective ionization length.

Assuming Gaussian uncertainties and that the ionization cluster is produced close to the POCA ($d_0 \approx r_0$, see Fig. A.1) the drift time and distance PDFs can be written as

$$G_r(r|r_0) = \frac{1}{\sqrt{2\pi}\sigma_r} \exp\left(-\frac{(r - r_0)^2}{2\sigma_r^2}\right) \quad (\text{A.3})$$

and

$$G_t(t|r_0) = \frac{1}{\sqrt{2\pi}\sigma_t(r_0)} \exp\left(-\frac{(t - t(r_0))^2}{2\sigma_t(r_0)^2}\right), \quad (\text{A.4})$$

where σ_r is an estimate of the distance uncertainty (provided by the track fit) and $\sigma_t(r_0)$ is the drift time resolution. The function $t(r_0)$ is the distance-to-time relation or TR-relation.

The drift time resolution is assumed to have a linear dependence:

$$\sigma_t(r) = \sigma_t^{(0)} \cdot \left(1 - \frac{r}{r_m}\right) + \sigma_t^{(m)} \cdot \frac{r}{r_m}, \quad (\text{A.5})$$

where $\sigma_t^{(0)}$ is the resolution at distance $r = 0$ and $\sigma_t^{(m)}$ is the resolution at distance $r = r_m$.

The TR-relation has the form of a second order polynomial:

$$t(r) = t_m \cdot \frac{r}{r_m} - 4t_c \cdot \frac{r}{r_m} \left(1 - \frac{r}{r_m}\right), \quad (\text{A.6})$$

where t_m is the maximum drift time at distance $r = r_m$ and t_c describes the curvature of the distance-to-time relation. The schematic view of the TR-relation illustrating the meaning of parameters is shown in Fig. A.2.

Secondary hits

The measured drift time corresponds to the rising edge of the signal that is read-out. Consequently, for two particles passing the same straw the measured drift time will correspond to the particle (ionization) that is closest to the wire. Note that the reconstructed distances correspond to the signal particles (reconstructed tracks), as any secondary hits are considered to be random and their contribution is reduced by usage of track quality cuts, for example the track fit χ^2 .

For the particle passing the straw at distance r_0 and for a secondary (background) particle passing the straw at distance r'_0 there are four cases to be considered:

- The secondary particle did not produce an ionization cluster and the drift

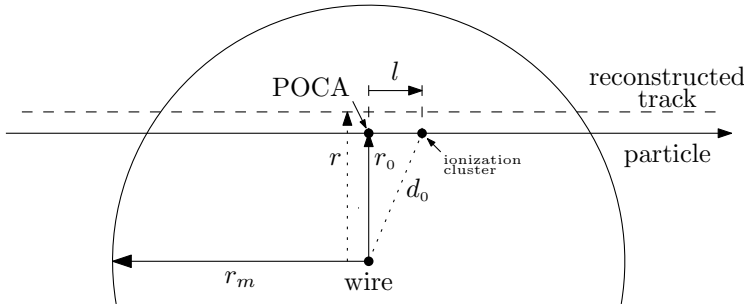


Figure A.1: Schematic view of a particle passing the straw at distance r_0 from the wire. POCA denotes the point of closest approach to the wire on the particle trajectory. The distance along the particle trajectory from the POCA to the closest ionization cluster is l . The inner radius of the straw is r_m .

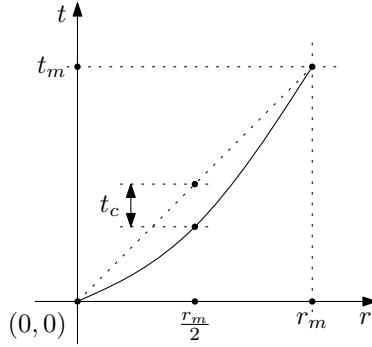


Figure A.2: Illustration of time-to-distance relation. TR-relation is described with second order polynomial. The t_m is the maximum drift time and t_c describes the curvature.

time corresponding to the signal particle is measured:

$$P'_{10}(t|r_0) = \int_0^{r_m} \varepsilon(r_0) \cdot (1 - \varepsilon(r'_0)) \cdot G_t(t|r_0) dr'_0, \quad (\text{A.7})$$

where $\varepsilon'(r_0)$ is the cell efficiency for secondary particle;

- The signal particle did not produce an ionization cluster and the drift time corresponding to the secondary particle is measured:

$$P'_{01}(t|r_0) = \int_0^{r_m} (1 - \varepsilon(r_0)) \cdot \varepsilon(r'_0) \cdot G_t(t|r'_0) dr'_0; \quad (\text{A.8})$$

- Both particles produced ionization clusters and the secondary particle is closer to the wire ($r'_0 < r_0$):

$$P'_{>}(t|r_0) = \int_0^{r_0} \varepsilon(r_0) \cdot \varepsilon(r'_0) \cdot G_t(t|r'_0) dr'_0; \quad (\text{A.9})$$

- Both particles produced ionization clusters and the signal particle is closer to the wire ($r'_0 > r_0$):

$$P'_{<}(t|r_0) = \int_{r_0}^{r_m} \varepsilon(r_0) \cdot \varepsilon(r'_0) \cdot G_t(t|r'_0) dr'_0; \quad (\text{A.10})$$

The combination of these contributions gives the correction to TR PDF:

$$\Delta P(r, t) = \alpha \int_0^{r_m} G_r(r|r_0) \cdot (P'_{10} + P'_{01} + P'_{<} + P'_{>}) dr_0, \quad (\text{A.11})$$

where α is the fraction of secondary hits. Both r_0 and r'_0 are assumed to have uniform distribution and are integrated out.

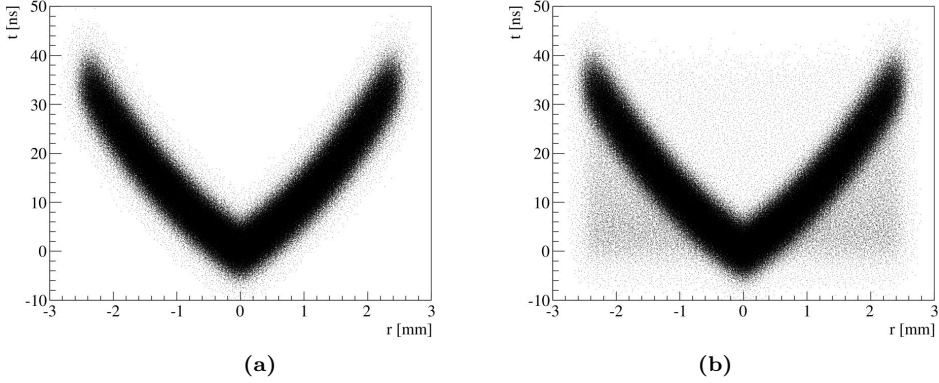


Figure A.3: Simulated distribution of drift time and distance with no background hits (a) and with background hits (b).

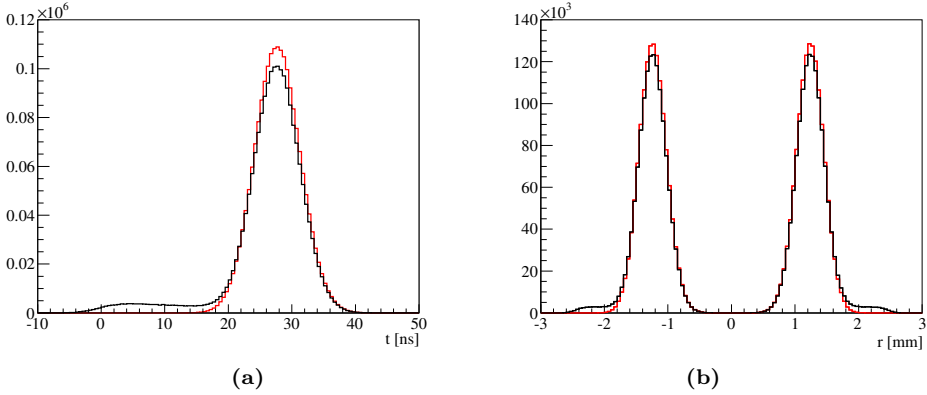


Figure A.4: (a) Drift time projections for $|r - 2.0| < 50 \mu\text{m}$ and (b) distance projections for $|t - 15| < 0.5 \text{ ns}$. The black line corresponds to TR distribution with background hits and the red line with no background hits.

Figure A.3 (left) shows the two-dimensional distributions of hits simulated with the TR-relation PDF given by Eq. (A.1) and Eq. (A.11). Figure A.4 shows for both PDFs the projections on drift time and reconstructed distance in a certain range of distance and time respectively. Note that the background hits are visible mainly below the main distribution ($t' < t$).

Ionization length

It has been assumed above that the ionization clusters are produced at the POCA. This is a good approximation at distances $r_0 \gtrsim \lambda_{eff}$. However, at small distances

to the wire, due to the distribution of clusters along the particle trajectory, the distance to closest ionization cluster can be significantly larger than r_0 .

The distance l to the closest ionization cluster from the POCA along the particle trajectory is described with an exponential PDF:

$$P_l(l) = \frac{2}{\lambda_{eff}} \exp\left(-\frac{2}{\lambda_{eff}l}\right), \quad (\text{A.12})$$

where the factor 2 comes from the fact that the ionization cluster can be located on both sides from the POCA.

Following Eq. (A.12) the drift time PDF can be rewritten as:

$$G_t(t|r_0) = \int_0^{\sqrt{r_m^2 - r_0^2}} \frac{1}{\sqrt{2\pi}\sigma_t(d_0)} \exp\left(-\frac{(t - t(d_0))^2}{2\sigma_t(d_0)^2}\right) P_l(l) dl, \quad (\text{A.13})$$

where $d_0 = \sqrt{r_0^2 + l^2}$ is the distance to the ionization cluster.

Note that the introduction of such a drift time PDF into the TR PDF significantly complicates the calculation, leading to multidimensional integrals. Consequently, this extension of TR PDF is used only to extract the effective ionization length, as shown in Section 4.5. In addition, at small distance the average measured drift time becomes larger, effectively introducing a shift along the t -axis. This leads to the fact that the fit performed with the simplified PDF ($d_0 = r_0$) does not describe the actual (physical) time-to-distance relation.

Appendix B

D^0 and D^{*+} fits

Figures B.1 to B.9 show the D^0 fits in large bins. In each figure (a) shows the prompt (circles) and secondary (open squares) $D^0 \log_{10}(\chi^2_{IP})$ in MC, (b) shows the $m_{K\pi}$ in data with the overlaid fit projection, (c) and (d) show the $D^0 \log_{10}(\chi^2_{IP})$ in data with the overlaid fit projection in signal ($|m_{K\pi} - 1865| < 30 \text{ MeV}/c^2$) and background ($|m_{K\pi} - 1865| > 30 \text{ MeV}/c^2$) regions, respectively.

Figures B.10 to B.15 shows the D^{*+} fits in large bins. In each figure (a) shows the prompt (circles) and secondary (open squares) $D^0 \log_{10}(\chi^2_{IP})$ in MC, (b) shows the $m_{K\pi}$ in data with the overlaid fit projection, (c) and (d) show the $D^0 \log_{10}(\chi^2_{IP})$ in data with the overlaid fit projection in signal ($|m_{K\pi} - 1865| < 30 \text{ MeV}/c^2$ and $|\Delta m - 145.5| < 3.0 \text{ MeV}/c^2$) and background ($|m_{K\pi} - 1865| > 30 \text{ MeV}/c^2$) regions, respectively, (e) shows the Δm in data with the overlaid fit projection

In each figure the dashed line, shaded area and dotted line show the prompt, secondary and background fit components, respectively. The fit parameters for each projection are shown in corresponding figure. For parameters that are defined per small bin the range of parameter values are shown. The background and secondary yields are not shown. The signal yields are shown in Tables 5.4 and 5.5.

For detailed description of fit procedure see Section 5.3.

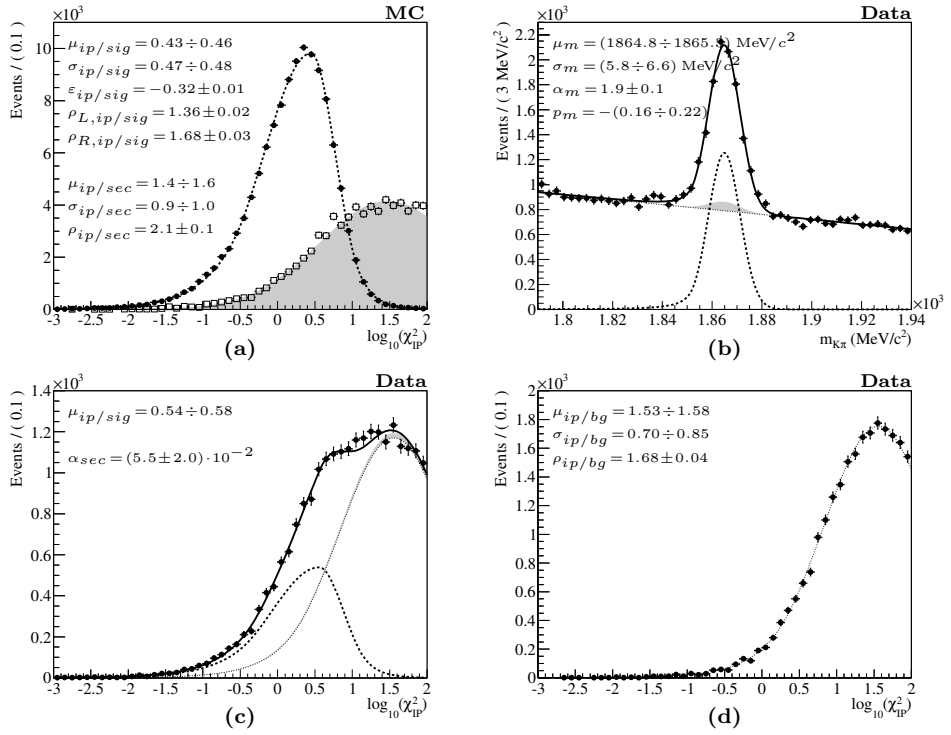


Figure B.1: Fit to the D^0 data for $0 < p_T < 2 \text{ GeV}/c$ and $2.0 < y < 3.0$.

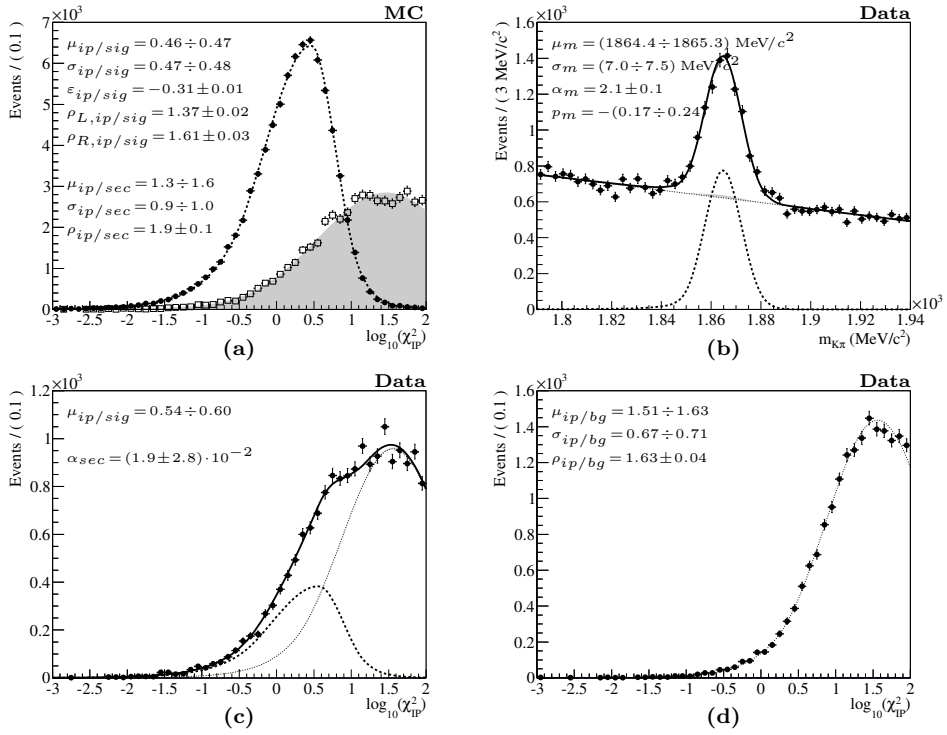


Figure B.2: Fit to the D^0 data for $0 < p_T < 2 \text{ GeV}/c$ and $3.0 < y < 3.5$.

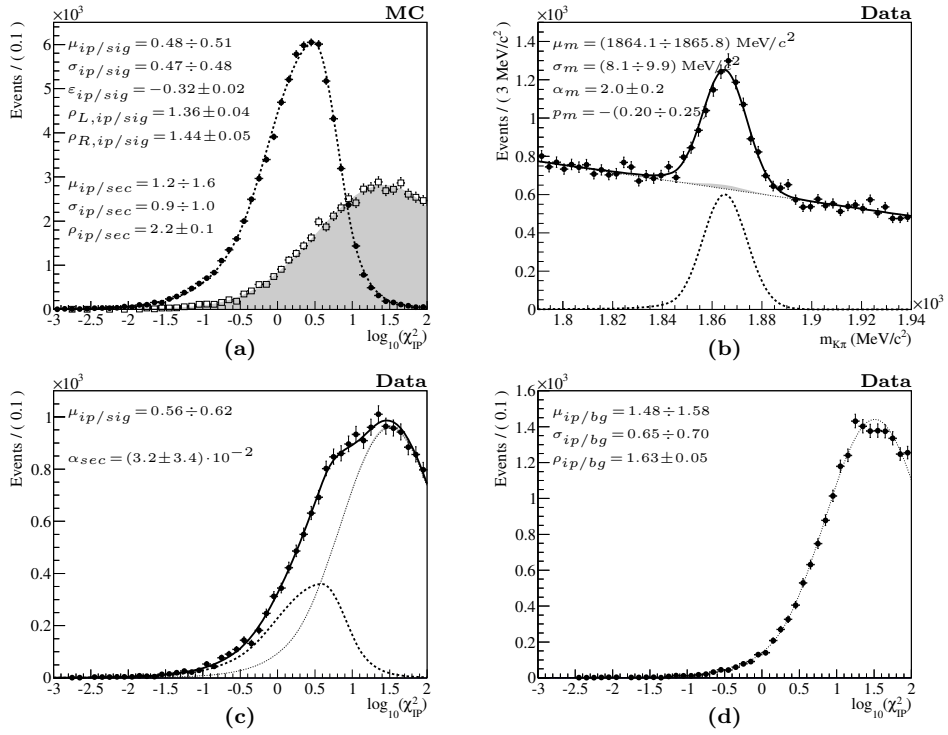


Figure B.3: Fit to the D^0 data for $0 < p_T < 2 \text{ GeV}/c$ and $3.5 < y < 4.5$.

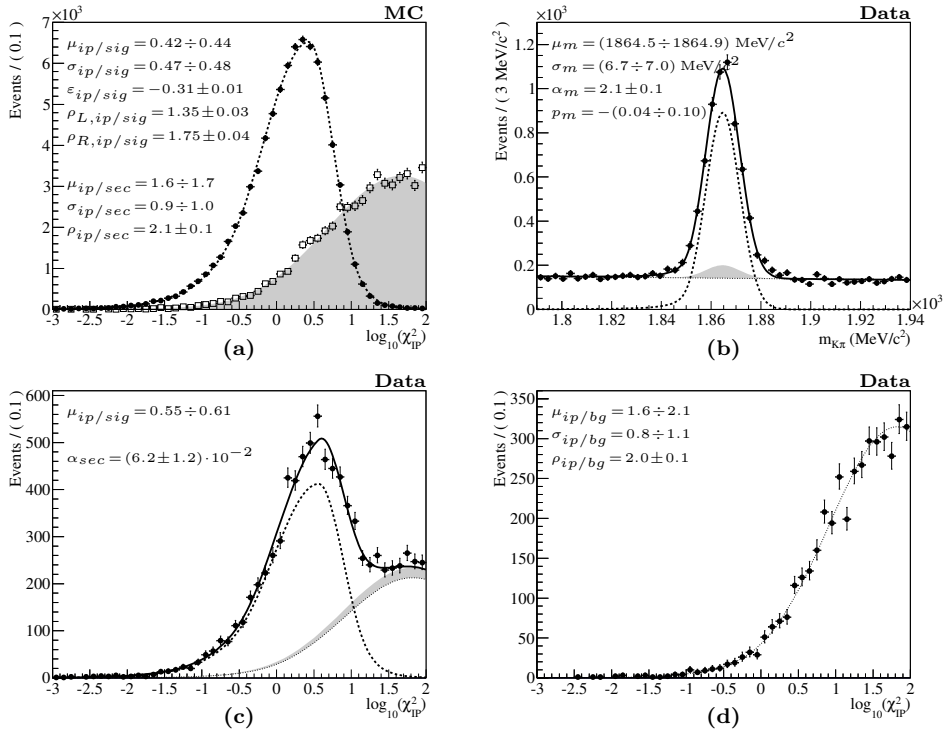


Figure B.4: Fit to the D^0 data for $2 < p_T < 4 \text{ GeV}/c$ and $2.0 < y < 3.0$.

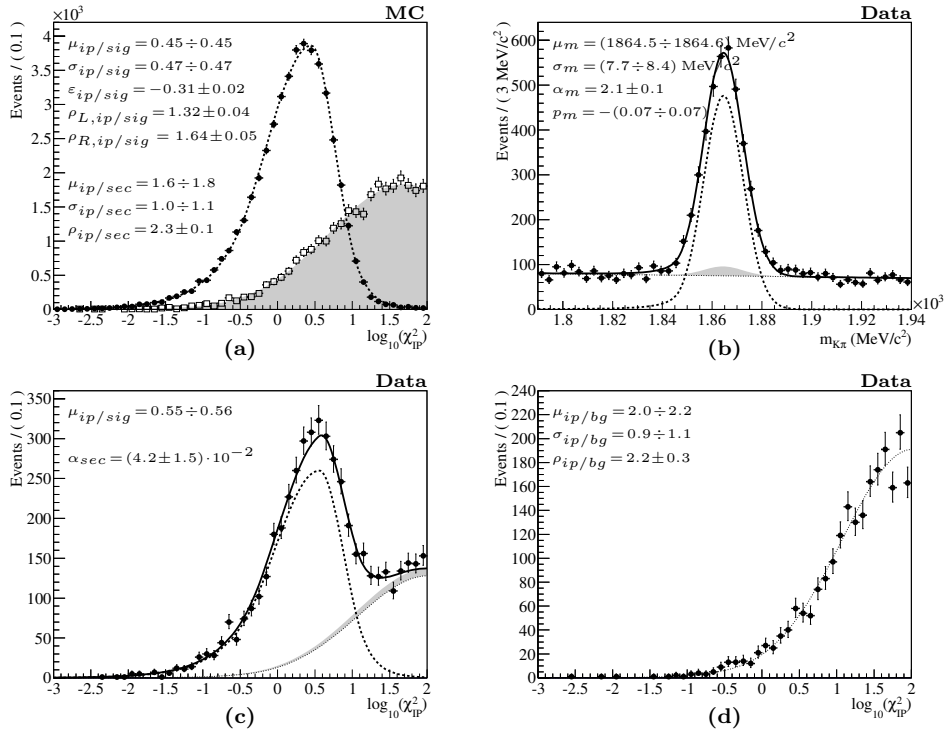


Figure B.5: Fit to the D^0 data for $2 < p_T < 4 \text{ GeV}/c$ and $3.0 < y < 3.5$.

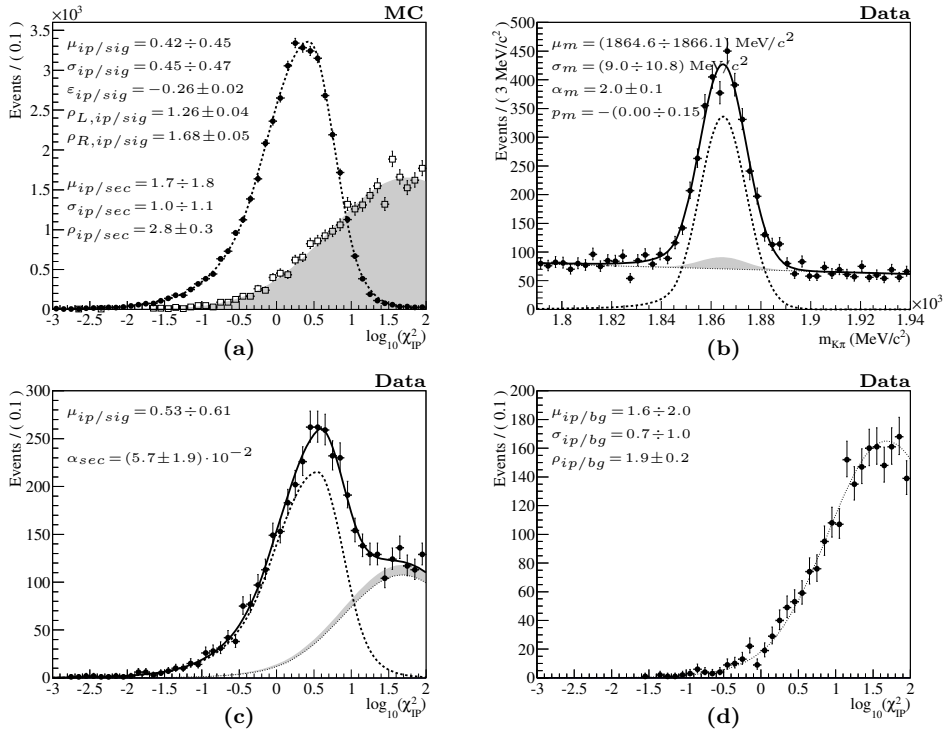


Figure B.6: Fit to the D^0 data for $2 < p_T < 4 \text{ GeV}/c$ and $3.5 < y < 4.5$.

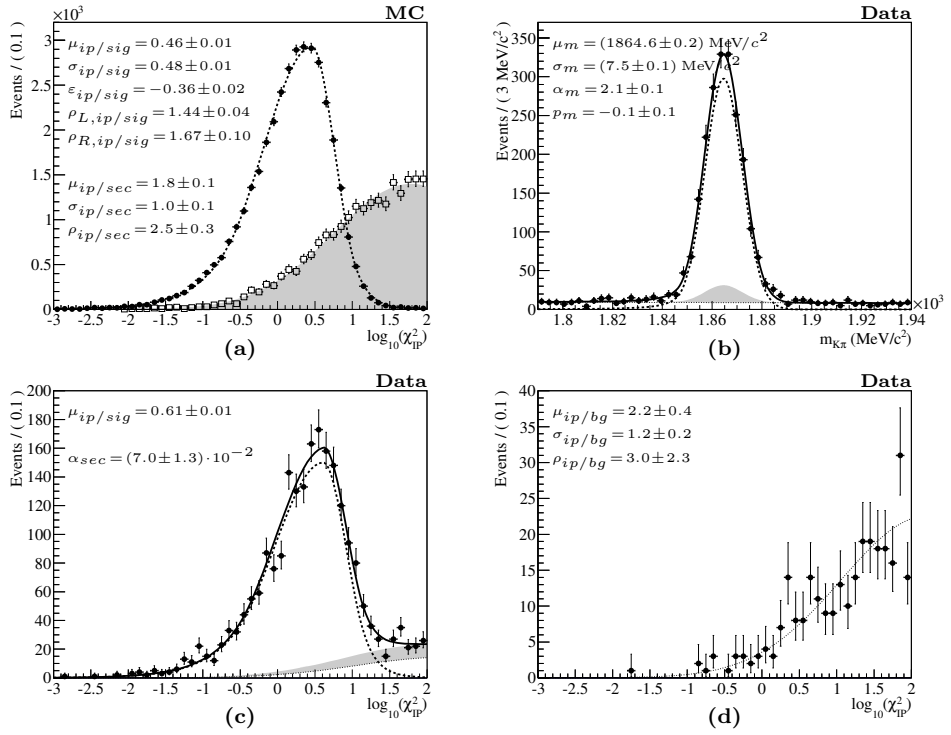


Figure B.7: Fit to the D^0 data for $4 < p_T < 8 \text{ GeV}/c$ and $2.0 < y < 3.0$.

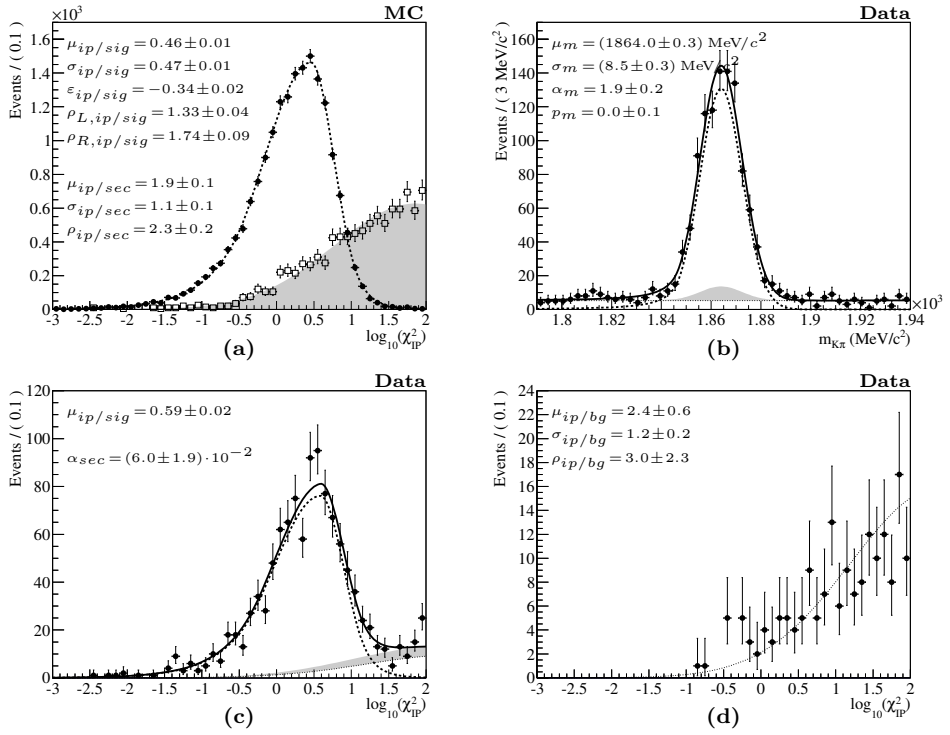


Figure B.8: Fit to the D^0 data for $4 < p_T < 8 \text{ GeV}/c$ and $3.0 < y < 3.5$.

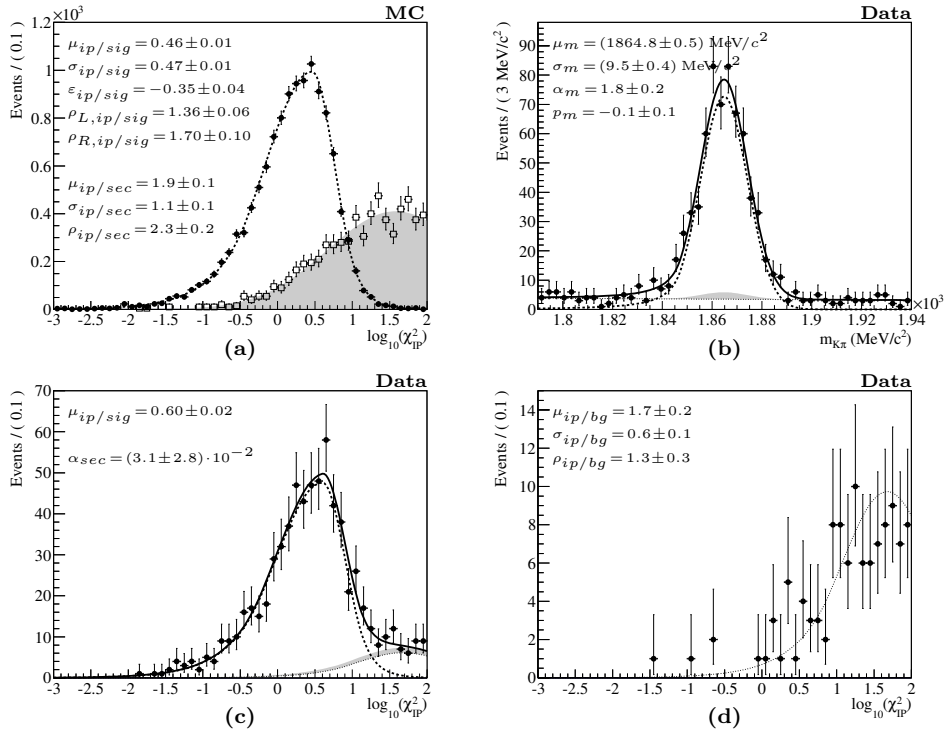


Figure B.9: Fit to the D^0 data for $4 < p_T < 8 \text{ GeV}/c$ and $3.5 < y < 4.5$.

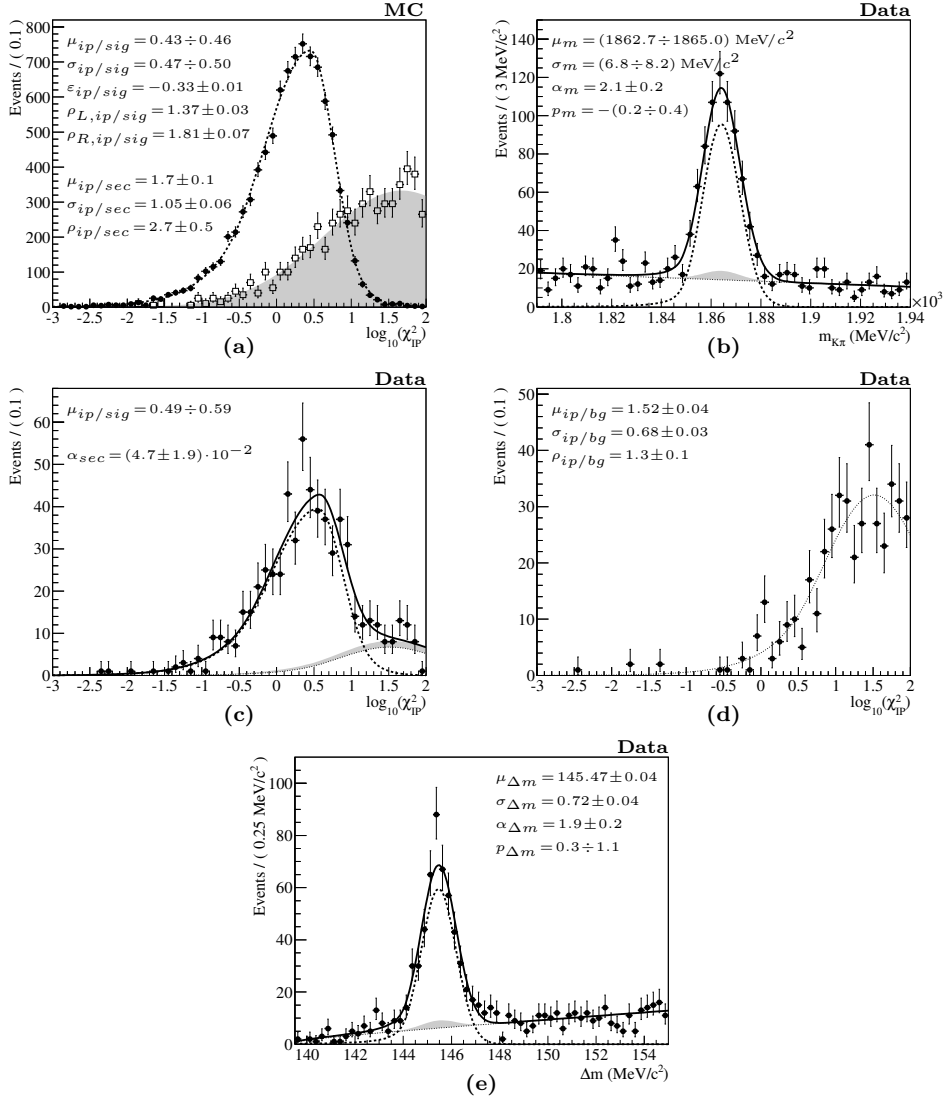


Figure B.10: Fit to the D^{*+} data for $0 < p_T < 4 \text{ GeV}/c$ and $2.0 < y < 3.0$.

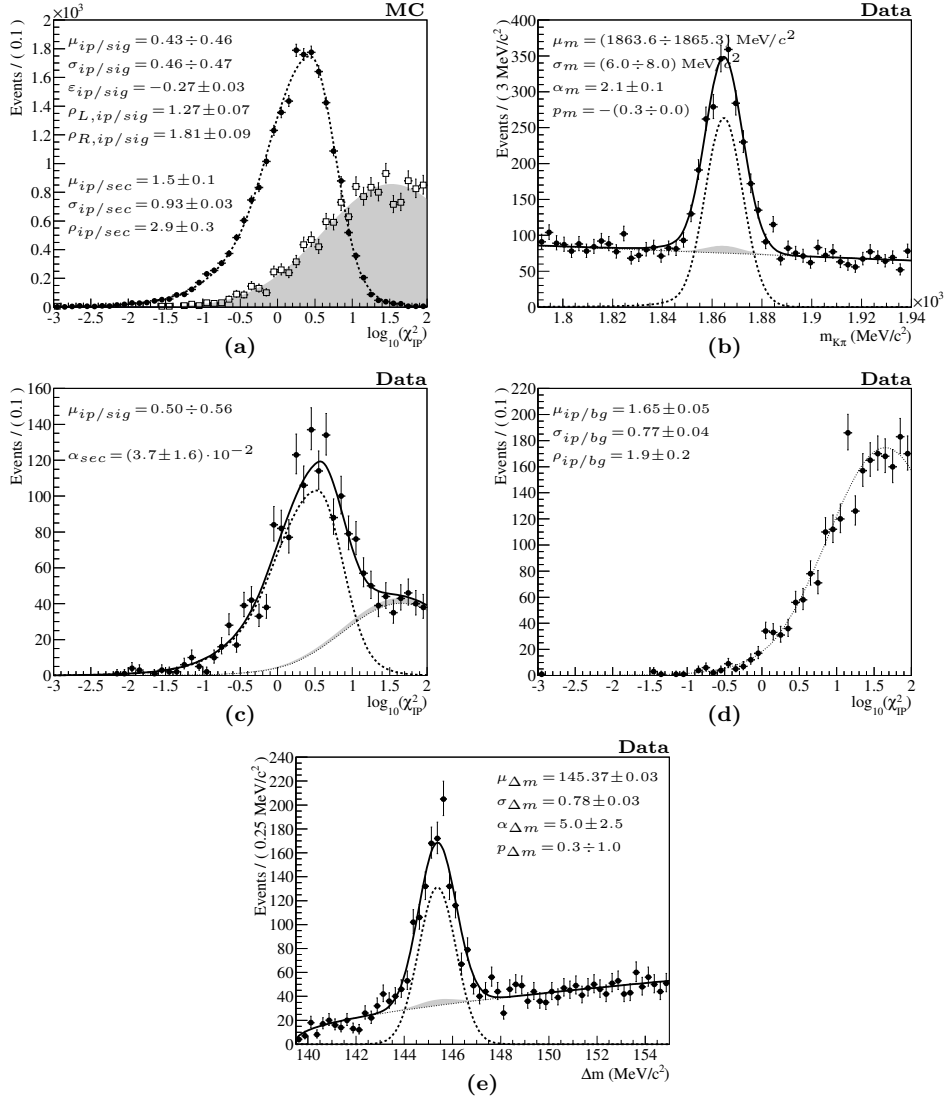


Figure B.11: Fit to the D^{*+} data for $0 < p_T < 4 \text{ GeV}/c$ and $3.0 < y < 3.5$.

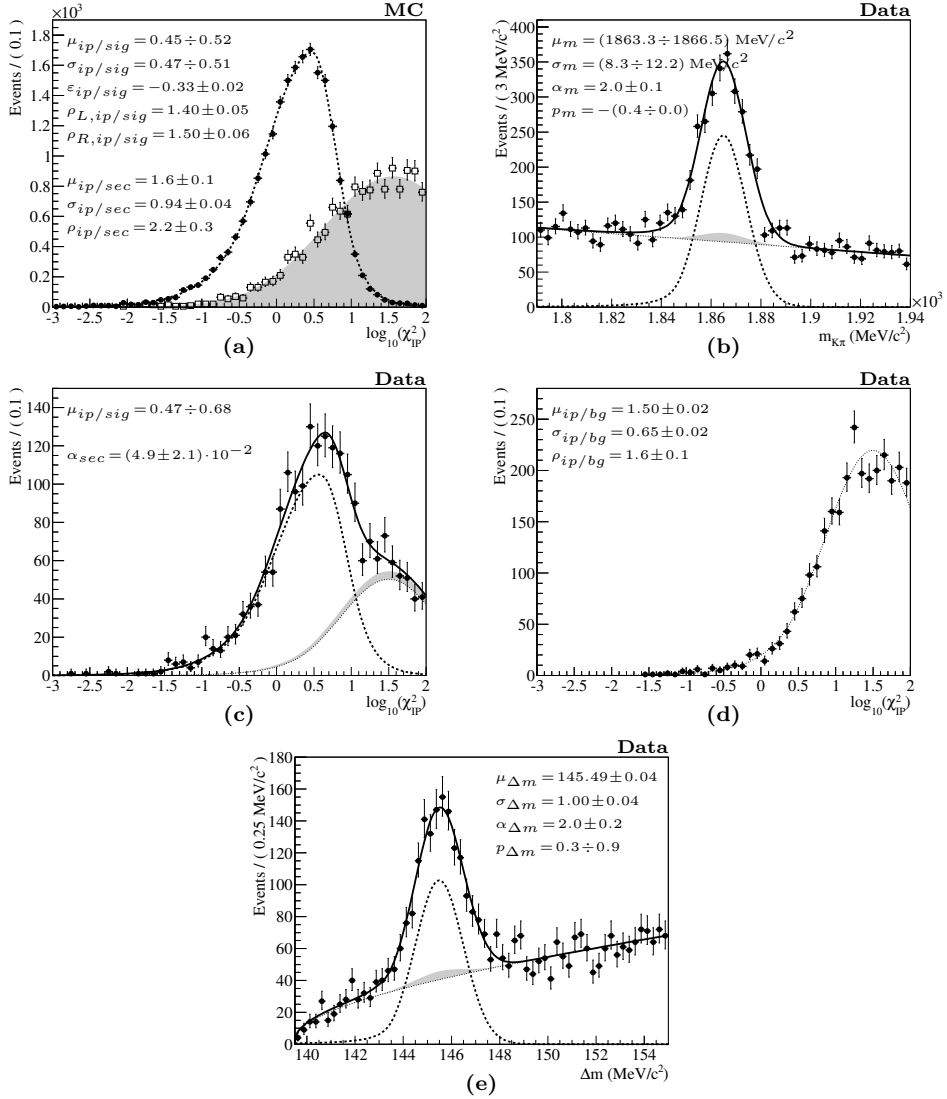


Figure B.12: Fit to the D^{*+} data for $0 < p_T < 4 \text{ GeV}/c$ and $3.5 < y < 4.5$.

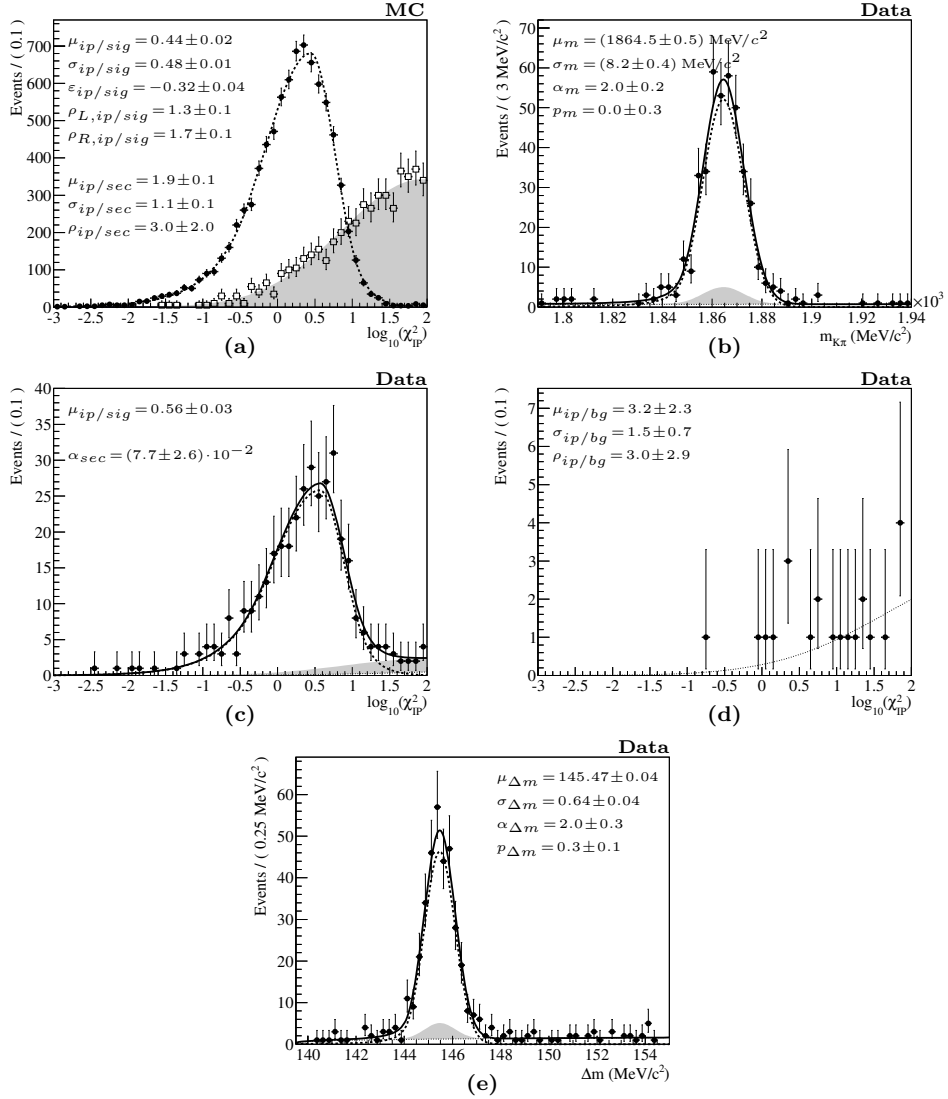


Figure B.13: Fit to the D^{*+} data for $4 < p_T < 8 \text{ GeV}/c$ and $2.0 < y < 3.0$.

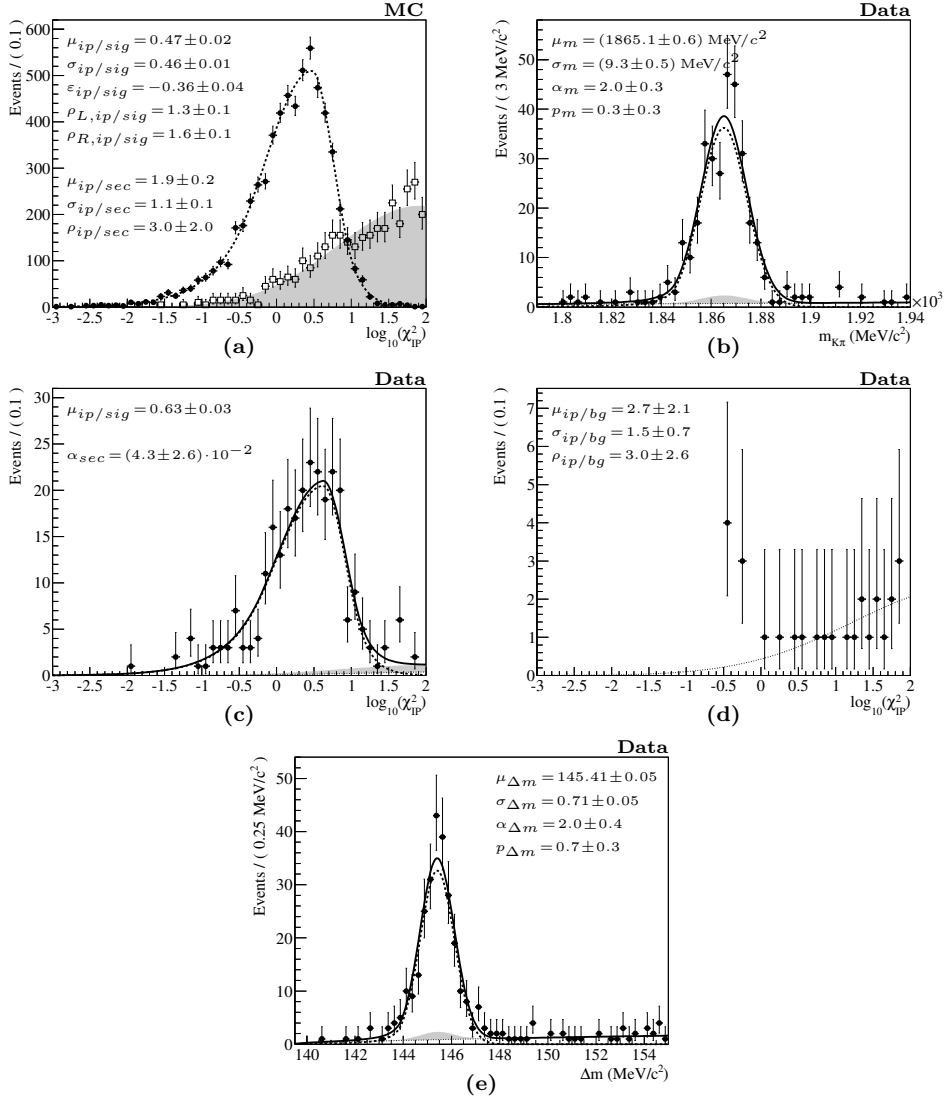


Figure B.14: Fit to the D^{*+} data for $4 < p_T < 8 \text{ GeV}/c$ and $3.0 < y < 3.5$.

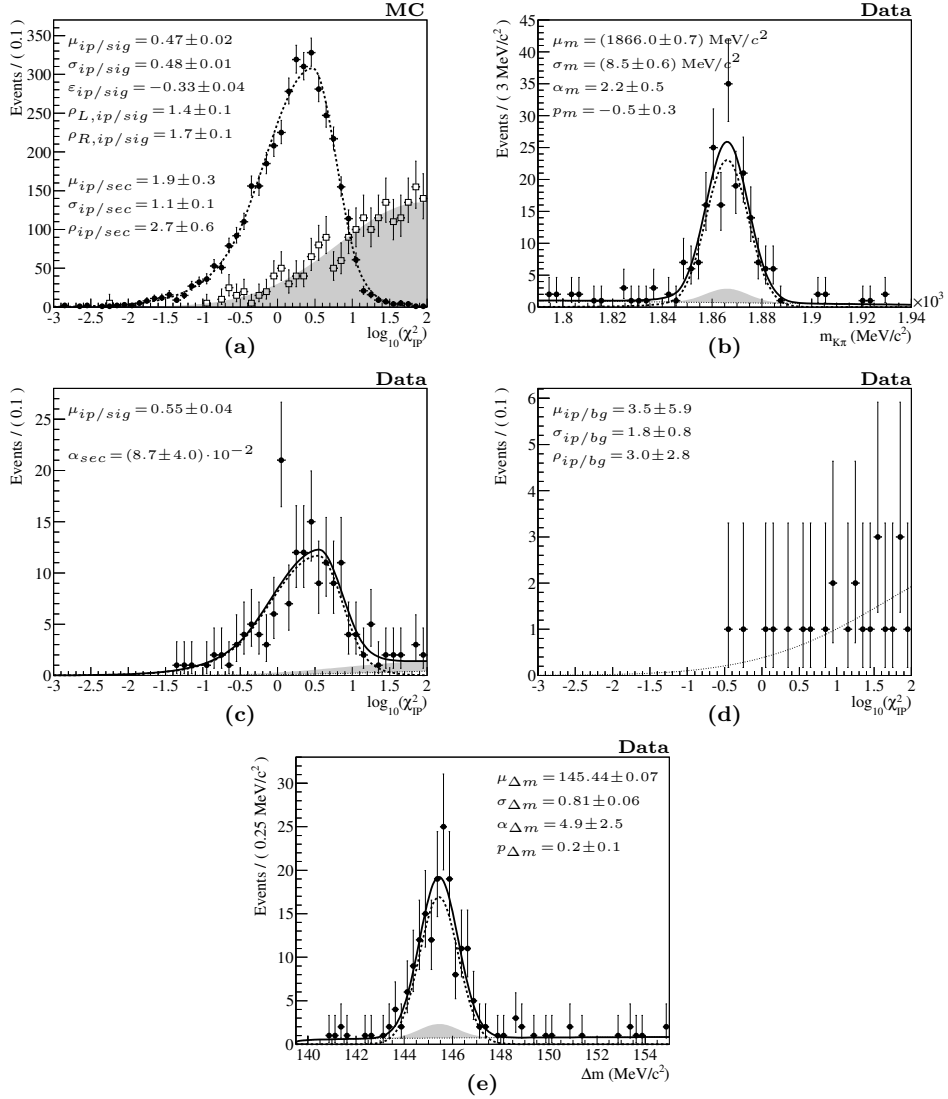


Figure B.15: Fit to the D^{*+} data for $4 < p_T < 8 \text{ GeV}/c$ and $3.5 < y < 4.5$.

Bibliography

- [1] M. Cacciari *et al.*, “Theoretical review of various approaches in heavy quark production”, *HERA and the LHC : A Workshop on the Implications of HERA for LHC Physics* (2005) 318.
- [2] M. Cacciari *et al.*, “Theoretical predictions for charm and bottom production at the LHC”, *JHEP* **1210** (2012) 137.
- [3] B. Kniehl *et al.*, “Inclusive Charmed-Meson Production at the CERN LHC”, *Eur.Phys.J.* **C72** (2012) 2082.
- [4] S. Glashow, J. Iliopoulos, and L. Maiani, “Weak Interactions with Lepton-Hadron Symmetry”, *Phys.Rev.* **D2** (1970) 1285–1292.
- [5] M. Kobayashi and T. Maskawa, “CP Violation in the Renormalizable Theory of Weak Interaction”, *Prog.Theor.Phys.* **49** (1973) 652–657.
- [6] SLAC-SP-017 Collaboration, J. Augustin *et al.*, “Discovery of a Narrow Resonance in e^+e^- Annihilation”, *Phys.Rev.Lett.* **33** (1974) 1406–1408.
- [7] E598 Collaboration, J. Aubert *et al.*, “Experimental Observation of a Heavy Particle J”, *Phys.Rev.Lett.* **33** (1974) 1404–1406.
- [8] C. Dominguez and M. Greco, “Charm, EVDM and Narrow Resonances in e^+e^- Annihilation”, *Lett.Nuovo Cim.* **12** (1975) 439.
- [9] J. C. Collins, D. E. Soper, and G. F. Sterman, “Factorization of Hard Processes in QCD”, *Adv.Ser.Direct.High Energy Phys.* **5** (1988) 1–91.
- [10] V. Gribov and L. Lipatov, “Deep inelastic ep scattering in perturbation theory”, *Sov.J.Nucl.Phys.* **15** (1972) 438–450.
- [11] G. Altarelli and G. Parisi, “Asymptotic Freedom in Parton Language”, *Nucl.Phys.* **B126** (1977) 298.
- [12] J. Pumplin *et al.*, “New generation of parton distributions with uncertainties from global QCD analysis”, *JHEP* **0207** (2002) 012.
- [13] R. Thorne, A. Martin, W. Stirling, and G. Watt, “Status of MRST/MSTW PDF sets”, [arXiv:0907.2387](https://arxiv.org/abs/0907.2387) [hep-ph].

- [14] G. 't Hooft and M. Veltman, “Regularization and Renormalization of Gauge Fields”, *Nucl.Phys.* **B44** (1972) 189–213.
- [15] B. Kniehl *et al.*, “Inclusive $D^{*\pm}$ production in p anti- p collisions with massive charm quarks”, *Phys.Rev.* **D71** (2005) 014018.
- [16] B. Kniehl *et al.*, “Collinear subtractions in hadroproduction of heavy quarks”, *Eur.Phys.J.* **C41** (2005) 199–212.
- [17] M. Cacciari, M. Greco, and P. Nason, “The p_T spectrum in heavy flavor hadroproduction”, *JHEP* **9805** (1998) 007.
- [18] M. Cacciari, S. Frixione, and P. Nason, “The p_T spectrum in heavy flavor photoproduction”, *JHEP* **0103** (2001) 006.
- [19] HFAG Collaboration, Y. Amhis *et al.*, “Averages of b -hadron, c -hadron, and τ -lepton properties as of early 2012”, [arXiv:1207.1158 \[hep-ex\]](#).
- [20] LHCb Collaboration, R. Aaij *et al.*, “Measurement of the B^\pm production cross-section in pp collisions at $\sqrt{s} = 7$ TeV”, *JHEP* **1204** (2012) 093.
- [21] LHCb Collaboration, R. Aaij *et al.*, “Prompt charm production in pp collisions at $\sqrt{s} = 7$ TeV”, *Nucl.Phys.* **B** (2013) .
- [22] LHCb Collaboration, R. Aaij *et al.*, “Measurement of mixing and CP violation parameters in two-body charm decays”, *JHEP* **1204** (2012) 129.
- [23] LHCb Collaboration, R. Aaij *et al.*, “Evidence for CP violation in time-integrated $D^0 \rightarrow h^- h^+$ decay rates”, *Phys.Rev.Lett.* **108** (2012) 111602.
- [24] CDF Collaboration, T. Aaltonen *et al.*, “Measurement of CP-violating asymmetries in $D^0 \rightarrow \pi^+ \pi^-$ and $D^0 \rightarrow K^+ K^-$ decays at CDF”, *Phys.Rev.* **D85** (2012) 012009.
- [25] LHCb Collaboration, R. Aaij *et al.*, “Observation of double charm production involving open charm in pp collisions at $\sqrt{s}=7$ TeV”, *JHEP* **1206** (2012) 141.
- [26] L. Evans and P. Bryant, “LHC Machine”, *JINST* **3** (2008) S08001.
- [27] ATLAS Collaboration, G. Aad *et al.*, “The ATLAS Experiment at the CERN Large Hadron Collider”, *JINST* **3** (2008) S08003.
- [28] CMS Collaboration, S. Chatrchyan *et al.*, “The CMS experiment at the CERN LHC”, *JINST* **3** (2008) S08004.
- [29] LHCb Collaboration, J. Alves, A. Augusto *et al.*, “The LHCb Detector at the LHC”, *JINST* **3** (2008) S08005.
- [30] ALICE Collaboration, K. Aamodt *et al.*, “The ALICE experiment at the CERN LHC”, *JINST* **3** (2008) S08002.

- [31] CMS Collaboration, S. Chatrchyan *et al.*, “Measurement of the inelastic proton-proton cross section at $\sqrt{s} = 7$ TeV”, [arXiv:1210.6718 \[hep-ex\]](#).
- [32] TOTEM Collaboration, G. Antchev *et al.*, “Luminosity-independent measurements of total, elastic and inelastic cross-sections at $\sqrt{s} = 7$ TeV”, CERN-PH-EP-2012-353.
- [33] LHCb Collaboration, S. Amato *et al.*, “LHCb VELO: Technical Design Report”, CERN-LHCC-2001-011.
- [34] LHCb Collaboration, A. Vollhardt, “The LHCb Silicon Tracker”, CERN-LHCB-2003-143.
- [35] LHCb Collaboration, A. Franca *et al.*, “LHCb Inner Tracker: Technical Design Report”, CERN-LHCC-2002-029.
- [36] LHCb Collaboration, S. Amato *et al.*, “LHCb Outer Tracker: Technical Design Report”, CERN-LHCC-2001-024.
- [37] LHCb Collaboration, S. Amato *et al.*, “LHCb RICH: Technical Design Report”, CERN-LHCC-2000-037.
- [38] LHCb Collaboration, S. Amato *et al.*, “LHCb calorimeters: Technical Design Report”, CERN-LHCC-2000-036.
- [39] LHCb Collaboration, S. Amato *et al.*, “LHCb muon system: Technical Design Report”, CERN-LHCC-2001-010.
- [40] LHCb Collaboration, R. Aaij *et al.*, “The LHCb Trigger and its Performance”, [arXiv:1211.3055 \[hep-ex\]](#).
- [41] LHCb Collaboration, M. Clemencic *et al.*, “The LHCb simulation application, Gauss: Design, evolution and experience”, *J.Phys.Conf.Ser.* **331** (2011) 032023.
- [42] GEANT4 Collaboration, S. Agostinelli *et al.*, “GEANT4: A Simulation toolkit”, *Nucl.Instrum.Meth.* **A506** (2003) 250–303.
- [43] J. Allison *et al.*, “Geant4 developments and applications”, *IEEE Trans.Nucl.Sci.* **53** (2006) 270.
- [44] J. Amoraal, “Alignment with Kalman filter fitted tracks and reconstruction of $B_s^0 \rightarrow J/\psi\phi$ decays”, PhD thesis, Vrije Universiteit Amsterdam, 2011.
- [45] W. Blum, L. Rolandi, and W. Riegler, “Particle detection with drift chambers”, ISBN-13-9783540766834.
- [46] G. van Apeldoorn *et al.*, “Beam tests of final modules and electronics of the LHCb outer tracker in 2005”, CERN-LHCB-2005-076.
- [47] V. Gromov and T. Sluijk, “Electrical properties of various types of straw tubes considered for the LHCb outer tracker”, CERN-LHCB-2001-001.

- [48] V. Coco. Private communication.
- [49] RD12 Collaboration, B. Taylor, “TTC distribution for LHC detectors”, *IEEE Trans.Nucl.Sci.* **45** (1998) 821–828.
- [50] M. Schiller, “Standalone track reconstruction for the Outer Tracker of the LHCb experiment using a cellular automation”, PhD thesis, University of Heidelberg, 2007.
- [51] J. van Tilburg, “Track simulation and reconstruction in LHCb”, PhD thesis, Vrije Universiteit Amsterdam, 2005.
- [52] LHCb Collaboration, R. Aaij *et al.*, “Absolute luminosity measurements with the LHCb detector at the LHC”, *JINST* **7** (2012) P01010.
- [53] LHCb Collaboration, I. Belyaev *et al.*, “Handling of the generation of primary events in Gauss, the LHCb simulation framework”, *J.Phys.Conf.Ser.* **331** (2011) 032047.
- [54] M. Needham, “Clone track identification using the Kullback-Leibler distance”, CERN-LHCB-2008-002.
- [55] W. Verkerke and D. P. Kirkby, “The RooFit toolkit for data modeling”, [arXiv:0306116 \[physics\]](#).
- [56] M. Oreglia, “A Study Of The Reactions $\psi' \rightarrow \gamma\gamma\psi$ ”, SLAC-0236, UMI-81-08973, SLAC-R-0236, SLAC-R-236.
- [57] LHCb Collaboration, A. Powell, “Particle identification at LHCb”, *PoS ICHEP2010* (2010) 020.
- [58] LHCb Collaboration, A. Powell, “Reconstruction and PID performance of the LHCb RICH detectors”, *Nucl.Instrum.Meth.* **A639** (2011) 260–263.
- [59] BABAR Collaboration, J. Lees *et al.*, “Branching Fraction Measurements of the Color-Suppressed Decays $\bar{B}^0 \rightarrow D^{(*)0}\pi^0$, $D^{(*)0}\eta$, $D^{(*)0}\omega$, and $D^{(*)0}\eta'$ and Measurement of the Polarization in the Decay $\bar{B}^0 \rightarrow D^{*0}\omega$ ”, *Phys.Rev.* **D84** (2011) 112007.
- [60] E. Lohrmann, “A Summary of Charm Hadron Production Fractions”, [arXiv:1112.3757 \[hep-ex\]](#).
- [61] B. Kniehl, G. Kramer, I. Schienbein, and H. Spiesberger. Private communication.
- [62] M. Cacciari, S. Frixione, M. Mangano, M. Nason, and G. Ridolfi. Private communication.
- [63] LHCb Collaboration, N. Tuning, “ b production cross section and fragmentation fractions f_s/f_d at LHCb”, *PoS BEAUTY2011* (2011) 050.

Summary

The LHC is a hadron collider located in a circular tunnel 27 km in circumference, designed to collide two beams of protons with 7 TeV nominal energy in each beam. The LHCb experiment is one of the four experiments located at interaction points. LHCb detector is a single-arm forward spectrometer dedicated to flavor physics studies. Its main goals are precision measurements of CP-violation and meson mixing, as well as studies of rare decays of heavy flavor particles, to search for physics beyond the Standard Model ('New Physics') using the decays of b - and c -hadrons.

The Outer Tracker (OT), one of the LHCb sub-detectors, is a straw drift-tube detector used for tracking of charged particles and their momentum measurement. It consists of three stations and covers the region surrounding a smaller silicon Inner Tracker. Each station consists of four layers of modules which in turn contain two mono-layers of straw tubes. The straw tubes are 5 mm in diameter and measure the drift time via the ionization clusters induced by charged particles.

About 70% of all reconstructed tracks in LHCb pass through the active area of the OT, and for these tracks about half of the hits are provided by the OT, the remaining hits originate from the upstream tracking detectors. These OT hits contribute mainly to the momentum estimate of the particle and the trajectory slope determination in the RICH detectors. The calibration of the OT, which includes timing and spatial alignment, allows to improve the single hit resolution, consequently improving the precision of the track-parameter estimates.

The first part of this thesis describes the timing calibration of the OT and includes t_0 and TR-relation, as well as signal propagation and resolution calibration. The developed calibration procedures are currently used for the OT timing calibration in the LHCb experiment. The calibration allows to achieve average time resolution of approximately 3 ns, which is equal to result obtained in the 2005 beam test. The corresponding average spatial resolution is 210 μm . In this thesis it is shown that the resolution can be improved to approximately 2.4 ns with the implementation of half mono-layer alignment which then corresponds to the average spatial resolution of 180 μm .

Quantum chromodynamics (QCD) is the theory of the strong interactions, which describes the interactions of quarks and gluons. In QCD, the six quark flavors are divided in light and heavy quarks, depending on their relation to the QCD scale. The knowledge of heavy quark production in proton-proton collisions is important for understanding and testing of QCD. In addition, the precise knowl-

edge of the heavy quark production cross section is important as charm and beauty from QCD processes contribute to the background for other, often rare, SM processes, e.g. in Higgs production.

The second part of this thesis presents the measurement of the open charm production cross section of D^0 and D^{*+} . The measurement is performed using 15 nb^{-1} of proton-proton collision data collected under low pile-up conditions with the LHCb detector at 7 TeV center-of-mass energy in May 2010. The cross sections are measured in bins of transverse momentum p_T and rapidity y : 8 bins of width 1 GeV/ c in the range $0 < p_T < 8 \text{ GeV}/c$, and 5 bins of width 0.5 units in the range $2.0 < y < 4.5$. The total $c\bar{c}$ cross section in the experimental kinematic region is determined to be $\sigma(c\bar{c}, D^0) = (1470 \pm 121) \mu\text{b}$ and $\sigma(c\bar{c}, D^{*+}) = (1512 \pm 224) \mu\text{b}$ using D^0 and D^{*+} cross sections, respectively. The measured cross sections are compared with theoretical predictions (Fixed Order Next-to-Leading Log and General Mass Variable Flavor Number Scheme) and found to be compatible within theoretical uncertainties.

There has been a major development in the experimental knowledge of the charm sector in the past few years. This includes the measurement of open and closed charm production, double charm production, the $c - \bar{c}$ production asymmetry, $D^0 - \bar{D}^0$ mixing and measurement of CP violation (CPV). The large production cross section, in combination with the high efficiency of LHCb detector will lead to interesting charm physics results in the future.

Samenvatting

De LHC is een hadron versneller gesitueerd in een circulaire tunnel met een omtrek van 27 km, die ontworpen is om twee bundels protonen met een energie van 7 TeV per bundel te laten botsen. Het LHCb experiment is één van de vier experimenten in de interactiepunten. De LHCb detector is een eenarmige voorwaarts gebouwde spectrometer gemaakt om *flavor* fysica te bestuderen. De hoofddoelen van het experiment zijn om precisiemetingen uit te voeren van CP-schending en meson mixing, maar ook om zeldzame vervallen te bestuderen van zware quarks, om zodanig te zoeken naar fysica buiten het standaard model ('nieuwe fysica') gebruikmakend van de vervallen van *b*- en *c*-hadronen.

De Outer Tracker (OT), een van de subdetectoren van LHCb, is een detector bestaande uit gasgevulde cilindrische cathode driftbuizen ('rietjes'). Deze wordt gebruikt om de sporen van geladen deeltjes en hun impuls te meten. Hij bestaat uit drie stations en omringt de veel kleinere Inner Tracker. Elk station bestaat uit vier lagen van modules, welke elk twee monolagen rietjes bevatten. De rietjes zijn 5 mm in diameter en meten de drifttijd via de ionisatieclusters die door geladen deeltjes gemaakt worden.

Ongeveer 70% van alle gereconstrueerde sporen in LHCb gaan door het actieve oppervlak van de OT en voor deze sporen wordt ongeveer de helft van de 'hits' door de OT gegeven, de overige hits komen van de detectoren stroomopwaarts. Deze OT hits dragen voornamelijk bij aan de geschatte waarde van de impuls van het deeltje en de geschatte waarde van de baanrichting in de RICH detectoren. De calibratie van de OT bevat tijd- en ruimte-informatie en zorgt voor een verbetering van de resolutie van een hit met als gevolg een verbetering van de precisie van de gemeten spoorparameters.

Het eerste deel van dit proefschrift beschrijft de tijdsalibratie van de OT en bevat de bepaling van t_0 en TR-relatie, alsook signaalpropagatie en calibratie van de resolutie. De ontwikkelde procedures worden gebruikt in de huidige calibratie van de OT tijden in het LHCb experiment. De calibratie maakt het mogelijk een waarde voor de tijdsresolutie te verkrijgen van ongeveer 3 ns, gelijk aan het resultaat verkregen in de testbundel van 2005. De corresponderende gemiddelde ruimtelijke resolutie is 210 μm . In dit proefschrift wordt aangetoond dat de resolutie kan worden verbeterd tot ongeveer 2.4 ns door de implementatie van alineëring van halve monolagen, welke dan correspondeert met een gemiddelde ruimtelijke resolutie van 180 μm .

Quantumchromodynamica (QCD) is de theorie van de sterke interacties die de

wisselwerkingen beschrijft tussen quarks en gluonen. In QCD zijn de zes quarks-maken verdeeld in lichte en zware quarks, afhankelijk van hun relatie tot de QCD schaal. De kennis van productie van zware quarks in proton-proton botsingen is belangrijk voor het begrip en het testen van QCD. Ook is de precieze kennis van de productie doorsnede van zware quarks belangrijk omdat 'charm' en 'beauty' productie uit QCD processen bijdragen aan de achtergrond van andere, vaak zeldzame, SM processen, zoals b.v. Higgsproductie.

Het tweede deel van dit proefschrift presenteert de meting van de productie doorsnede voor 'open charm' in D^0 en D^{*+} . De meting is uitgevoerd met 15 nb^{-1} aan proton-proton botsingsdata, verzameld in lage 'pile-up' condities met de LHCb detector bij 7 TeV botsingsenergie in Mei 2010. De werkzame doorsnedes worden gemeten in 'bins' van transversale impuls p_T en rapiditeit, y : 8 bins met breedte $1 \text{ GeV}/c$ in het bereik $0 < p_T < 8 \text{ GeV}/c$, en 5 bins met een breedte van 0.5 eenheden in het bereik $2.0 < y < 4.5$. De totale $c\bar{c}$ doorsnede in de experimentele kinematische gebied is gemeten als $\sigma(c\bar{c}, D^0) = (1470 \pm 121) \mu\text{b}$ en $\sigma(c\bar{c}, D^{*+}) = (1512 \pm 224) \mu\text{b}$ voor respectievelijk de D^0 en D^{*+} doorsnedes. De gemeten werkzame doorsnedes worden vergeleken met theoretische voorspellingen (*Fixed Order Next-to-Leading Log* en *General Mass Variable Flavor Number Scheme*) en blijken compatibel binnen de theoretische onzekerheden.

Er is de laatste jaren een grote ontwikkeling in de experimentele kennis van de charm sector. Deze kennis omvat ook de meting van open en gesloten productie van 'charm', dubbele 'charm'-productie, de $c - \bar{c}$ productie asymmetrie, $D^0 - \bar{D}^0$ mixing en de meting van CP schending. De grote productie doorsnede, samen met de hoge efficiëntie van de LHCb detector zal leiden tot interessante 'charm'-fysica resultaten in de toekomst.

Acknowledgments

Dear friends and colleagues. It has been a great pleasure to work at Nikhef. I would like to thank everyone for their help in work, life and, of course, in writing and preparing this manuscript. I especially would like to thank Marcel and Thomas for their expertise and patience.

I am really thankful to my family for all their support during this long path, starting from university and then working at Nikhef.

Dear colleagues, Wouter, Jan, Fabian, Serena, Chiara, Jeroen, Roel, Ivan, Edward, Gabriel, thank you for all your advise, fruitful discussions and also parties. Special thanks to Niels and Antonio, the experts from whom I learned a lot about the OT. It was real pleasure to get to know you all.

I would especially like to thank Vanya who always helped me with the LHCb analysis software and other things. He constantly pushed me with my thesis research, so special thanks to him for this.

A bit of a story related to the cover of this thesis. My original idea was to include a winter forest as it represented in my mind the straws of OT, as well as the beauty and charm of Russian nature. Well, some of you actually saw right away that it resembles OT. There are many other things one can see in it: alignment - relative position of trees, noise and aging - branches, background - snow, etc. I hope you like it.

This was a great time, thank you all,
Alexandr (aka Alex)

